

Layer parallel shortening and cataclastic flow by fractures in the Permian Kapp Starostin Formation, Mediumfjellet, Spitsbergen

Siri Anne Haugland Strand



Master of Science Thesis

**Department of Earth Science, University of Bergen
Department of Arctic Geology, University Centre in Svalbard**

June 2015

ABSTRACT

This study presents a structural analysis, from macro- to micro-scale, of the Permian carbonates and spiculites of the Kapp Starostin Formation. The analysis was conducted to better understand the fracture development and deformation in a Fold and Thrust Belt environment, located to the Mediumfjellet that is displaying a major thrust-stack in the thin-skinned part of the Paleogene West-Spitsbergen Fold and Thrust Belt.

Methods include regional mapping and cross-section construction, coupled with Lidarscan interpretations in the software Lime. These data forms a base for calculations of layer parallel shortening. Field methods include lithostratigraphically logging with additional thin section studies. Further, scanlines record fracture frequency (fractures per meter) both along strike and dip with respect to bedding, and reveal fracture orientations, terminations and fill.

The Kapp Starostin Formation comprises mainly spiculitic units with some silicified carbonate and shale beds. Permian strata are deformed along four well-known major thrusts (M1-M3, and G), but the observation of a new, major structure in the hangingwall of the M2, suggests the presence of another thrust in the area, termed the M2 upper splay.

The bryozoan limestone has higher fracture frequency than dolomite, brachiopod limestone, spiculite and shale, and may have more fractures in thinner beds, in contrast to the other lithologies. The fracture data shows five main fracture populations striking; (i) nearly E-W, (ii) NNW-SSE, (iii) NW-SE, (iv) NE-SW to NNE-SSW and (v) nearly N-S.

The findings of this study indicate a total layer parallel shortening averaging a minimum of 64 percent/m, with highest shortening in the hinge zone of the folds. The characteristics of the fracture network suggest folding by cataclastic flow, in most layers characterized by frictional flow on fractures rather than flexural slip along layers. The fractured tight Permian rocks in Mediumfjellet makes the studied strata an analogue for fractured reservoirs in fold-thrust belts.

Keywords: Fold and Thrust Belt, Kapp Starostin Formation, spiculites, fracture systems, cataclastic flow

ACKNOWLEDGEMENTS

First of all, I would like to thank my supervisor Alvar Braathen (University of Oslo), who has supported me from day one. Thank you for giving me the opportunity to write a master thesis with fieldwork and additional courses at Svalbard. Thank you for all the feedback on the thesis, and the time you have used on discussions and explanations.

I would also like to thank my supervisor Atle Rotevatn at the University of Bergen for major support, especially during my last semester.

I will express my gratitude to my supervisor at UNIS, Snorre Olausen, who have helped me with the sedimentological part of the studies. Lars Stemmerik and Gunnar Sælen for feedback and discussion on my thin section studies. Leif Bjørnar Henriksen for guidance and discussion about the Kapp Starostin Formation. Simon Buckley for great help with the Lidarscan part of my studies. Irina Maria Dumitru for making my thin sections and learning me about thin section studies, and of course Jeremy Watt for final improvements on my text.

Thanks to Svalbard Science Forum (SSF) for founding my master project, Lina Asbjørnsens Stipendiefond for their generous scholarship, and UNIS for helping me with logistics during fieldwork. Further I want to thank Thea Malene Ohnstad Broch, Olav Aleksander Naurstad and Marita Thomassen for outstanding assistance during fieldwork at Mediumfjellet.

Especially thanks to my family for support and motivation, it meant everything.

Finally, I want to thank my fellow students at the University of Bergen, particularly the girls at “Midtrommet”, for five great years, and everybody else helping me through the time writing the master thesis.

Bergen, 28th of May 2015

Siri Anne Haugland Strand

Table of Contents

CHAPTER 1 INTRODUCTION.....	1
1.1 Preface.....	1
1.2 Aims and objectives.....	1
1.3 Geographic location and local topography.....	2
1.4 Geological framework.....	4
1.5 Methods.....	6
1.5.1 Fracture sampling.....	6
1.5.2 Fracture analysis.....	6
1.5.3 Statistical analysis.....	7
1.5.4 Lithology.....	7
1.5.5 Lidarscan.....	8
1.5.6 Thin sections.....	9
CHAPTER 2 GEOLOGICAL SETTING.....	11
2.1 Regional setting – geological history of Spitsbergen.....	11
2.2 Previous work.....	14
2.3 Spitsbergen’s main geological periods.....	15
2.3.1 Basement.....	15
2.3.2 Old Red (Devonian).....	15
2.3.3 Late Paleozoic.....	16
2.3.4 Mesozoic.....	18
2.3.5 Cenozoic.....	19
2.4 The Tertiary Fold and Thrust Belt.....	20
2.4.1 Deformation provinces.....	21
2.4.2 Kinematics.....	24
2.4.3 Sedimentary basins.....	24
2.5 Mediumfjellet – location of field studies.....	26
CHAPTER 3 CONCEPTS OF FRACTURE SYSTEMS IN FOLD THRUST BELTS.....	29
3.1 Introduction.....	29
3.2 Fold and thrust geometries.....	29
3.2.1 Thrust systems.....	29
3.2.2 Thrust geometry.....	30
3.2.3 Thrust related folds.....	32
3.3 Fracture development.....	35
3.3.1 Basic fracture types.....	35
3.3.2 Diagenetic fractures.....	36
3.3.3 Tectonic fractures.....	37
3.3.4 Fracture intensity.....	38
3.4 Fold related fractures.....	39
3.4.1 Cataclastic flow related to folding.....	41
3.5 Fluid flow on fractures.....	42
CHAPTER 4 LITHOLOGY DESCRIPTION.....	45
4.1 Introduction.....	45
4.2 Gipsdalen Group.....	46

4.2.1	Gipshuken Formation.....	48
4.3	Tempelfjorden Group.....	49
4.3.1	Kapp Starostin Formation.....	49
4.4	Intrusions.....	52
4.5	The stratigraphic importance of deformation.....	54
4.6	Summary and interpretation.....	54
CHAPTER 5 RESULTS AND STRUCTURAL DESCRIPTIONS.....		57
5.1	Introduction.....	57
5.2	Structural framework of the area.....	57
5.2.1	M1 fold and thrust province.....	58
5.2.2	M2 fold and thrust province.....	59
5.2.3	M3 fold and thrust province.....	59
5.2.4	Gavltinden fold and thrust province.....	60
5.3	Lidarscan interpretations and layer parallel shortening (LPS).....	62
5.3.1	Meso-scale shortening.....	62
5.3.2	Macro-scale shortening.....	67
5.3.3	Estimated total shortening in Mediumfjellet (Y).....	69
5.4	Fracture characterization.....	71
5.4.1	Bed-confined fractures (BC).....	71
5.4.2	Through-going fractures (TG).....	72
5.4.3	Calcite precipitation (CP).....	72
5.4.4	Slip lineations on fracture plain.....	73
5.5	Fracture orientation trends.....	75
5.6	Fracture frequency variations.....	80
5.6.1	Comparing fracture frequency for all scanlines.....	80
5.6.2	Comparing fracture frequency for bed-confined fractures.....	81
5.6.3	Comparing fracture frequency for through-going fractures.....	82
5.6.4	Comparing fracture frequency for lithologies.....	83
5.6.5	Fracture frequency compared with bed thickness.....	85
5.7	Microtextural analysis.....	87
5.7.1	Observations.....	88
5.7.2	Conclusions from thin section studies.....	94
CHAPTER 6 STRUCTURAL ANALYSIS AND DISCUSSION.....		97
6.1	Introduction.....	97
6.2	Summary of fracture distribution and characteristics.....	97
6.3	Large-scale structures and their lateral variability.....	99
6.4	Fractures related to the fold-thrust belt.....	100
6.5	Fracture systems in lithostratigraphic framework.....	103
6.6	Strain by cataclastic flow.....	107
6.6.1	Mesoscopic deformation.....	107
6.6.2	Sub-mesoscopic deformation (microscopic deformation).....	108
6.7	Possible fluid flow and similar fracture reservoirs.....	109

CHAPTER 7 CONCLUSION AND FUTURE WORK.....	113
7.1 Conclusions.....	113
7.2 Future work.....	114
CHAPTER 8 REFERENCES.....	117
APPENDIX.....	129

CHAPTER 1 INTRODUCTION

This master thesis has been part of a collaborative project in which the University of Bergen and University Centre in Svalbard have contributed. The Svalbard Science Forum (SSF) sponsored the last field trip during the summer of 2014.

1.1 Preface

This study is motivated by the fact that close to half of the major oil and gas fields as well as major groundwater aquifers of the world are located in fold-thrust belts, many with fractured reservoirs (Nelson 2001, Goffey et al. 2010, Roeder 2010, Margat and Van der Gun 2013). A fractured reservoir is at all scales heterogeneous, from micro to macro-scale. By studying outcrops, the understanding of fracture distribution can be improved to better predict fluid flow (Wennberg et al. 2006). This thesis describes fracture rocks as a reservoir analogue, covering Permian carbonates and spiculites, in a fold-thrust belt setting, with Spitsbergen as the chosen location.

The thesis is divided into 7 chapters. Chapter 1 introduces the study area, a summary of the geological history at Svalbard and methods used in this thesis. A more detailed geological background can be found in Chapter 2, describing both the depositional and tectonic history of the studied rocks, with an emphasis on the Tertiary Fold and Thrust Belt. Chapter 3 focuses on the relevant theory giving a background for the results and discussion. The stratigraphy of the Mediumfjellet is described in Chapter 4, based on field observations, whereas Chapter 5 focuses on the structural part of the area. The discussion in Chapter 6 will address the fracturing in the fold-thrust belt, and compare field observations with earlier work. The conclusion of this thesis is presented in Chapter 7.

1.2 Aims and objectives

The aim of this master thesis is to study fracture systems in the Permian Kapp Starostin Formation. The studied succession is located in the central parts of the Tertiary Fold and Thrust Belt of Spitsbergen, at the southern tip of Mediumfjellet, north of Isfjorden. These data can be used to consider if fractures in a section of layered rocks offers a potential flow-path in an otherwise tight reservoir, either for

water or hydrocarbons. Parts of the project have also addressed the importance of layer-parallel-shortening (LPS) and how LPS is connected to fracturing and folding mechanisms in the fold-thrust belt.

Key questions addressed in this thesis are links to fractures of tight reservoirs in fold-thrust belts

- How is the pattern and evolution of the investigated fractures, and how do they link to lithologies with general characteristics?
- How do small-scale deformation relate to the fold-thrust belt?
- Can the fractures be connected to layer parallel shortening and dilation during cataclastic flow?
- Are the mapped fractures important for fluid flow, and how can these data be used as an analogue for fractured reservoirs in fold-thrust belts?

1.3 Geographic location and local topography

Svalbard is positioned in the Norwegian High Arctic (around 78 °33'N, 14°6'E) approximately midway between Norway and the North Pole (Figure 1.1). Svalbard is an archipelago, with the main islands consisting of Spitsbergen, Nordaustlandet, Barentsøya, Edgeøya, Kong Karls Land, Prins Karls Forland, Kvitøya, Hopen and Bjørnøya. The main settlement is in Longyearbyen, located at the island Spitsbergen with approximately 2600 inhabitants (in 2012).

The study area of this thesis is located in Spitsbergen, on the northwest side of Isfjorden, in the region called Oscar II Land (UTM: 33x 482894 8712932). In this region the landscape is characterized by steep slopes and high peaks, where the highest peaks reach more than 800 m a.s.l. This location in the High Arctic conforms to a cold and dry environment, classified as an arctic desert. However, precipitation varies significantly, from the wetter western coast to the drier inland. The location of the study area attests to some impact of the coastal climate.

The field data was collected at the southern front of the mountain range called Mediumfjellet. The study site is partly covered by the Wahlenberg glacier to the west, and terminates against the steep mountainside of Mediumfjellet to the north and the sea in the south and SE. The location is reached by boat and is approximately 50 km

from Longyearbyen. The site has been selected due to outstanding exposures, with 95% of the area exposed, and rocks that have been polished by the overriding glacier. The large outcrop is relatively easy accessible from the beach in the SE, but the climb up to the ridge itself is rather steep and at places vertical, constraining access to parts of the outcrop.

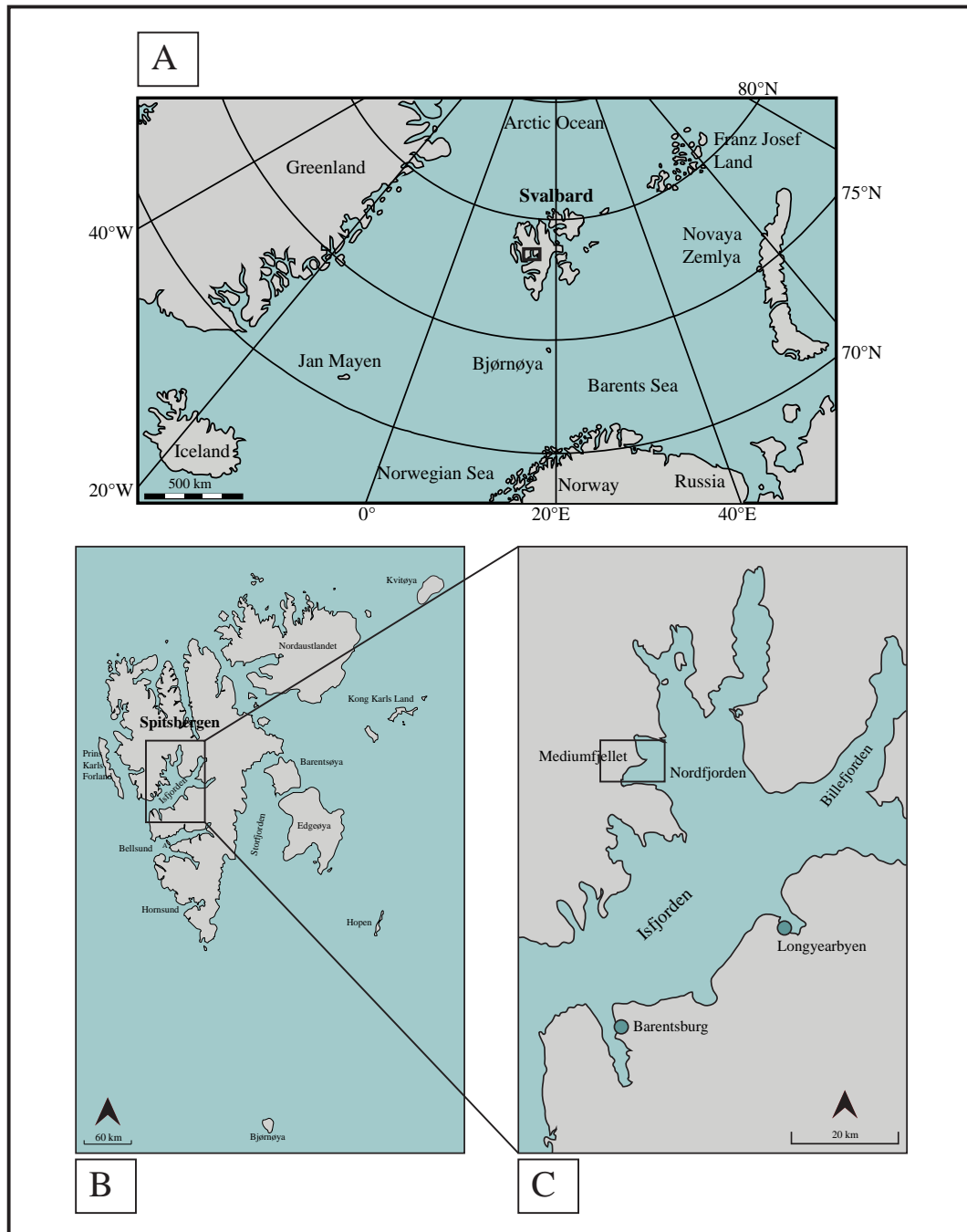


Figure 1. 1: Geographic map and location of Svalbard and field area. **A)** Map showing Svalbard's geographical location. **B)** Map of Svalbard, with a box locating the field area. **C)** Zoom-in on the location of Mediumfjellet and surrounding areas. Note the blue dots for the location of Longyearbyen and Barentsburg. Modified after maps from Norwegian Polar Institute.

1.4 Geological framework

The geological history of the Svalbard archipelago is long and diverse. There are rocks present covering all epochs from the Precambrian to the Tertiary, with the present landscape developing in front of our eyes. The geological archive shows that the archipelago has been drifting from close to the South Pole northward to its present position (Dallmann et al. 1999) the last 600 Ma. In this evolution, the Caledonian Orogeny strongly impacted the so-called Hekla Hoek basement, reworking older gneissic units and deforming younger sediments that in general became metamorphosed to greenschist facies (partly higher P-T). Among the different lithologies post-dating the Caledonian orogeny that attest to a changing climate are the Devonian old red sandstones, Carboniferous coals and Permian carbonates and spiculites (Dallmann et al. 1999, Elvevold et al. 2007).

The sedimentological record gives a good indication on the environment, while the many faults and folded layers tells a story of major tectonic events. The “Old Red” succession (Devonian) is up to 9000 m thick and located to a large fault-bound basin well exposed in the deeper exhumed north of Spitsbergen. This basin has a complex tectonic evolution, with various contributions advocating strike-slip and reverse faulting events as key tectonic signals (Friend et al. 2000, Blomeier et al. 2003, Bergh et al. 2011, Bælum and Braathen 2012). The paper by Braathen et al. (2011) refers to the location and implications of a major extensional detachment, promoting the significant tectonic similarities with the late-post Caledonian extension seen for mainland Norway. As the metamorphic basement and the Devonian basin occur in the deeper exhumed region north of the study area, these rocks are of less relevance for this thesis.

After the Devonian, a peneplain was developed and subsequently covered by Early Carboniferous sandstones and coal before the onset of the first post-Caledonian rifting event, which is of mid-late Carboniferous age (Steel and Worsley 1984, Harland et al. 1997). From the Permian and throughout the Mesozoic Svalbard was overall a stable platform that experienced nearly continuous deposition of sediments, although minor faulting has been discussed for areas in the east (Anell et al. 2013), and abandoned rift events are well documented for the Barents Shelf in the south (e.g. Gabrielsen et al. 1990, Faleide et al. 2008), noticeably of Permo-Triassic and especially Late Jurassic-

Early Cretaceous age. For most of the shelf, the end of the Permian notes a marked shift in deposition, when a change from bioclastic to siliciclastic-dominated environments occurred. By the time of the Cretaceous, seafloor spreading developed farther south in the Atlantic Ocean. With gradually northward propagation of this ocean basin, dextral transform movements initiated between Greenland and the Barents Shelf, connecting spreading ridges of the Atlantic and Arctic basins. Movements on this transform fault caused shortening of the margins, as well manifested by Svalbard's Tertiary fold and thrust belt, herein abbreviated FT-Belt (Harland 1969, Faleide et al. 1993, Dallmann et al. 1999, Braathen et al. 2011) that is of Paleogene-Eocene age (Maher et al. 1995).

The Tertiary FT-Belt runs along the western part of Spitsbergen, with its foreland basin system covering large parts of the more central parts of the island. The rocks are highly tectonised along the western coast, with major basement-involved thrust sheets. Eastward, the tectonic style changes, as the FT-Belt is mainly thin-skinned. There, intensity of folding and thrust-displacement is less pronounced, albeit spectacular in regions that are deeper exhumed such as the Oscar II Land. When reaching the region of Central Spitsbergen where tectonism links to decollements, the succession is nearly flat-laying; however, there are some local splay thrusts and related folds (Braathen et al. 1999). Even farther east, the FT-Belt interacts with reactivated deep-seated lineaments, the Billefjorden and Lomfjorden fault zones, before the decollement style of deformation reoccurs for eastern Spitsbergen (Haremo et al. 1990, Bergh et al. 1997). Mediumfjellet, which is the location of the undertaken field studies, has been termed the thrust front (Bergh et al., 1997). There, a shift from a lower detachment in lower Permian evaporates (Gipshuken Fm.) to one in lower Triassic black shales (Bravaisberget Fm.) sets up a major imbricate stack (or duplex) that is well displayed in the Permo-Triassic succession. This conforms to the thin-skinned deformation, with thrust sheets stacked in a piggyback sequence that is disturbed by out-of-sequence thrusting. Four major thrust sheets have been identified; the Mediumfjellet sheets termed M1, M2, M3 and Gavltinden sheet named G (Bergh and Andresen, 1990), of which the latter is the mentioned out-of-sequence structure as it decapitates folds of the M3 (Bergh et al., 1997). A detailed description of Svalbard's geological history and especially Mediumfjellet's setting is given in Chapter 2 *Geological setting*.

1.5 Methods

1.5.1 Fracture sampling

In total, 728 fractures have been recorded from the studied ridge in front of the Mediumfjellet Mountain (See Appendix 3). By using the scanline method (e.g. Priest 1993, Ogata et al. 2014) the fracture orientation, spacing between fractures and fracture characteristics have been noted. The fracture data has been combined with bed thickness and bed orientation data for every scanline, with observations being made for all lithology types in the Kapp Starostin Formation being recorded.

The collected fracture data has then been analyzed and presented based on programs such as Stereonet, Excel, Adobe Illustrator and TopoSvalbard.

1.5.2 Fracture analysis

The location of scanlines was chosen to best document the characteristics and distribution of fractures within the mountain ridge, with focus on possible differences between lithologies. The length and number of scanlines varies due to steep and difficult terrain, or scree cover in some areas. Every scanline includes:

Fracture frequency (*ff*)

The fracture frequency is expressed as the number of fractures crossing the scanline for each meter. Each scanline has been measured along a single bed, not crossing beds, and are between 1 and 46 m long. The dataset covers measurements collected both parallel to strike and parallel to dip. Small fractures (cut-off at 10 cm in length) were not taken into account.

Fracture orientations

The orientation of the fractures was measured with a Silva Expedition compass with clinometer using the right hand rule. To best display the fractures strike and dip, they were plotted in a Schmidt net. This is a spherical projection, having equal area, where the fractures are plotted in the lower hemisphere. The fractures orientation (strike/dip) is presented as great circles (planes). Though this is one way to present fracture data, larger dataset are better presented by using poles. In this study, fracture data are presented as both planes and poles. Contour plots are also used, with a spacing interval of 2. The contour plots present the density of fracture orientations (using 1%

Area), where the highest density of poles is shown as the darkest area. Accordingly, brighter areas have a lower density. The software used is named Stereonet9.

The magnetic declination of 6° east of the true north, has not been corrected for in the strike data.

Fracture characterization

The fractures were recorded as either bed-confined or through-going (crossing several beds and lithologies). Further, calcite precipitation or/and slip lineations were noted. True bed thickness was also measured.

1.5.3 Statistical analysis

The collected fracture data is displayed in charts with error bars and standard deviation. This was done in Excel, using the function SDTEV.S. The function bases its calculations on the data collected being a sample of available data. As the orientation of all measurable fractures in the ridge was not collected, the data is characterized as a sample.

1.5.4 Lithology

The mountain ridge has been lithostratigraphically logged, focusing on bed thickness, lithology and mechanical properties (weak or strong). The ridge offers a succession that comprises both carbonates and bioclastic silica beds.

The carbonates were classified after Dunham (1962), modified by Embry and Klovan (1972), and termed mudstone, wackestone, floatstone and rudstone. This classification considers the presence of gravel-size carbonate grains (>2 mm), in addition to the quantity of allochems and micrite (Figure 1.2).

Allochthonous limestone original components not organically bound during deposition				Autochthonous limestone original components organically bound during deposition				
Less than 10% >2 mm components			Greater than 10% >2 mm components		Boundstone			
Contains lime mud (<0.02 mm)		No lime mud		Matrix supported	>2 mm component supported	By organisms which act as barriers	By organisms which encrust and bind	By organisms which build a rigid framework
Mud supported		Grain supported						
Less than 10% grains (>0.02 mm to <2 mm)	Greater than 10% grains							
Mudstone	Wackestone	Packstone	Grainstone	Floatstone	Rudstone	Bafflestone	Bindstone	Framestone

Figure 1. 2: Dunham's classification of carbonate rocks, modified by Embry and Klovan (1972). The classification is based on depositional texture.

1.5.5 Lidarscan

Light detection and ranging scan (LiDar Scan) is a terrestrial laser scanning. This device sends out infrared light, and records the reflected light. The return time of the reflected light is then used to calculate the distance to the scanned reflective surface, from which a cloud of reflections allows a 3D surface to be designated (Wehr and Lohr 1999).

By using a lidar scanner attached to a helicopter data was collected for this study. Accompanying the lidar scan was a high-resolution digital camera (to obtain the true colors of the mountainside), a Global position system (GPS) and an inertial measurement unit (IMU) (Buckley et al. 2008a). The data acquisition was conducted with a helicopter of model AS350B as a platform. The images were taken approximately perpendicular to the topography, and had an overlap of ca. 70%. The overlap ensured that the whole area was covered (Buckley et al. 2008a). When processing the data, the high-resolution photos were rectified onto the DEM-model (derived digital elevation model) that was made out of a laser point cloud (Buckley et al. 2008b). Geological interpretations are done in the software LIME, in which marker beds and other distinct beds are mapped and analyzed. By measuring the bed's original length versus current length, it is possible to address the extent of Layer-Parallel-Shortening (LPS) in the Kapp Starostin Formation.

Table 1. 1: The table gives information about the datasets, produced from the Lidar scan at Mediumfjellet. Modified from Larsen (2009).

Mediumfjellet	
Laser scan components:	
Riegl LMS Q240i-60 airborne laser scanner	
Hasselblad H1 22mp camera with 35 mm lens	
iMar iIMU-FSAS inertial measurement unit	
Dual frequency GPS	
Parameters of the dataset:	
Measurement rate	10 kHz
Pointspacing	1.5 m
Accuracy	0.1-0.15 m
Number of datapoints used	c. 8 m
Number of triangles in top level	c. 16 m
Number of levels	9
Number of images	c. 500
Size of area	7 km x 3 km x 800 m

1.5.6 Thin sections

In order to further understand the details of the lithologies in the succession, rock samples were collected for thin sections. Irina Maria Dumitru (University of Bergen) made the 11 thin sections used in this study.

For analysis, a microscope with camera was used, eclipse E400 POL microscope with a mounted Nikon, digital sight DS-U3 camera. All photos are taken with 4x zoom in cross-polarized light.

In total five thin sections were prepared for in depth study in a scanning electron microscope (SEM) by removing the varnish that has been applied on top of the rock to better preserve it. After the varnish is removed, the thin sections have to be grinded once more to remove any traces of the varnish; ~6 micron is removed. The grinding is done by hand on a Struers DP-U2, where both diamond spray and DP-Lubricant are applied. The thin sections are provisioned for electron microscope by coating them with carbon. This is done in an Agar Turbo Carbon Coater machine, before they are studied in SEM, of type Zeiss Supra 55VP.

CHAPTER 2 GEOLOGICAL SETTING

2.1 Regional setting – geological history of Spitsbergen

Svalbard is a small, elevated part of the Barents Shelf, representing a unique locality for geologists and a playground for those interested in petroleum-related geology.

Being located in the northwestern part of the Barents shelf, it shares a similar but not identical geological history as the rest of the shelf. For instance, not all formations can be directly correlated across the whole shelf. The Barents Shelf is an intra-continental platform with a passive margin setting through most of its history, offering an evolution that can be followed from mainland Norway to north of Svalbard, and all the way east to Novaja Zemlja. Moving west of Svalbard, the shelf tapers sharply and turns into a deep marine basin, dominated by highly-oblique active seafloor spreading (Faleide et al. 1991).

As a response to plate tectonics, the Svalbard archipelago have been drifting northwards since the beginning of the Paleozoic and continues to do so. The journey that started close to the South Pole some 600 Ma ago has made the geological history of Svalbard long and diverse. Accordingly, climate changes have been enormous throughout the Phanerozoic Eon, which can be seen in the sedimentological archive (Dallmann et al. 1999).

Spitsbergen is made up of rocks spanning from Precambrian to Tertiary age. Examples of the older evolution include Neoproterozoic till deposits, thought to be deposited at ca. 600 Ma (Birkenmajer, 1975). The crustal uplift in Late Mesozoic and Cenozoic times resulted in erosion, which removed the entire upper Cretaceous leaving a distinct hiatus. This can be ascribed to two major events; (i) the High-Arctic Igneous Province impacting the area (Diabasodden Suite of Svalbard; (Senger et al. 2014) followed by rifting in the north (two events of Cretaceous and Paleogene age), causing regional uplift of Northern Svalbard and a general south tilt, and (ii) Paleogene FT-Belt formation with localized uplift especially in the west, followed by Oligocene rifting leading to rift-shoulder uplift in western Spitsbergen. Although parts of the stratigraphy are missing, this uplift of Svalbard and the northwestern Barents

Sea makes it possible to observe the once deeper buried strata in outcrops. They allow detailed study of the geological history, including numerous orogenies, such as the Grenvillian (late-Mesoproterozoic), Caledonian (Ordovician-Silurian), Svalbardian (Late Devonian), Variscan (Mid-Carboniferous) and Apidic (Early Tertiary) (Dallmann, 1999). The main fault zones of Spitsbergen are oriented NNW-SSE, and are believed to have their origin linked to the Caledonian Orogeny (Harland et al. 1997). These fault zones have been reactivated several times, first in the Devonian to Carboniferous (McCann and Dallmann, 1996), and then again during the Tertiary (Maher et al. 1997).

This study relates to impacts of the Tertiary Fold and Thrust Belt (FT-Belt), and will focus on deformation structures caused by contractional tectonics. As a background, the geological periods of Spitsbergen are summarized, introducing a general framework of the evolution of the region. This is of relevance as structural elements and stratigraphy may have influenced the FT-Belt structural styles that are observed in the rocks of the study area. As a start on the regional setting Figure 2. 1 shows a geological map of Svalbard marking major structures and outlining the general distribution of metamorphic basement and sedimentary basins.

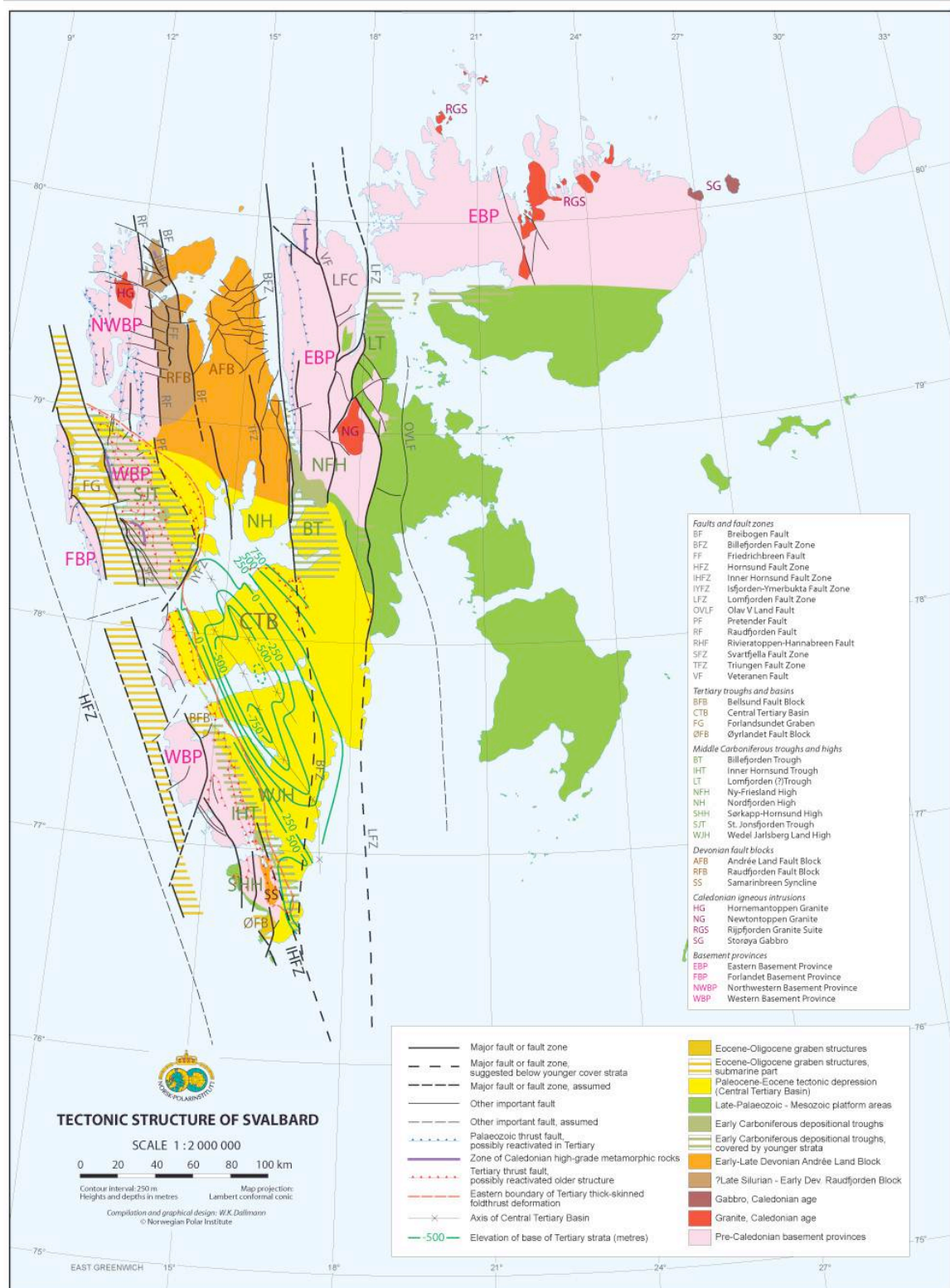


Figure 2. 1: Tectonic map of Svalbard, focusing on the major structures. Notice the size of the Tertiary foreland basin system (yellow) and the basement exposure along the west and north coast of Spitsbergen. Map from the Norwegian Polar Institute.

2.2 Previous work

The name Spitsbergen was given by the captain Willem Barents, when he first saw the island in 1596. The name attests to the high and sharp peaks that rise up towards you, when arriving the seaway. However, he did not know that the island had been mentioned earlier as Svalbard (cool coast) in the *Islandske Annaler* of the Vikings, though there is no direct evidence of vikings visiting the islands (Harland et al. 1997).

The first known geologist that visited Spitsbergen was the Norwegian geologist Keilhau in 1827. The polar explorer Nansen continued the scientific work during his expedition in 1895 and 1896 (Ramberg et al. 2006). The 19th century was dominated by exploring Swedish geologists and, among them probably the most important; Nordenskiöld. Nordenskiöld, together with Loven, Nathorst and De Geer established the stratigraphic framework of Spitsbergen (Nathorst 1910). The discovery of coal was important for further investigation in the 20th century. Expeditions first led by Isachsen and later by Hoel resulted in a better understanding of the island and important new knowledge.

In more recent times, the most prominent geologist must be Harland. Especially relevant are his studies of the major NNW-SSE trending lineaments, and their link to the Caledonides. He was also a pioneer in the exploration of the Tertiary FT-Belt. His work inspired those of Birkenmajer (1972), Kellogg (1975) and Steel et al. (1981), neatly summarized in Steel and Worsley (1984) which offers the first comprehensive, modern analysis of Spitsbergen's sedimentary basins. With the onset of petroleum exploration that culminated in the 1980's, a wealth of detailed studies came along. The current understanding and ongoing research is to a large degree based on exploration-related accounts of the 1990's, especially around the FT-Belt, which are further discussed in Chapter 2.3 and 2.4.

2.3 Spitsbergen's main geological periods

2.3.1 Basement

The basement of Svalbard has been termed Hecla Hoek, and this term has been used for all the rocks older than Devonian (Dallmann, 1999). The oldest rock ever found in Svalbard offers zircon dated to an age of 3,3 Ga, and was sampled in the northwestern part of Spitsbergen (Elvevold et al. 2007). Basement is exposed as a belt along the west and north coast of Spitsbergen, at Ny Friesland and the northern part of Nordaustlandet (Harland et al. 1997). The rocks representing Hecla Hoek are mainly of igneous and metamorphic character, with abundant meta-sediments, and show evidences of several orogenies. The oldest well-established event is dated to be from ca. 1700 Ma, but evidences of orogenesis around 1000 Ma (Grenvillian) and 600 Ma (Baikalian) have also been found (Dallmann 1999, Worsley 2008). These are followed by the Caledonian Orogeny, during the Silurian to Devonian, at a time when Spitsbergen was connected to Greenland as part of the Pangaea and was positioned close to the equator (Dallmann 1999). This orogeny caused increased magmatic activity, and these Silurian intrusions make up today's higher peaks; for instance Svalbard's highest mountain, Newtontoppen (1717 m asl.), which is composed of late Silurian granite (Elvevold et al. 2007).

2.3.2 Old Red (Devonian)

"The old red sandstone" is a term used for Devonian rocks in Svalbard, as a fitting name for parts that offer a strikingly red succession. These rocks consist mostly of siltstones and sandstones, and conglomerates alternating with some shales and carbonates. The striking red color is due to high concentrations of iron oxide (hematite) mainly as grain coating, typical for a hot, arid climate. These types of sediments provide information about the climate at that time, and are suggested to be deposited in dry desert-like areas (Elvevold et al. 2007). Svalbard's Devonian basin is poorly understood compared to its counterparts of mainland Norway. For Svalbard, accounts point to a combination of a high erosional rate, and an extensional phase that led to the collapse of the Caledonian orogeny. Several graben-systems developed along fault zones, and sediments that make up the Devonian rocks were deposited in fault-bound basins (Worsley 1986, Harland et al. 1997). In this context, the more recent account of Braathen et al. (2011) links the Svalbard Devonian basin to an

extensional detachment, the Keiserhjelmen detachment. These authors advocate a tectonic setting and evolution for the basin linked to late-orogenic collapse of the Caledonian mountain belt, offering a closer link to the basins of mainland Norway. A similar discussion is presented by Nystuen et al. (2008) in the Making of the Land.

Younger Devonian rocks are noticeably different in color, being composed of gray lacustrine shales and marine mudstones. The grey color may indicate deposition in more anoxic conditions, which stopped the iron from corroding. Through the Devonian period there has been a change in deposition environment, from terrestrial alluvial conglomerates and fluvial sandstone deposits, to grey lacustrine shales and marine mudstones, fining upwards. This change has been ascribed to a climatic shift, from a semi-arid to a more humid climate (Harland et al. 1997, Critelli and Reed 1999, Blomeier et al. 2003, Worsley 2008).

Throughout most of Svalbard, the Devonian sediments look like they are mostly undeformed, with low dips of bedding. However, moving closer to the Billefjorden Fault Zone, this changes drastically in to tightly folded layers striking approximately north-south. This deformation links to a major thrusting and basin-inversion event, often termed the Svalbardian event (Bergh et al. 2011), which have been interlinked with a major pulse coarse clastic sedimentation in the southeastern part of the basin.

2.3.3 Late Paleozoic

Through the Carboniferous period, Spitsbergen experienced erosion and peneplanation, subsequently covered by alluvial-fluvial sandstones and coal deposits of the Billefjorden Group. By mid Carboniferous, there was an onset of rifting, with fault activity mostly following old fault zones that had developed during the Caledonian orogeny, such as in the Billefjorden Fault Zone. Extensional rejuvenation of this fault zone caused the formation of a N-S trending half-graben, the Billefjorden Trough (Braathen et al. 2011), which is located some 40-50 km east of the study area addressed in the thesis.

As Carboniferous and Permian rocks are present in the subsurface of the study area, and partly make up the Mediumfjellet thrust sheets, they require a closer inspection. In this period, the climate changed drastically. From a tropical location, Svalbard

drifted into arid and then temperate zones. The sea level was changing with a high frequency, but the overall trend was of sea level rise. In the early Carboniferous a tropical climate was present, with onshore areas consisting of floodplains from Svalbard to Greenland. This environment resulted in sandstones, mudstones and coal with no marine influence, making up the Billefjorden Group. The Carboniferous coal is the same coal that was mined by the Russians in the ghost town of Pyramiden (Gjelberg and Steel 1981, Worsley 2008). The floodplains were eventually flooded during onset of rifting in the mid Carboniferous, giving way to marginal marine to continental environments, today observed as shallow marine evaporites, dolomites and limestones, interfingering with sandstones and shales. These deposits are well exposed in the graben making up the Billefjorden Trough, but are thin or non-existent outside this and other similar basins.

Late Carboniferous and Early Permian times are characterized by relatively stable platform conditions, dominated by carbonate deposition, with little siliclastic input to the deposit system that makes up the Gipsdalen Group. The unconformity between the Billefjorden Group and the Gipsdalen Group indicates a major regional uplift and a shift to warm and arid climate. Early Permian units are characterized by limestones and evaporites, found in the Wordiekammen and Gipshuken formations (Steel and Worsley 1984, Worsley 2008). The Gipshuken Formation is mainly comprised of evaporites and carbonates deposited in a warm and arid climate. The evaporites were deposited in a sabkha environment, while the carbonates were deposited in a shallow marine environment, indicating sea level fluctuations (Worsley 2008). The Gipshuken evaporites are important in this study, as they represent the detachments at Mediumfjellet (Chapter 2.5).

In the Middle Permian, Spitsbergen experienced a shift to temperate climate. Subsidence and continental drift had made the shallow platforms deeper and colder. Rocks representing this age are mudstones, sandstones and limestones. The following Middle - Late Permian succession of the Kapp Starostin Formation is known for its spiculitic layers, which are highly resistant to erosion. These layers can easily be seen in outcrops and on seismic data, and are known as the Røye and Ørret formations in the Barents Sea (Rafaelsen et al. 2008). The transition of highly siliceous units in Late Permian, to the non-siliceous shales and mudstones of the Sassendalen Group in Early

Triassic marks a dramatic change. A theory is that a suddenly heating of oceanic waters was one of the leading factors for the Late Permian mass extinction (Worsley 2008).

Tempelfjorden and Billefjorden with its plateau-shaped mountains are some examples of Carboniferous and Permian deposits that are well exposed (Elvevold et al. 2007). The Mediumfjellet massive is made up of these units; and are therefore the rocks that are studied in this thesis.

2.3.4 Mesozoic

Several regressive and transgressive sequences are present from the Triassic throughout the Cretaceous, while the platform continued to be relatively stable. Deposition reflects a shallow to deep marine environment, made up of thin-bedded shale and sandstone (Steel and Worsley 1984). The climate was temperate and humid, and Svalbard drifted from 35°N in the Late Permian to 60°N in the Early Cretaceous. Mesozoic rocks are exposed in central, southern and on the eastern parts of Spitsbergen, as shown in Figure 2.1 (Elvevold et al. 2007, Worsley 2008).

Moving into the Cretaceous, the first phase of seafloor spreading started in the Arctic Ocean/Basin, which resulted in uplift and erosion in the north. This uplift coincide with the so-called HALIP – High Arctic Large Igneous Province (Maher Jr 2001) event seen as magmatic activity in the High Arctic area (Tarduno et al. 1998, Tarduno 1998). Intrusions from this event can be seen in Permian rocks (Birkenmajer and Morawski 1960) as those present in Mediumfjellet. It is possible to see most of the Early Cretaceous succession on land on Svalbard in the south. Moving from the south towards the north the Cretaceous layers pinch out below a very low angle unconformity. Because of the opening of the Arctic Ocean in the Late Cretaceous, magmatic activity caused uplift of the northern part of Spitsbergen by more than 1 km, and Late Cretaceous strata is missing on Northern-Central Svalbard today (Faleide et al. 1993, Dallmann et al. 1999).

In the Paleogene, rifting reoccurred in the north, in parallel with dextral transform plate-boundary movements between Greenland and Svalbard (Dallmann et al., 1999).

2.3.5 Cenozoic

The opening of the Arctic and North Atlantic oceans created complex structures, among them the Tertiary Fold and Thrust Belt of Spitsbergen. Older rocks were folded, and a mountain belt developed, associated with a foreland basin system (Harland 1969, Lowell 1972, Talwani and Eldholm 1977, Steel et al. 1985, Maher et al. 1997). Harland (1965,1969) was the first to come up with a theory for the Tertiary tectonics, which is further discussed in *Chapter 2.4 The Tertiary Fold and Thrust Belt*.

The most obvious part of the foreland basin system is the Tertiary Central Basin. Sandstones, shales and locally some very organic rich layers (coal) were deposited, today dominating the geology in the central parts of Spitsbergen (Elvevold et al. 2007). After termination of folding and thrusting, with linked foredeep subsidence, no rocks were deposited, or rather preserved until the Quaternary. The exception is some Oligocene basins along the west coast. The ice age made its appearance in the Neogene. Continuous glacial periods has transformed Svalbard into what we know it as today, where as much as 60% of the archipelago is covered by glaciers (Elvevold et al. 2007). Harland et al. (1997) suggest that Spitsbergen has been uplifted close to 3000 m, due to isostatic uplift through Neogene. Accordingly, parts of Svalbard have experienced significant unroofing.

2.4 The Tertiary Fold and Thrust Belt

The Tertiary Fold and Thrust Belt (FT-Belt) are located along the western part of Spitsbergen, from NW of Kongsfjorden to south of Sørkapp (Faleide et al. 2008). The age of the tectonic event is poorly constrained, but likely of Paleogene age (Maher et al. 1995). Traces of this tectonic event can today be seen as a 100-200 km wide zone, making up a taper that thins towards the east (Braathen et al. 1999). Studies by Wennberg et al. (1994) suggest a WSW-ENE shortening of at least 35%, while Bergh et al. (1997) suggest a 45% shortening, using the Kapp Starostin Formation as a marker. This implies a shortening of minimum 20-25 km. It is also suggested that the FT-Belt experienced in-sequence thrust development, rooted in detachment horizons towards the foreland. Out-of-sequence thrusts developed at a later stage (Wennberg et al. 1994).

The FT-Belt was formed as a response to dextral transform movements between Greenland and Spitsbergen (Harland 1969, Leever et al. 2011). These plate movements involved relative movement of three plates; Eurasia (Spitsbergen and the Barents Sea), Greenland and North America. In the late Paleocene Greenland separated from the North American plate and became an independent microplate. This was a consequence of the ongoing spreading in the Norwegian–Greenland Sea. The spreading in the Labrador Sea later in early Oligocene led to further motion of the Greenland and North American plate (e.g. Rowley and Lottes 1988, Engen et al. 2008, Gaina et al. 2009). As a result of the Tertiary plate motion with the opening of both the North Atlantic Sea and the Arctic Sea, Greenland and Spitsbergen became separated by a transform fault, which experienced temporal transpression. The zone between these two continents developed the FT-Belt. Later transtension started at approximately 37 Ma. New ocean floor developed because of the seafloor spreading that progressed north, and resulted in the opening of an ocean between Greenland and Spitsbergen, the Greenland Sea (Harland, 1969).

Later work on the Spitsbergen FT-Belt, addressing its kinematic evolution, timing, and deformation zones is found in (Lowell 1972, Talwani and Eldholm 1977, Steel et al. 1985, Maher et al. 1995, Bergh et al. 1997, Braathen et al. 1999, Maher et al. 2001).

2.4.1 Deformation provinces

The Fold and Thrust Belt (FT-Belt) of Spitsbergen have been subdivided into different zones. For instance, Braathen et al. (1999) divided the FT-Belt into four zones of different tectonic styles, from west to east (Figure 2. 2). The first zone (1) is the western hinterland zone, dominated by basement. This is the most deeply eroded part, with several Tertiary grabens, forming sedimentary basins (Braathen et al. 1999). One of these grabens is the Forlandssundet Graben with a 5 km thick package of sediments (Steel et al. 1985). It was created mainly between the Eocene to Early Oligocene and consists of alluvial, shallow marine and deeper marine deposits, which are slightly deformed (Gabrielsen et al. 1992). Studies show that Forlandssundet Graben originated in a transpressional regime, which later turned into a transtensional regime (Leever et al. 2011). Within this zone is the Svartfjella-Eidembukta-Daudmannsodden lineament (SEDL), which is a 35 km long zone of deformed Carboniferous strata. The SEDL shows traces of both orogen-perpendicular and orogen-parallel movements. The orogen-parallel movements makes it different from the FT-Belt to the east, and is a good indication for a transcurrent component in a transpressive setting (Maher et al. 1997). The second zone (2) is the Basement-involved fold thrust complex. This zone is thick-skinned, with partly rotated steep thrusts. The overall structure in Oskar II Land and Nordenskiöld land is chevron-style folds, monoclines, anticlines and synclines, with a wavelength of up to 5 km. The third zone (3) is called the Central Zone. The folds are open to tight, turning from a thick-skinned to a thin-skinned fold thrust belt. The different lithologies can be seen as a result of the changing of faulting styles within these different types of rocks. The Triassic silt and shales has been tightly folded, while the Triassic – Cretaceous sandy units have more open folds. A stratigraphic step-up, moving from the detachment layer in Gipshuken Formation (Permian evaporites) to the stratigraphically higher detachment zone in Botnheia Formation (Triassic shales), marks the transition from the Central Zone to the Eastern Foreland Zone. It is the Mediumfjellet Mountain with its piggyback sequence that marks the thrust front of this zone. The Eastern foreland province (4) develops into nearly flat lying strata with just a few scattered thrust, and marks the end of where the fold thrust belt had a tectonic impact. The tectonic development has probably been controlled by pre-existing faults, and the zone consists of stacked and imbricated thrust sheets, dipping WSW (Braathen et al. 1999).

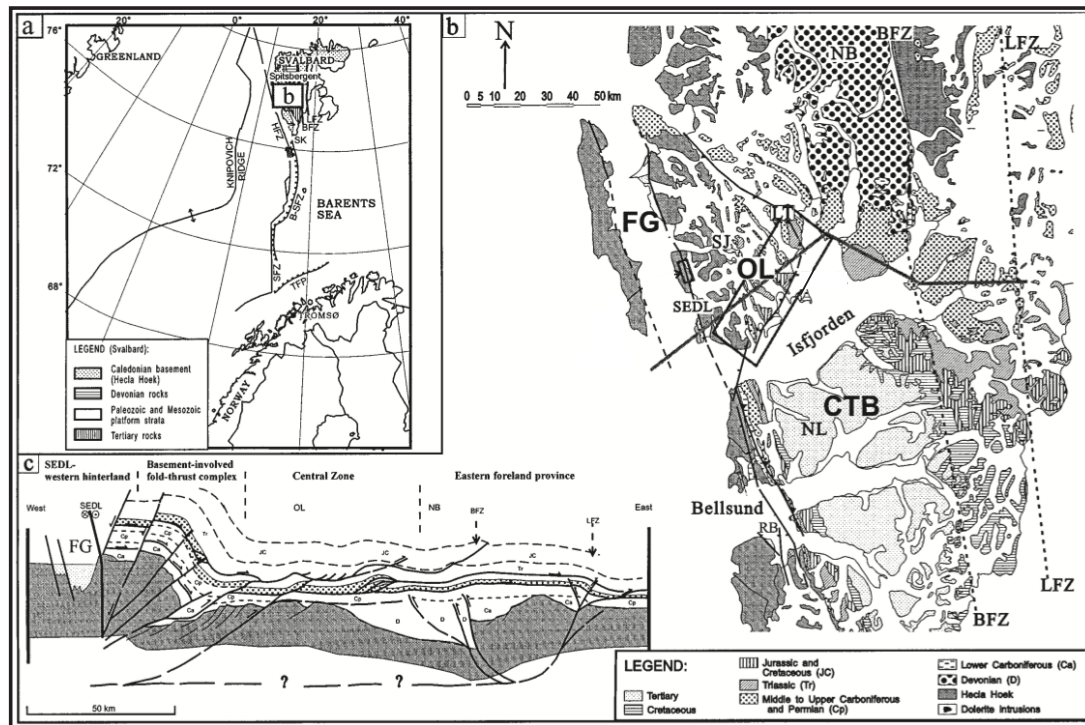


Figure 2. **a)** Regional map, marking the location of Svalbard and the Barents Sea. **b)** Geologic map showing the central parts of Spitsbergen and the location of the cross-section in c. **c)** Schematic cross-section, divided into four deformation zones; the SEDL -western hinterland, the Basement-involved fold and thrust complex, the Central Zone of thin-skinned deformation and the Eastern foreland province of barely deformed strata (modified from Braathen et al. 1999).

In contrast to the four zones previously described, papers by Bergh et al. (1997), Kellogg (1975) and Wennberg et al. (1994) subdivide Oscar II Land into 3 zones; the Western Zone, the Central Zone and the Eastern Zone (See Figure 2. 3). The Western Zone is the thick-skinned zone, with basement-involved steep thrusts. The Central Zone is a thin-skinned zone with its detachment layer located in the Gipshuken formation. The Eastern Zone has a frontal duplex system, dipping towards the hinterland, where the basal thrust is lying in the Gipshuken Formation. Fault-propagation folds and fault-bend folds are also present. The Eastern Zone is the transition zone between the folded layers in the Central Zone and the sub-horizontal layers in the Nordfjorden block (Bergh et al. 1997). While the Mediumfjellet marks the thrust front, and the transition from the Central Zone to the Eastern foreland province in the model of Braathen et al. (1999), the characteristic mountain are positioned into the Eastern Zone of the model of Bergh et al. (1997).

Regardless of what theory is used, a summary would approximately be that there is deep and highly tectonised rock in the western part of the FT-Belt. Moving towards the foreland (eastwards), the deformation is going from a thick-skinned (in the

hinterland) to a thin-skinned (in the foreland) deformation. East of Mediumfjellet, is the sedimentary succession barely deformed, indicating the end of tectonically impacted rocks, and thus the end of the FT-Belt.

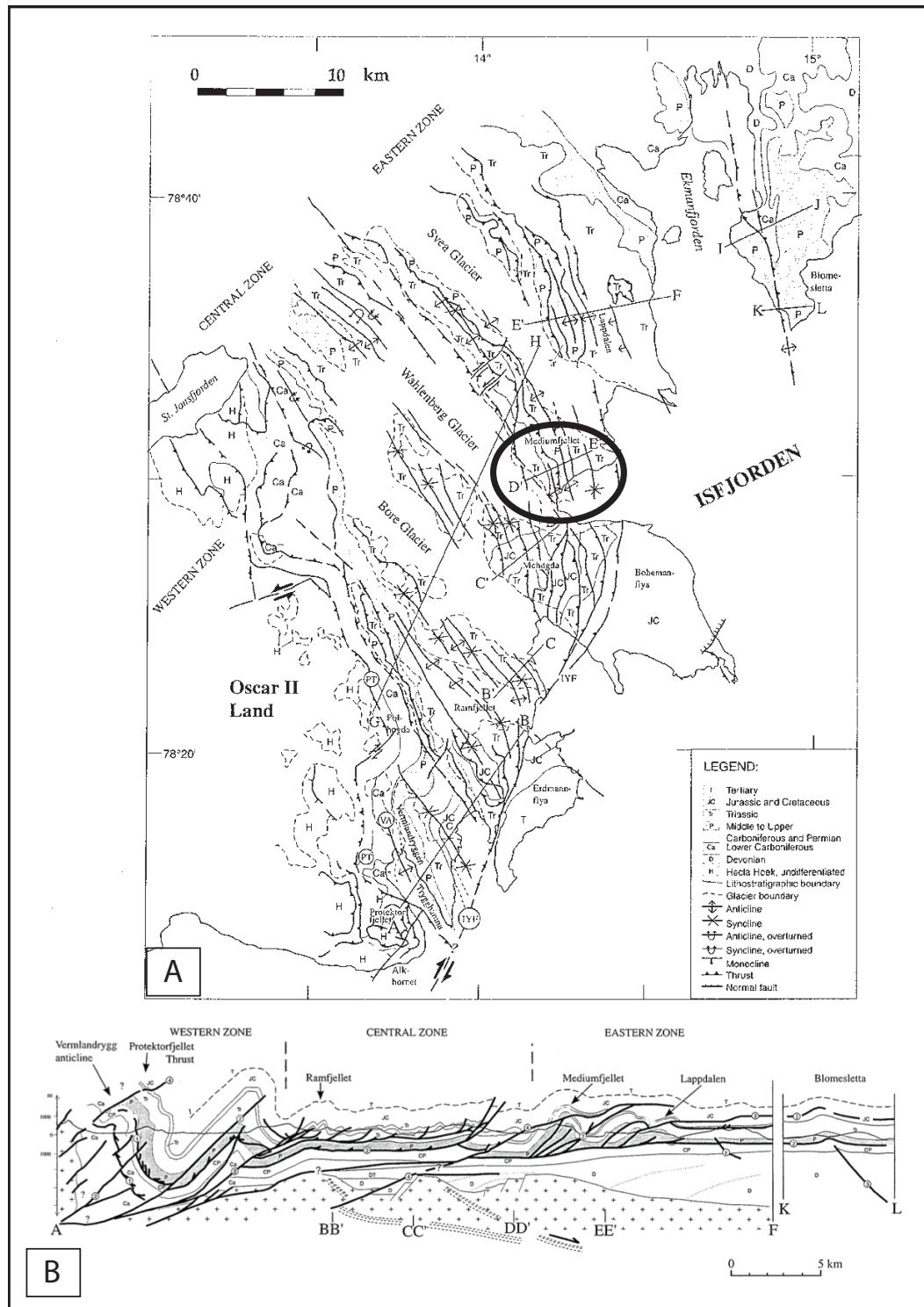


Figure 2. 3: **A)** A structural map of Oscar II Land, Spitsbergen. The study area lies within the circle. IYF = Isfjorden-Ymerbukta fault; PT = Protektorfjellet thrust; VA = Vermlandryggen anticline. **B)** A schematic cross-section through Oscar II Land. The cross-sections can be found in the structural map (A). The location of Mediumfjellet is marked with an arrow in the cross-section, here in the Eastern zone (modified from Bergh et al. 1997).

2.4.2 Kinematics

The kinematic evolution of the FT-Belt has been divided into 5 stages; Stage 1 is the beginning of compression. Northward directed shortening resulted in rocks being pushed along a decollement zone creating a wedge. A zone of weakness was created for later fold and thrust belt development (Braathen et al. 1999). Stage 2 and 3 is the main shortening events, making a WSW-ENE shortening. Crustal thickening created a supercritical wedge in the hinterland, build up of basement and cover rocks (Braathen et al. 1999). In-sequence thrusting in detachment horizons also developed. Further shortening resulted in out-of-sequence thrusting, probably the reactivation of deep old thrusts (Stage 4). The SEDL is most likely of similar age as the kinematics of Stage 4. Erosion on the earlier formed supercritical wedge caused a critical taper angle (Braathen et al. 1999). The last stage, Stage 5, is characterized by local extension, erosion and sedimentation. As a result of the extension, normal faults developed in the uplifted western part of the FT-Belt. At Mediumfjellet, only stage 2-4 is present (Braathen et al. 1999).

2.4.3 Sedimentary basins

As mentioned in 2.4.1 the FT-Belt are divided into several deformation zones. The deformation zones also include sedimentary basins. The Forlandsundet graben is located in the western hinterland with several smaller basins (Braathen et al. 1999). The orientation and location of the Forlandsundet graben (north-northwest trending) suggests it to be linked to the Svartfjella-Eidembukta-Daudmannsodden lineament. The graben consists of approximately 5 km of Paleogene sediments, and indicates both extensional and strike slip faulting (Gabrielsen et al. 1992, Blinova et al. 2009). The Central Tertiary Basin is located in the Central Zone, east of the FT-Belt, and is seen as the foreland basin. The basin infill of Paleocene-Eocene strata is made up of clastic sediments, with a thickness of up to 2500 m, and termed the Van Mijenfjord group (Steel et al. 1985, Dallmann et al. 1999, Helland-Hansen 2010). The sedimentary succession is folded, with open to gentle folds. It is suggested that it originally was formed as a low-relief foreland basin that was subsiding due to tectonism and sediment load. Eventually the basin got under-thrusted and became a piggyback basin (Braathen et al. 1999, Helland-Hansen 1990).

The timing and development of the FT-Belt has been widely discussed, but overall it is suggested that the FT-Belt is a result of dextral transpression in Paleocene-Eocene

times (e.g. Orvin 1940, Harland 1969, Birkenmajer 1981, Dallmann et al. 1993). Lyberis and Manby (1993), conclude in their paper that the FT-Belt probably is formed in Late Cretaceous by pure compression. Created by the collision between Svalbard and Greenland, instead of dextral transpression as earlier described. This is highly disputed by most others, as little evidence exist for such an early start of deformation, e.g. Maher et al (1995) and Steel et al. (1985) discussed in their paper that different kinds of data shows different age of plate motion. Sea-floor data date the strike slip motion along the Greenland-Spitsbergen plate boundary to be from Late Paleocene time, whereas data from the Central Basin suggest possible strike slip motion from Early Paleocene. However, recent plate reconstructions points towards Paleogene (Worsley 2008).

Other models (Maher and Craddock 1988, Faleide et al. 1988) suggest instead a separation of the contractional and transcurrent elements near the paleotransform fault. The kinematic evolution is divided into five stages, where the first stage started in Late Cretaceous to Paleocene (e.g. Braathen and Bergh 1995, Bergh et al. 1997, Maher et al 1995).

2.5 Mediumfjellet – location of field studies

Mediumfjellet is located to Oscar II Land between Wahlenbergreen and Sveabreen, west of Nordfjorden and NE of Isfjorden. The area marks the thrust front, and in the classification after Braathen et al. (1999) of the Tertiary Fold and Thrust Belt is this the transition from thin-skinned deformation in the Central Zone, to barely deformed strata in the Eastern Zone. This transition zone is called the Mediumfjellet – Lappedalen area, and consists of Paleozoic and Mesozoic rocks that are deformed and thrust, making up a thrust front in the Nordfjorden block (Bergh and Andresen 1990). The Mediumfjellet-Lappedalen area is restricted to the east by the Lappedalen thrust and to the south by the Isfjorden transfer fault (Braathen et al. 1999). The deformation is typically thin-skinned, and the thrust front has a gentle dip towards the west (Bergh and Andresen 1990). In the Lappedalen area the major thrusts are named L1, L2, L3 and U (Umefjell), while M1, M2, M3 and G (Gavltinden) are thrusts that can be found in the Mediumfjellet area (Bergh and Andresen 1990). The field area is located at Mediumfjellet, and only thrusts situated in this area will therefore be described further.

M1-thrust

At Mediumfjellet, M1 is the easternmost thrust. M1 marks where moderate to steeply dipping Triassic and Permian strata overlies nearly flat-lying Triassic strata. The steeply dipping strata are a part of the eastern forelimb of a major anticline, located in the hangingwall of M1. The M1-thrust is suggested to be a footwall low-angle-to-bedding to flat thrust that cuts the forelimb of the anticline located in the hangingwall. This thrust seems to have grown out from another thrust beneath Mediumfjellet, termed the M2-thrust (Bergh and Andresen 1990, Larsen 2009).

M2-thrust

The M2 thrust is located within the Gipshuken Formation, and end up with its tip line in the anticline center of a fault-propagation fold (Bergh and Andresen 1990).

M3-thrust

The westernmost and also the oldest thrust of M1, M2 and M3, is the M3 thrust. This is the steepest dipping and structurally uppermost thrust, which is suggested to have developed as a flat. The thrust cuts through both the Gipshuken Formation and the

Kapp Starostin Formation, and puts Gipshuken Formation on top of Triassic rocks. Both the Triassic and Permian strata are dipping towards SW. In the hangingwall block is a major anticline present, described to be a broad box/chevron-type in the northern part, while the southern part have tight chevron and box parasitic structures, related to the major anticline. The M3-thrust is interpreted to be a fault-bend-fold (Bergh and Andresen, 1990). Reconstructions of the M3 thrust shows that the minimum displacement is estimated to be 700 m at Mediumfjellet's southern flank. Moving 3 km north, the displacement is reduced to 200 m (Bergh and Andresen 1990).

The three thrusts M1, M2 and M3 all seems to make up flat-ramp fault propagating thrust systems. M2 and M3 are responsible for the two major anticlines, which could be linked to major footwall ramps. In the southern part of Mediumfjellet these anticlines are interpreted to be fault propagation folds, which further north changes into box/chevron fold geometries that are consistent with fault bend fold formation (Bergh and Andresen 1990).

G thrust

The last major thrust is the G thrust (Gavltinden thrust), located west of M3, which is cutting both Triassic and Permian strata. The thrust are dipping 20-25 ° west (Bergh and Andresen 1990) and is interpret to be an out-of-sequence thrust as it cuts both limbs of an anticline (Morley 1988). The Gavltinden thrust has a minimum displacement of ~ 1 km. This thrust is likely a separate and much younger thrust system, cutting down-section through earlier formed fold and thrust sections (Bergh and Andresen 1990).

A two-stage model can explain the development of the Mediumfjellet-Lappedalen thrust front. Stage 1 is the creation of a fold-thrust system. The thrusts are in-sequence (M1, M2 and M3), propagating eastward (piggyback) with ramp-flat thrust geometries. Associated to the thrusts are fault-bend and fault-propagation folds in the hangingwall. In stage 2 a more complex hinterland develops, with out-of-sequence thrusts (OOST) and formation of a duplex system (Bergh and Andresen 1990). This event is likely linked to the OOST at Mediumfjellet (G) and Lappedalen (U) (Bergh et al. 1997).

CHAPTER 3 CONCEPTS OF FRACTURE SYSTEMS IN FOLD THRUST BELTS

3.1 Introduction

The focus of this chapter is on the concepts of fracture systems as a background for the study, including relevant earlier work. Herein there is a short but informative description, referencing key literature. This forms the background for the sedimentological and structural descriptions in Chapters 4 and 5, and the discussion in Chapter 6.

This chapter has a similar layout as the discussion, starting with large-scale structures; thrusts and their related folds, which can be at km-scale in size. Then the focus shifts to more detailed and small-scale structures, such as mm to meter scale fractures. The final part connects the large- and small-scale structures, focusing on how they influence each other and fluid flow.

3.2 Fold and thrust geometries

3.2.1 Thrust systems

According to Butler (1982), thrust faults that originate from the same detachment zone are seen as a thrust system. A detachment zone, or a décollement zone, is the main fault that has detached the overlying volume of rock from the volume of rock below the fault (Boyer and Elliott 1982, Butler 1982, McClay 1992). Three different end-member types of thrust systems can be distinguished; i) imbricate fans, ii) duplexes and iii) triangle zones. An imbricate fan has closely related thrusts nucleating from the same detachment zone, but not necessarily developing at the same time. The thrust system has a floor thrust as root to thrust ramps and could be either leading edge (largest displacement towards the hinterland) or trailing edge (largest displacement towards the foreland). Duplexes are closely spaced thrusts bound by both a floor thrust and a roof thrust, hosting bodies of rock enclosed by thrusts on all sides (horses). There are several types of duplexes, but the most common ones are either hinterland-dipping or foreland-dipping duplex systems (McClay, 1992).

The triangle zone is included as a third end-member thrust system by McClay (1992). This type of thrust system develops when two thrusts of opposing vergence share the same detachment zone, together creating a triangular zone.

The thrusts in a thrust system will not develop simultaneously, but in an order or sequence. A forward breaking sequence has its youngest thrust at the front, while a break-back sequence has the youngest thrust closest to the hinterland. If a thrust does not obey this order, it is called an out-of-sequence thrust (McClay 1992, Morley 1988). At Mediumfjellet, both in-sequence and out-of-sequence thrusts are present (see Chapter 2.5). A piggyback sequence can be seen in the southern front of Mediumfjellet (facing Nordfjorden). A piggyback sequence is a type of leading imbricate fan, where the youngest thrust jack up the older ones and give the thrusts different dips in a fan-shaped geometry. This results in that the dip of bedding related to the thrusts, increasing from younger to older structures (Boyer and Elliott 1982, McClay 1992).

3.2.2 Thrust geometry

Fold and thrust belts commonly have both thick-skinned and thin-skinned elements. The thick-skinned part is basement involved, and in many cases shows more complex deformation. Thin-skinned thrusting only involves cover rocks (McClay, 2004); this is the system present in the field area. A thrust belt is built up of several thrust sheets, each of which is a volume of rock transported above an underlying thrust fault (McClay, 1992). The geometry of thrusts is that of flats and short ramps with flats that follow weak layers like evaporites or shales. Where the thrust propagates towards an obstacle or more competent rock, it normally makes a step up and thereby creates a ramp that cuts across the stratigraphy up to a higher weaker horizon. According to McClay (1992) there are mainly three types of ramps; lateral ramps, frontal ramps and oblique ramps (Figure 3.1). A lateral ramp has reverse-oblique to strike slip movement and is oblique to the overall transport direction. A frontal ramp is positioned perpendicular to the transport direction, with a dominating up-dip movement. An oblique ramp strikes oblique to the transport direction. Geomechanic constraints dictate that all thrust ramps should have a dip angle of 10-30°, depending on shear strength of rocks (McClay, 1992).

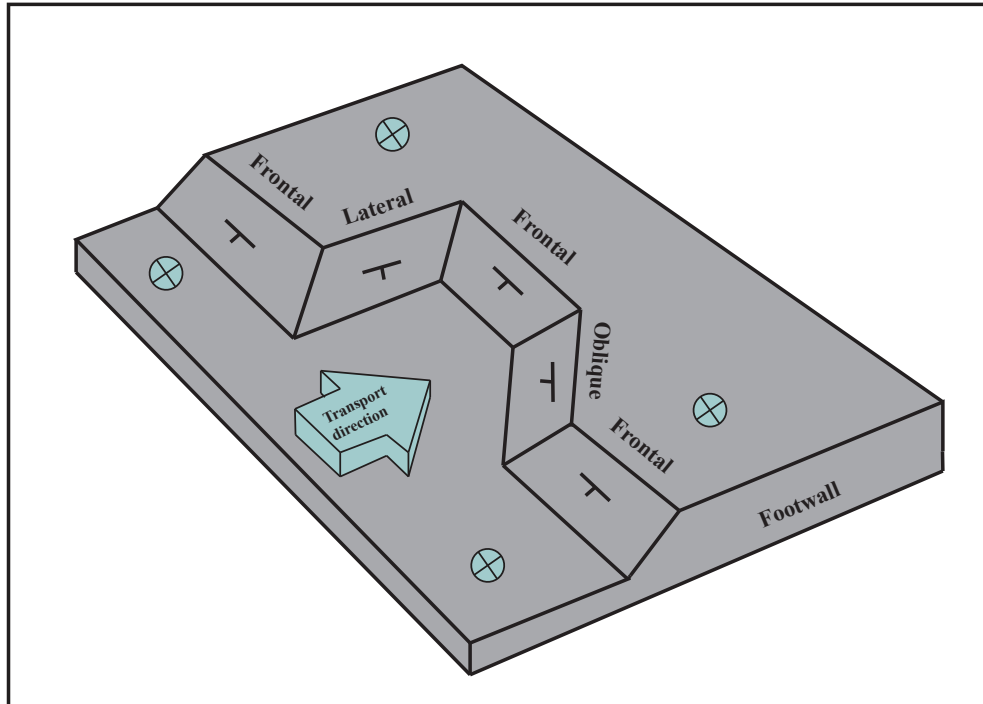


Figure 3. 1: Illustration of the different ramp geometries. A ramp can either be frontal, lateral or oblique (modified from Wilkerson and Marshak 1997, Wilkerson et al. 2002)

A thrust surface is not planar, but more commonly curved, reflecting growth of thrust segments into a composite thrust (Ray, 2006). This means that the thrust morphology will show a ridge-and-furrow appearance, and its map view will accordingly show curves (Figure 3.2a). Ridges parallel to the transport direction may have an influence on later displacement, while the ridges oriented at a high angle to the transport direction will work as barriers and in many cases lead to fault-bend-folding (Figure 3.2b) (Ray, 2006).

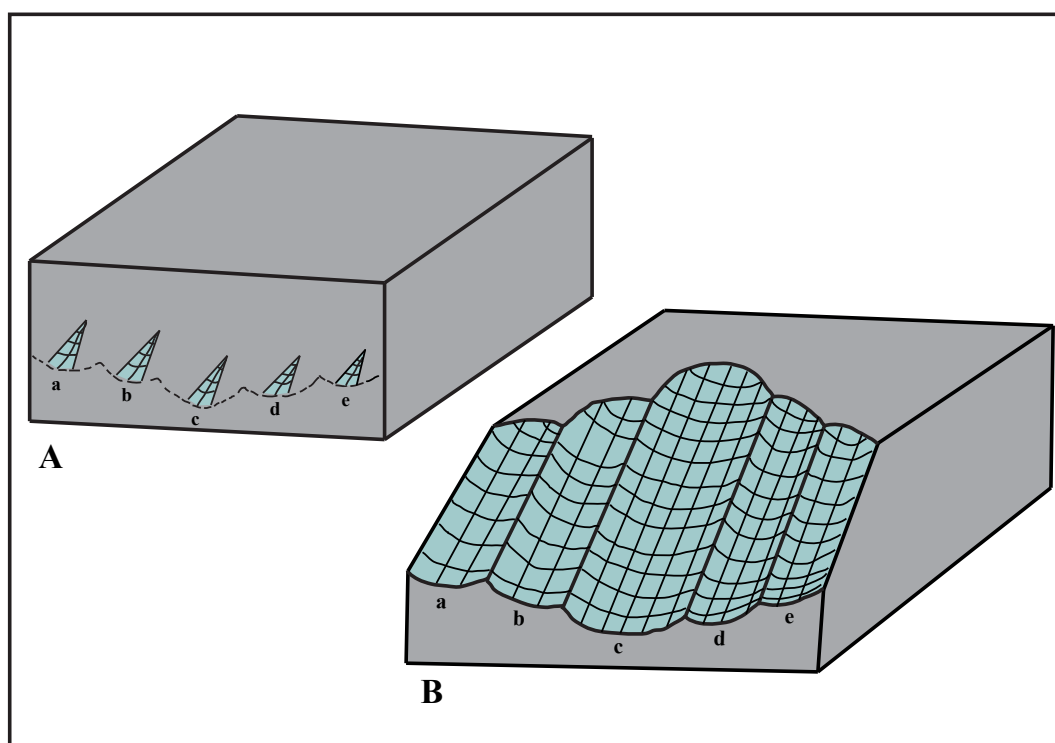


Figure 3. 2: Schematic model showing the impact of fault growth for the geometry of a thrust. **A)** Early stage of fault growth, where several small fault segments (a-e) have nucleate. **B)** At a later stage the small faults in A has grown to interlink, developing ridges and troughs, (modified from Ray, 2006).

3.2.3 Thrust related folds

A fold is created when rock respond to stress by flexing for instance above a fault (e.g. Shaw et al. 2005). The axial plane of a fold is not spatially fixed; it is able to migrate throughout the deformation event. Important folding mechanism will be passive folding, active folding (buckling), bending, and flexural folding. If the layers in a folded multilayered unit have no mechanical influence on the fold shape, it is called a *passive folding*. If a passive fold is produced by simple shear, it is called a shear fold, but this type of folding is not restricted to simple shear. If the multilayered unit is made up of layers with different mechanical properties (contrasts in viscosity), it is termed an *active folding (or buckling)*. While the force is parallel to the layering during buckling, the force has an oblique angle to the layering during *bending* (Donath and Parker 1964). Flexural folding can contribute to both active and passive folding, and are divided into *flexural slip*, *flexural flow* and *orthogonal flexure*. Where there is slip along layer interfaces during folding, there is flexural slip folding. In this case the slip is proportional to the dip of the limb. Where there is response in individual grains rather than on bedding interfaces, it is called flexural flow. Both

flexural slip and flexural flow have decreasing strain towards the hinge zone, while the strain pattern by orthogonal flexure is distinctively different. This type of fold mechanism stretch the outer part of the folded layer, while the inner part gets shortened (e.g. Donath and Parker 1964, Ramsay 1967, Shaw et al. 2005).

There are three main types of folds related to thrusts; i) fault-bend folds, ii) fault-propagation folds and iii) detachment folds; all types are assumed to have a constant volume (Figure 3.3) (Suppe 1983, Suppe and Medwedeff 1984, Jamison 1987, Mitra 2003). Fault-bend folds is caused by the fold mechanism bending, and develop as the volume of rock in the hangingwall is transported over younger strata in the footwall, by a thrust climbing up a ramp and turning into a flat. As the strata are transported up and over the ramp, they must flex to fit the flat-ramp-flat structure (Jamison, 1987). Especially Suppe (1983) shows the geometry of fault-bend folds; there are two fold pairs. One pair is fixed (B and B') while the other pair has travelling hinges (A and A') (see Figure 3.3). Both pairs consist of one anticline and one syncline. The backlimb of the fold is parallel to the footwall ramp (hangingwall flat), normally with a 25-35° dip, while the forelimb is shorter with a steeper angle (hangingwall ramp). The total rotation of the beds moving from the backlimb to the forelimb is twice the ramp angle. The rotation happens while moving from flat to ramp (the ramp angle), and again when moving from ramp to flat (ramp angle) (Shaw et al. 2005). This makes the strata in the hangingwall folded, while the footwall is undeformed (Suppe 1983, Jamison 1987).

Fault-propagation folds develop when thrust displacement diminishes along a thrust ramp and deformation is transferred into undeformed strata above the thrust (see Figure 3.3) (McClay, 1992). The fold develops at the thrust fault's tip (Mitra, 1990). Unlike the fault-bend fold, the folds in a fault-propagation fold develop simultaneously with the thrust. The folds have a vergence in the same direction as the thrusting and tend to be asymmetric with one steep limb (forelimb). The propagating fold will change in size as it grows, while the geometry and position relative to the fault tip is constant (including hinge line and cut-off line). Displacement on the fault decreases towards the fault tip (Suppe and Medwedeff, 1990). Mitra (1990) suggests that open folds give relative thickening of stratigraphically higher units, while tight folds are seen to have a relative thinning of these units. An important parameter for

the fold geometry is the angle of the ramp. High angles give upright and open folds, and low angles give overturned and tight folds. While open folds have material transported into the forelimb from the crest, the material in tight folds are transported from the forelimb into the crest (Salvini and Storti, 2001).

The above description of fault-propagation folds fits a kink-style type of fold; however there is an alternative way of explaining folds that does not fit with this classic geometry, called trishear. The trishear is a triangular shear zone (in profile) that distributes the strain through the whole zone. Because of this distribution the beds are stretched and thinned, causing the hinges of the folds to be curved (Erslev, 1991). When comparing fault-bend and fault-propagation folds, there are geometrical similarities. In many cases what started up as a double-edge fault-propagation fold (isolated fault segment), developed into a fault-bend fold at a later stage when the thrust propagated into higher flat (Tavani and Storti, 2006).

When the strata above a detachment zone or a bedding-parallel thrust buckles and create a fold, it is called a detachment fold. The defining feature is that displacement beneath the fold diminishes gradually, in most cases towards the foreland. For this type of folding, the fault needs to follow a layer of weak and ductile rocks (e.g. evaporites or shales). The weak rock will flow into the base of the fold, filling up the space created by up-folding (Jamison 1987, McClay 1992, Mitra 2003). The thickness of the main weak units controls the wavelength of these folds (Mitra, 2003). A detachment fold is different from a fault-bend fold and a fault-propagation fold in that it is normally more symmetric and upright, especially at an early stage (Mitra, 2003).

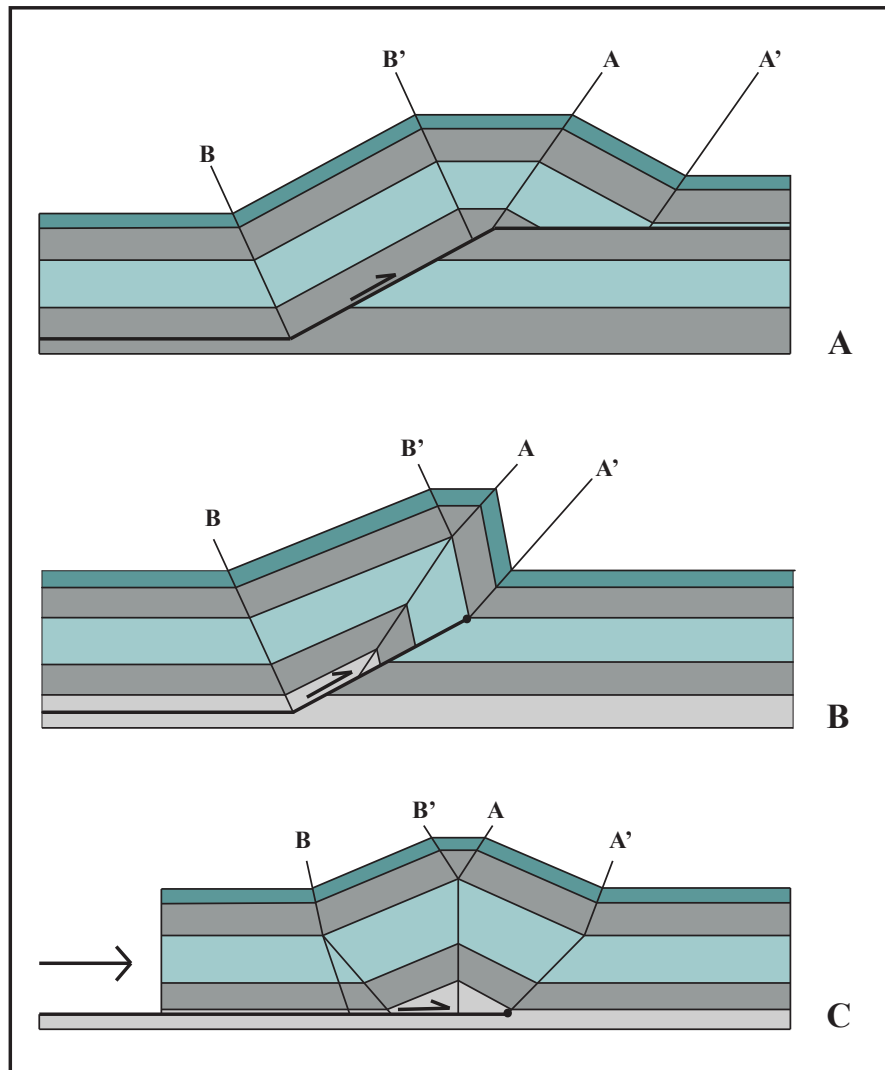


Figure 3. 3: The three main types of thrust related kink-style folds. **A)** Fault-bend fold **B)** Fault-propagation fold and **C)** Detachment fold (modified from McClay, 1992).

3.3 Fracture development

3.3.1 Basic fracture types

Fractures are discrete deformation structures, caused by rock failure through loss of cohesion. They can either be termed joint, shear fracture or if filled, a vein or a dike. Fractures can be found in all sizes but are not infinite in length. They are defined as discontinuities in a rock (e.g. Schultz and Fossen 2008). The principal stress causing a rock to fracture ($\sigma_1 > \sigma_2 > \sigma_3$) has maximum stress termed σ_1 , while the minimum stress is termed σ_3 . The effective stress (σ') is: $\sigma' = \sigma$ (total stress) - p (fluid pressure) (Mogi 1967, Hancock 1985). From analysis of tensile type of fracturing, Irwin (1957) came up with three main modes (mode I-III) for how an individual fracture grows

(Figure 3.4). Mode I is extensional fracture that has displacement perpendicular to the axis of least tectonic stress (σ_3). These fractures might be through-going, confined to only one bed by arrest at bed interfaces, or tip out in the bed. They are able to grow without change in orientation.

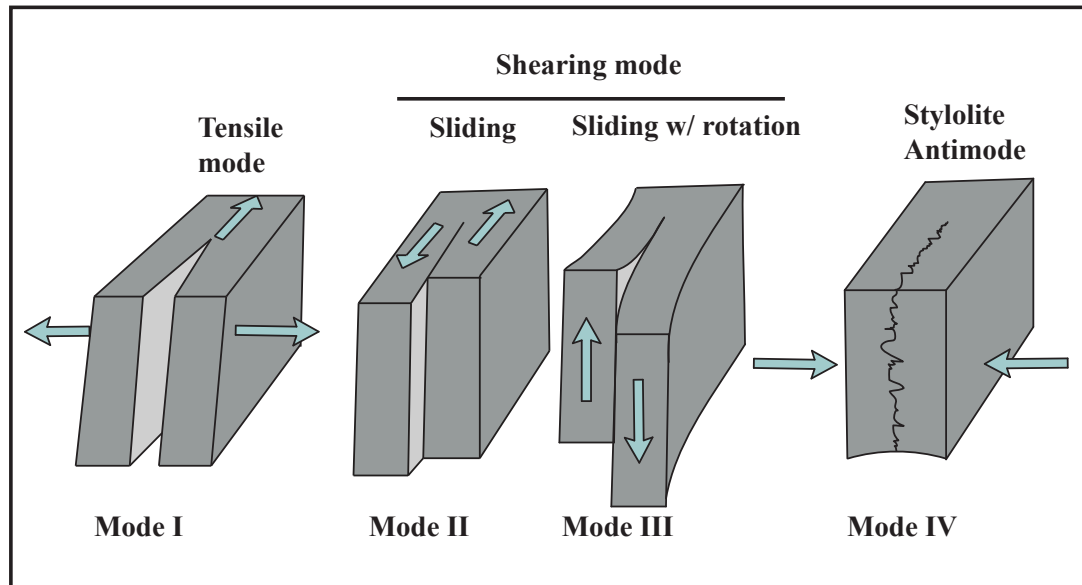


Figure 3. 4: The figure displays the main fracture types, grouped as mode I-IV. Mode I represents joints, while mode II-III are shear fractures. Mode IV develops during compression, resulting in volume loss due to pressure dissolution of grains (modified from Van der Pluijm and Marshak, 2004).

Mode II and mode III are both shear fractures, but while mode II fractures develop with shearing parallel to the fracture walls, mode III also includes rotation. Shear fractures commonly develop at 20-30° to σ_1 , and in conjugated pairs symmetric to the principal stress axes. Both extensional and shear fractures typically develop near the earth's surface and in upper parts of the crust, but shear fractures are also able to form close to the brittle-plastic transition. Hybrid fractures are present when there has been a combination of tension (mode I) and shearing (mode II and mode III). A fourth mode relates to compression; stylolites form by compression in an opposite sense to fractures of mode I. However, according to Delvaux and Sperner (2003) are stylolites not seen as compression fractures, but indicators of compressive stress.

3.3.2 Diagenetic fractures

Fractures originate based on variable factors. Engelder and Lacazette (1990) discuss how pore pressure triggers formation of fractures. This process is called hydraulic fracturing, and happens when the pore pressure exceed the compressive rock strength.

The net stress will then be tensile and cause fracturing. However, when the fracture develops, the pore pressure will drop and stop further fracturing. The classical model for pore pressure jointing was presented by Secor (1965,1969), who outlines stages of the jointing; 1) initiation, 2) propagation and 3) arrest. Further, he mentions the importance of open fractures when considering fluid flow such as hydrocarbons and ground water.

Silica fracturing arises when there is a conversion from opal A (non-crystalline biogenic silica) to opal CT (microcrystalline silica). In a clastic sedimentary basin, this thermochemical process occurs in buried sediments at the temperature interval of 2°-55°C (Hein et al. 1978, Bohrmann et al. 1994, Davies 2005). The reaction first dissolves silica and then re-precipitates in a phase change. This leads to volume reduction, as opal CT is denser than opal A. Furthermore the reaction results in a higher rate of compaction and reduced porosity, which again could cause related deformation at a km-scale, linking subsidence and fracturing (Davies, 2005). Taking this chemical reaction one step further, the opal CT turns into chalcedony or crystalline quartz (chert) (Kastner et al. 1977).

Dolomitization can be a reason for fracturing, and occurs when calcium carbonate (CaCO_3) turns into dolomite ($\text{CaMg}(\text{CO}_3)_2$) by adding Mg. This change relates to diagenesis, mostly at large depths (minimum 800-1000 m) (Dravis 1980, Grabowski 1984, Lind 1993, Wierzbicki et al. 2006). The process of dolomitization creates a volume reduction of 13 %, which can both decrease and increase the porosity depending on the crystal framework (Weyl, 1960). Since dolomite is more brittle by nature than calcium carbonate, it will also fracture more easily (Wierzbicki et al. 2006).

3.3.3 Tectonic fractures

Fractures are not just discontinuities of a rock, but holds information about earlier stress regimes. For instance, joints may form stress systems in an orogeny (Engelder and Geiser 1980). Shear fractures can leave steps and slickenlines along the fracture plane, which are good indicators of the transport orientation (slickensides). When the same stress field forms two fractures that intersect each other, they form a conjugate set. They are typically separated by an angle of ~30°- 60° (Stearns 1968, Hancock 1985, Doblus 1998, Bergbauer and Pollard 2004). Ramsey and Chester (2004) argue that there is a third end member type of fracture, hybrids. Hybrids include both

opening and shear modes, and can be seen as a transition from compression to extension (Figure 3.5). The fractures form at an angle that is greater than angles of extensional fractures, and less than that of shear fractures. This means that they will have an acute angle to the maximum principal stress.

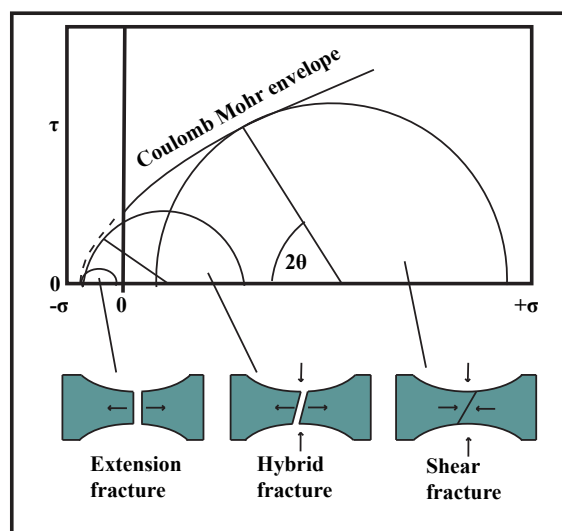


Figure 3. 5: The Mohr diagram here is used to display the different modes of brittle failure (extension, hybrid and shear). For a given non-fractured rock where the Mohr circle intersects the failure envelope, fractures form. The model show how hybrid fractures is a transition phase from compression to extension. The plot display shear stress, τ , versus normal stress, σ . θ is the predicted fracture angle, that is the measured angle between the fracture surface and the direction of σ_1 (modified from Ramsey and Chester, 2004).

3.3.4 Fracture intensity

When analyzing fractures, an important dataset is the fracture intensity. The spacing between fractures is what determine the fracture intensity, and can be studied in 1D (line measure), 2D (area) or 3D (rock mass) (Dershowitz and Herda 1992, Ogata et al. 1014). This study has used the line intersection method, collecting data by scanlines, which is the most common used method. Information about rock properties, bed thickness and structural position are all important parameters influencing fracture intensity (Hancock 1985, Huang and Angelier 1989, Cooke et al. 2006, Ogata et al. 2014). The rock properties include composition, grain size, porosity and presence of fossils (Cooke et al. 2006). A fracture might nucleate more easily around a fossil, because the tensile stress in the rock is more concentrated here (Gross, 1993). Coarse-grained beds have a lower tensile strength than fine-grained beds and, therefore higher possibilities for fracturing (Friedman et al. 1994, Renshaw et al. 2003). Overall, thin beds are seen to have smaller spacing between the fractures than

thick beds, and accordingly a higher possibility of fracturing than thick beds (Huang and Angelier, 1989).

3.4 Fold related fractures

Fractures in fold-thrust belts are discussed in Price (1967), Stearns (1968), Groshong (1975) and Hancock (1985). When looking at folded sedimentary strata, Stearns (1968) suggested a model of 11 fracture orientations (Figure 3.6). These common orientations are divided into 5 different populations, where the populations include two conjugate shear fractures and one extension fracture sets. The populations are divided by a *neutral surface* that marks the zero-strain surface. Above the neutral surface the rock experience extension, containing population 2 and 3, while set 1 and 4 are placed below, representing contractional fractures. The fifth fracture population represents the shear fractures that form during folding, as a result of slip between beds (this population are not included in Figure 3.6).

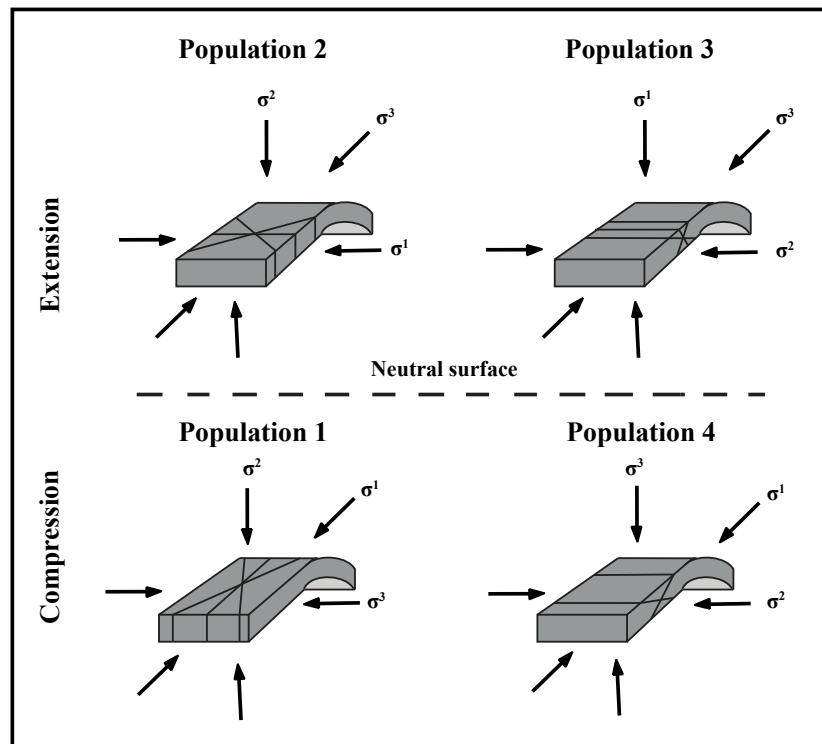


Figure 3. 6: Typical fractures in folded sedimentary strata, where the 11 fracture orientation sets are grouped into five different populations, with population one to four displayed in the figure. The fractures form symmetrical to the axis of the fold. The neutral surface of zero-strain, separate the contractional fractures from the extensional fractures (modified from Bergbauer and Pollard, 2004).

Hancock (1985) developed another model for fractures in folds, based in the notation of Turner and Weiss (1963) (Figure 3.7). The three axes that are distinguished for a fold are not dependent on absolute orientation. The axes, based on an orthogonal reference system symmetrical around bedding, is given the names a, b and c. The defined planes are thus named ab, ac or bc. Further the letters h, k and l are the fracture surfaces that intercept the fold axis. This means that h intercepts a, k intercepts b and l intercepts c, while 0 means a fracture surface is parallel to one of the fold axis. Fracture surfaces oblique to all three fold reference axes, will then be termed hkl (Price 1967, Hancock 1985). Studies show that a multilayered fold might experience shearing, dilatation or shortening at the ab surface as the stress is active on the fold (Hancock, 1985). Flexural slip is an example of a process at the ab surface (Shaw et al. 2005). Conjugated fracture systems are common, and the mesofracture sets leads to shortening or stretching of the fold. The fractures that do not fit into the model are, according to Hancock (1985), made prior to or after the folding, or are accommodation fractures caused by non-systematic strain.

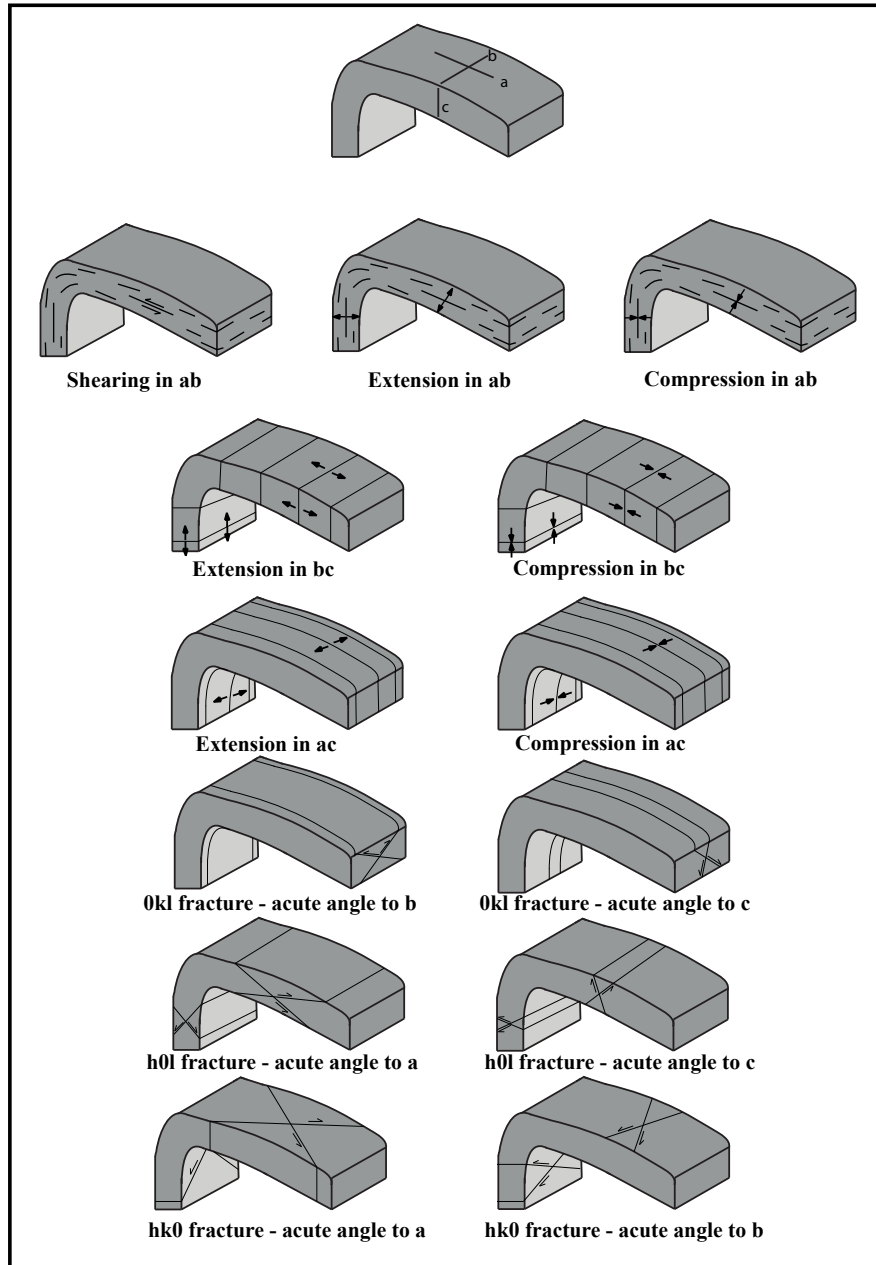


Figure 3. 7: Mesofractures in a fold can be grouped into different sets and populations. The fold is built up of sedimentary strata, where ab defines the bedding surface. The fractures record bulk strain during deformation (modified from Hancock, 1985) in what can be termed cataclastic or frictional flow during folding.

3.4.1 Cataclastic flow related to folding

Folding is a result of ductile style deformation, normally at some depths in the crust. Depending on the mineral composition and mineral response to stress, folding could occur by plastic deformation mechanisms (grain-scale flow). The exception is cataclastic flow (eg. Ismat and Mitra, 2001), or frictional flow, which involves frictional sliding, dilatancy and fracturing of the grains and beds (Sibson 1977,

Paterson 1978). This mechanism makes it possible to have a ductile deformation style above the brittle-plastic transition zone in the crust (eg. Ismat and Mitra, 2001). According to Sibson (1977), the term “cataclastic flow” is applicable to all scales, and occurs in the Elastico-Frictional regime (EF) at shallow depths (shallower than ~10 km for quartz, using a geothermal gradient of ~25°C/km). Accordingly, folds in the upper crust, such as in a fold-thrust belt, relate to cataclastic flow unless hydroplastic (unconsolidated sediment) or plastic (very low shear strength such as salt) flow contributes to deformation.

Folds commonly show inhomogeneous deformation with different fracture populations in the folds hinge and limbs as outlined above (Price 1967, Hancock 1985). Further strain tends to be most intense in the fold hinge. With fold hinge migration the fracture sets formed in the hinge zone will overprint the fractures in the former fold limb. Dynamic folding with overprinting fracture sets and strain zonation creates blocks bounded by fractures of different size. If there is movement along the fractures, the moving blocks will collide and further fracture, and the smaller blocks will sustain the continuity between the larger blocks. Accordingly, movement and fracturing of the blocks cause multiple block-sizes that allow frictional flow. This deformation mechanism can be observed as ductile, which at large-scale comprises cataclastic flow (Ismat and Mitra 2001). Strain compatibility is however essential, and needs to be present (Paterson 1978, Menendez et al. 1996). The compatibility can be sustained by having different deformation mechanics active simultaneously at different scales. While there is cataclastic flow on a large-scale, it could for instance be pressure solution and diffusion in addition to fracturing at a smaller scale (Ismat and Mitra, 2001). As discussed here, cataclastic flow can occur at any scale, but are depending on a network of intersecting fracture systems and deformation zones (Ismat and Mitra, 2001). In this thesis, frictional flow and complementary deformation mechanisms on a small scale comprise cataclastic flow during folding.

3.5 Fluid flow on fractures

Fractures can be either open/unaltered, healed or sealed as discussed in for instance Ogata et al. (2014). Fluid flow is strongly dependent on the fracture intensity in tight rocks, which is a common character of carbonates. Long, large fractures are common

in thick beds and if open provide clear pathways for fluid flow. Short fractures located in thinner beds have less potential for fluid flow, even though the fracture intensity is overall higher; this is because these short fractures are normally not located in the same plane and therefore produce tortuous flow paths. Further, long fractures intersect more fractures than short ones (Tsang 1984, Odling et al. 1999, Cooke et al. 2006).

Open fractures are, as earlier described, relevant for fluid flow. With fluid flow minerals can precipitate, in cases sufficient to seal the fracture. The sealed fracture will then act as a barrier instead of a pathway. However, Ogata et al. (2014) discuss that the fractures that are sealed by elastic strain (by vertical stress) can relatively easily be reopened when subjected to small pressure increments.

A study of fractures also addresses the potential for fluid flow; herein the aim is to distinguish a fractured rock's properties as a reservoir. Nelson (2001) proposed a classification system of fractured reservoir types, which is based on the matrix character and fracture network. Four types of fractured reservoirs are classified; in Type-I reservoirs the porosity and permeability is provided by fractures, Type-II reservoir has the essential permeability by fractures, with a small contribution from matrix. If the reservoir is already producible, but with a low permeability, and fractures assist to give a better permeability it is a Type-III reservoir. The last type of reservoir, Type IV, is when the matrix contribute to both storage and flow, but the fractures enhance the already high permeability (Figure 3.7) (Nelson 2001, Mäkel 2007, Awdal 2009).

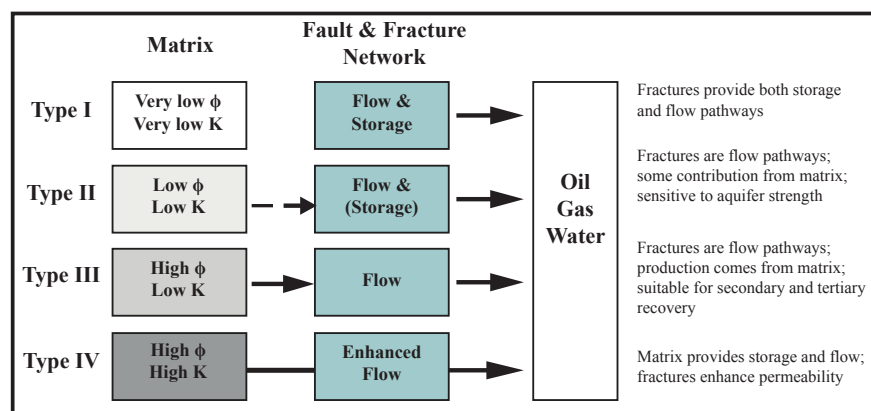


Figure 3. 8: Classification system for fractured reservoir types based on the contributing effects matrix and fracture network have to porosity and permeability. ϕ is porosity, while K is permeability (modified from Makel (2007), after Nelson (2001)).

CHAPTER 4 LITHOLOGY DESCRIPTION

4.1 Introduction

This chapter focuses on the lithology of Mediumfjellet, and gives a detailed description of the stratigraphy in the study area. The main stratigraphic units present in the Mediumfjellet are the Upper Carboniferous to Permian Gipsdalen Group, the Upper Permian Tempelfjorden group, the Triassic Sassendalen group and Lower Cretaceous intrusions. See Figure 4.1 for a lithostratigraphic scheme of the studied formations in Svalbard.

The nomenclature of the Upper Paleozoic stratigraphy, as defined by Dallmann et al. (1999), is used in this study. A detailed description of the studied rock is important, having a possible influence on the different fracture systems.

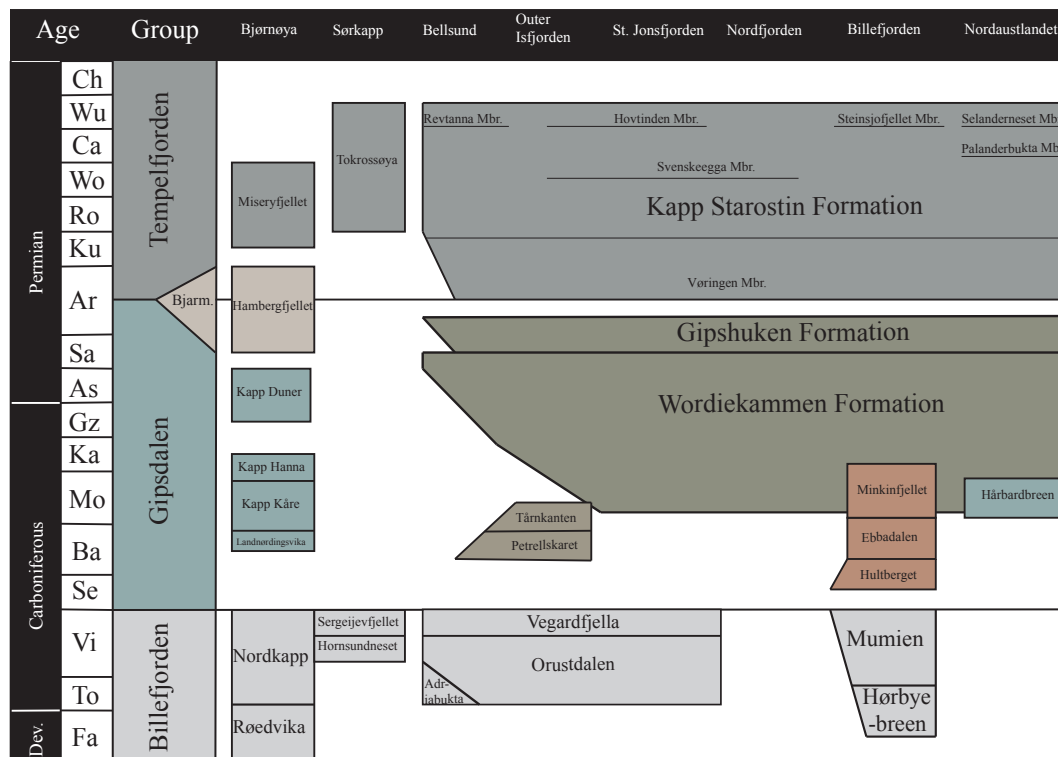


Figure 4. 1: A lithostratigraphic scheme for the Upper Paleozoic of Svalbard. Note that the names within the Kapp Starostin are all members, while the other names listed is all formations. The geological timescale are after Gradstein et al. (2004). Modified from Dallmann et al. (1999).

The lowermost part of the logged section is the upper part of the Gipshuken Formation, which is mostly represented here by carbonates. The rest of the logged section belongs to the mixed carbonate and spiculitic Kapp Starostin Formation of the Tempelfjorden Group. This formation is the main focus for this study as it covers most of the field area. See Figure 4.2 for the log track.



Figure 4. 2: A photo taken from top of the logged mountain ridge, looking south. The white line marks the measured profile. Note yellow tents on the beach for scale.

4.2 Gipsdalen Group

The Gipsdalen Group was deposited from Middle Carboniferous to Early Permian (Serpukhovian – Artinskian), with the name first being used by Cutbill and Challinor (1965). The stratigraphic succession shows the development from a mixture of syn-rift siliciclastic carbonates and evaporites in Carboniferous to marine shelf carbonates and evaporites in Late Carboniferous and early Permian. Overlying this unit is the Tempelfjorden Group, with the Billefjorden Group underlying it in most places. In several graben-structures basin fill has resulted in subgroups like Treskelen, Charlesbreen and Cambellryggen. These subgroups are overlain by a subgroup called

the Dickson Land Subgroup, which includes the Wordiekammen Formation and the Gipshuken Formation (Dallmann et al. 1999). At Mediumfjellet the only formation that can be seen from the Gipsdalen Group is the Gipshuken Formation, the lowermost part of the logged section (Figure 4.3).

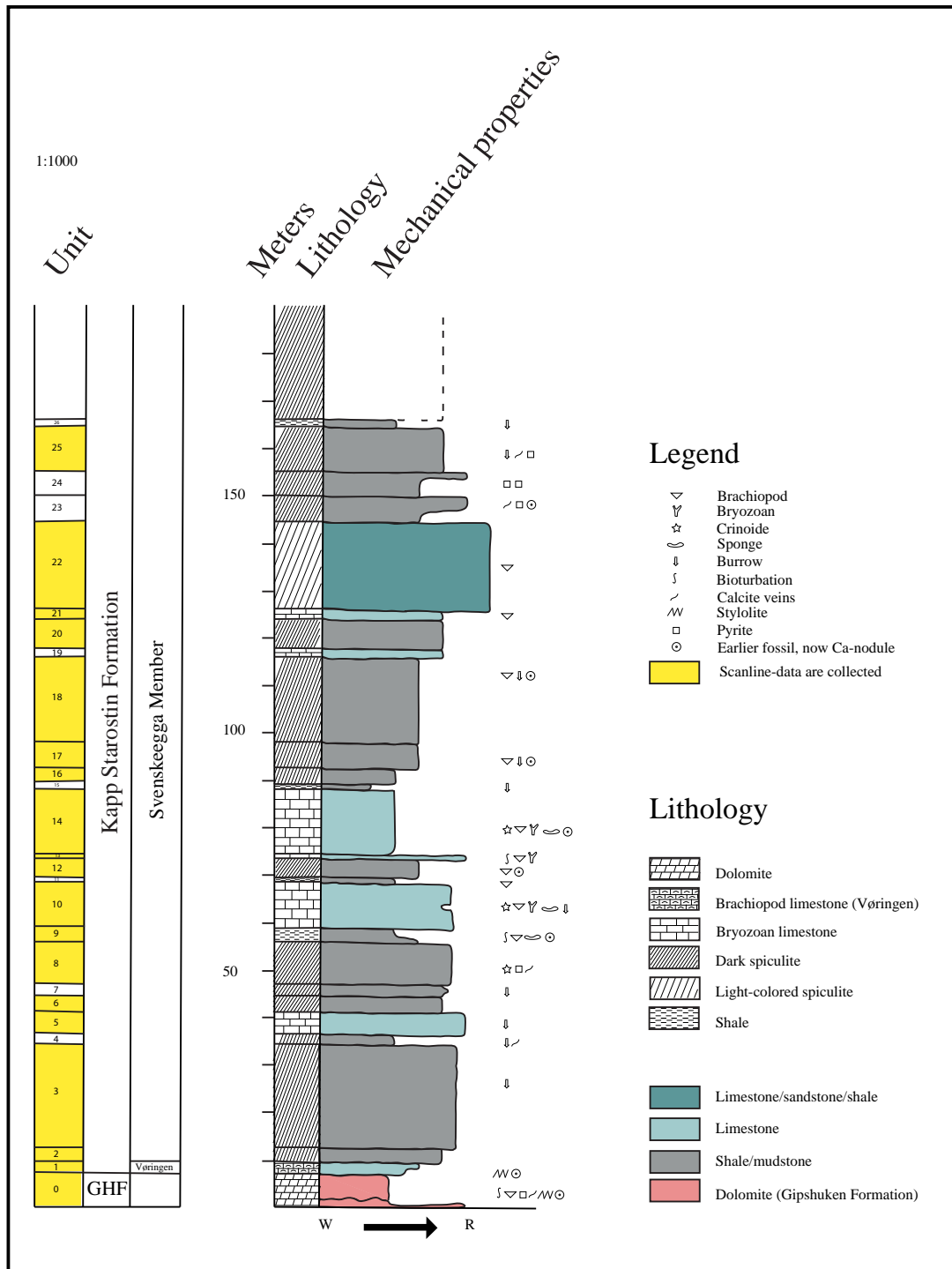


Figure 4. 3: Stratigraphic log presenting Gipshuken Formation (GHF) and Kapp Starostin Formation. The unit section shows where fracture data has been collected (yellow). Note that it is the mechanical properties of the rock that is shown, and not its grain size. W: weak, R: rigid.

4.2.1 Gipshuken Formation

Nathorst (1910) first described the Gipshuken Formation as “Gypsum beds”, before Cutbill and Challinor (1965) came up with its present name. The type section has a thickness of 245 m and is located at Bredsdorffberget in Dickson Land, made up of dolomite, limestone, anhydrite/gypsum and carbonate breccia from Early Permian. However, only a few meters of Gipshuken Formation are observed in outcrops at Mediumfjellet. The Formation is subdivided into six members, the Vengeberget, Zeipelodden, Kloten, Skansdalen, Templet and Sørfonna member. Since the formation is poorly exposed at Mediumfjellet, it is difficult to determine which member is present. The Gipshuken Formation at Mediumfjellet is probably associated with major thrust faults (Dallmann et al. 1999).

Lithology description

At Mediumfjellet, the Gipshuken Formation is logged to be ~7 m. The outcrop is grey in color, with patches of yellow weathering (Figure 4.5A). The base of the overlying Vøringen Member erodes into the Gipshuken Formation, resulting in a sharp upper boundary. This erosive surface also defines the top of Gipshuken Formation (Figure 4.5D). At Mediumfjellet the 7 m is observed to be a mix of mudstone/floatstone with brachiopods, brachiopod fragments, algae lamination, bioturbation, root traces and stylolites. Rip-up clasts of algae lamination have been observed, as well as planar parallel lamination partly destroyed by bioturbation.

A small outcrop at the beach (not included in the log) has been suggested to be a part of the Gipshuken Formation. This section is 4 m. The outcrop is made up of alternating beds of white gypsum and greyish dolomite. The gypsum is highly weathered with rillenkarren (small channels, ca. 1 cm in width) at the outcrop base. The gypsum is soft, while the dolomites are more rigid, but they are both highly folded. At the top of the outcrop is white, highly weathered gypsum.

This is similar to what is observed by Dallmann et al. (1999) in the Skansdalen Member. The carbonates in the logged section are thus likely to be dolomites. This can be verified by thin section studies (see Chapter 5.6).

4.3 Tempelfjorden Group

In Svalbard, the Tempelfjorden Group is about 460 meter thick and overlies the Gipsdalen Group. The depositional age is thought to be Middle – to Late Permian. The name Tempelfjorden Group, was first used by Cutbill and Challinor (1965). The lower boundary marks the transition to cooler water conditions, going from warm water carbonates in Gipshuken Formation (Moscovian - early Sakmarian) to cool water carbonates in Kapp Starostin Formation (late Sakmarian – Artinskian) (Ehrenberg et al. 2001, Blomeier et al. 2011). The fossils found in these two groups are also very different. The Tempelfjorden Group consists of siliceous (spiculitic) shales, siltstones and cherts with sandy layers, and show deep-water facies that may suggest sea level rise. According to Dallmann et al. (1999) is there three formations included in this group, called the Kapp Starostin Formation (Spitsbergen and eastern islands), Tokrossøya Formation (Sørkapp area) and Miseryfjellet Formation (Bjørnøya). However, the Tokrossøya and the Miseryfjellet Formation are only usable for the Sørkapp area and Bjørnøya (Dallmann et al. 1999). The field studies have exposed rock from the Kapp Starostin Formation. This is the formation that is seen as an analogue to the L-9 unit on the Finnmark Platform in the Barents Sea (Ehrenberg et al. 2001).

4.3.1 Kapp Starostin Formation

During deposition of this formation the carbonates went from being cool water to cold water carbonates (Kungurian – Late Permian). The type section is taken from Kapp Starostin in outer Isfjorden and is measured to be up to 460 m thick in St. Jonsfjorden Trough. In Isfjorden it is 380 m thick, but thins towards south and pinches out east of Sørkapp-Hornsund High (Dallmann et al. 1999). The logged section at Mediumfjellet is no more than ~160 m thick, and only parts of the formation can be studied here. The main lithologies in the Kapp Starostin Formation are spiculitic chert, siliceous shales and sandstones, and carbonates. Typical fossils found in this formation are brachiopods, bryozoans, sponges, echinoderms (crinoids) and the trace fossil *zoophycos*.

The Kapp Starostin Formation is subdivided differently depending on the location on Svalbard (Figure 4.1). In the Nordfjorden and Isfjorden area it is subdivided into three members, named the Vøringen Member, Svenskeegga Member and Hovtinden Member (the latter two are only defined at the type section in outer Isfjorden). The

Vøringen member's sharp and erosive contact clearly marks the base of the formation with its bioclastic brachiopod-rich limestone overlying the dolomitic lithologies in the Gipshuken Formation. The Svenskeegga Member is made up of mainly spiculites, with some chert beds and siliceous limestone beds. The Hovtinden Member is defined as silicified shales, siltstones, sandstones and limestones. Its lower boundary is set where shales, sandy cherts or cherty sandstone overlie the bioclastic limestone of the uppermost part of the Svenskeegga Member. The boundary is conformable, and is only defined at the type area at outer Isfjorden (Dallmann et al. 1999).

The lithology description below is taken from the unit description in Appendix 1, referring to Figure 4.3. There are five different lithologies defined in the logged section of Kapp Starostin, a classification similar to the facies associations in Ehrenberg et al. (2001). A more detailed look at the different lithologies and their accompanying units follows.

Lithology description

Brachiopod limestone

Observations from the field show that the U1 (~2 m thick unit) is a medium grey limestone, abundant in macrofossils as brachiopod shells and sponges. It is mostly a rudstone, but in some places is interpreted as a floatstone (Figure 4.3; Figure 4.5B). The lithology is comparable (its high content of brachiopods) to the brachiopod limestone described in Ehrenberg et al. (2001).

Bryozoan limestone

The bryozoan limestone beds are mainly found in the lower part of the Kapp Starostin Formation (Unit 5, 10, 13, 14, 19 and 21; Figure 4.3). They are mostly grey with patches of yellow weathering, bioturbated, and contains sponges, crinoids, brachiopods and bryozoans (Figure 4.5F, G and H). When looking at the grain size and classification of the bryozoan limestone, it is spanning from mudstone to rudstone, with matrix of silicified carbonate or shale. Even though bryozoans are not observed in all carbonate beds, they are all termed bryozoan limestone. This is because an abundant bryozoan fossil in the Kapp Starostin Formation is the *fennestrate bryozoan*, observed as circular voids of up to 1 mm in diameter, and can easily be overlooked.

Dark spiculite

Dark spiculitic beds are abundant in the Kapp Starostin Formation (Unit 2, 3, 4, 6, 7, 8, 12, 16, 17, 18, 20, 23, 24 and 25; Figure 4.3). They range from a grey to dark grey color, with highly silicified beds and intercalating laminated mud. The beds are often highly fractured that gives a nodular characteristic bedding (Figure 4.4). Some beds do also contain black nodules, which are not linked to fracturing. Earlier work has suggested that the nodule shape is a result of diagenetic silica growth occurring around *Thalassinoides* burrows (e.g. Fredriksen 1988, Henriksen 1988). Bioturbation is common and *zoophycos* and *lamellae ichnus* are observed (Figure 4.5H), while brachiopods are present but not abundant. Lithology similar to these spiculitic beds, have been found offshore on the Finnmark platform, but these spiculites are more calcareous (Ehrenberg et al. 2001).



Figure 4. 4: Dark spiculite from U3 with its nodular characteristic bedding. Note the coin for scale.

Light-colored spiculite

The light-colored spiculite is observed towards the top of the logged section (Unit 22; Figure 4.3). It has its characteristic light grey to white color, and is composed mostly of chert (Figure 4.5E). The carbonate content varies related to the amount of fossils present. The middle part of the unit consists of thicker and more massive beds than the ones below and above, with intercalations of shale (up to 5 cm thick). There is abundance of brachiopods throughout the whole unit. Examples of similar lithology can be found on the Finnmark platform (Ehrenberg et al. 2001) and at other locations in Spitsbergen (Grundvåg 2008).

Shale

The shaly units present in The Kapp Starostin Formation are maximum ~3 m in thickness (Unit 9, 11, 15 and 26; Figure 4.3), and composed of fine-grained mudstone. They have a greyish color, with common brachiopods, sponges and fossil fragments. Some beds are more weathered than others, making diffuse bedding, having mostly slope scree (Figure 4.5C). Burrows are also present. The same lithology can be seen as thin lamina dividing the beds of other lithologies in the Kapp Starostin Formation.

4.4 Intrusions

Lower Cretaceous intrusions (e.g. Gayer et al. 1966, Smith et al. 1976, Nejbort et al. 2011, Corfu et al. 2013) are present in the Mediumfjellet Mountain range as diabase sills and dikes. These intrusions are important because they affect the stratigraphy of individual horizons and thus later deformation. The diabase sills generally follow weak layers such as the gypsum in the Gipshuken Formation and the shale in the Triassic Botnheia Formation. The Kapp Starostin Formation host most of the dikes, cutting up through the stiffer strata (Larsen 2009). At the studied locality of the Kapp Starostin Formation, there are no intrusions, and therefore no intrusions will be described further.

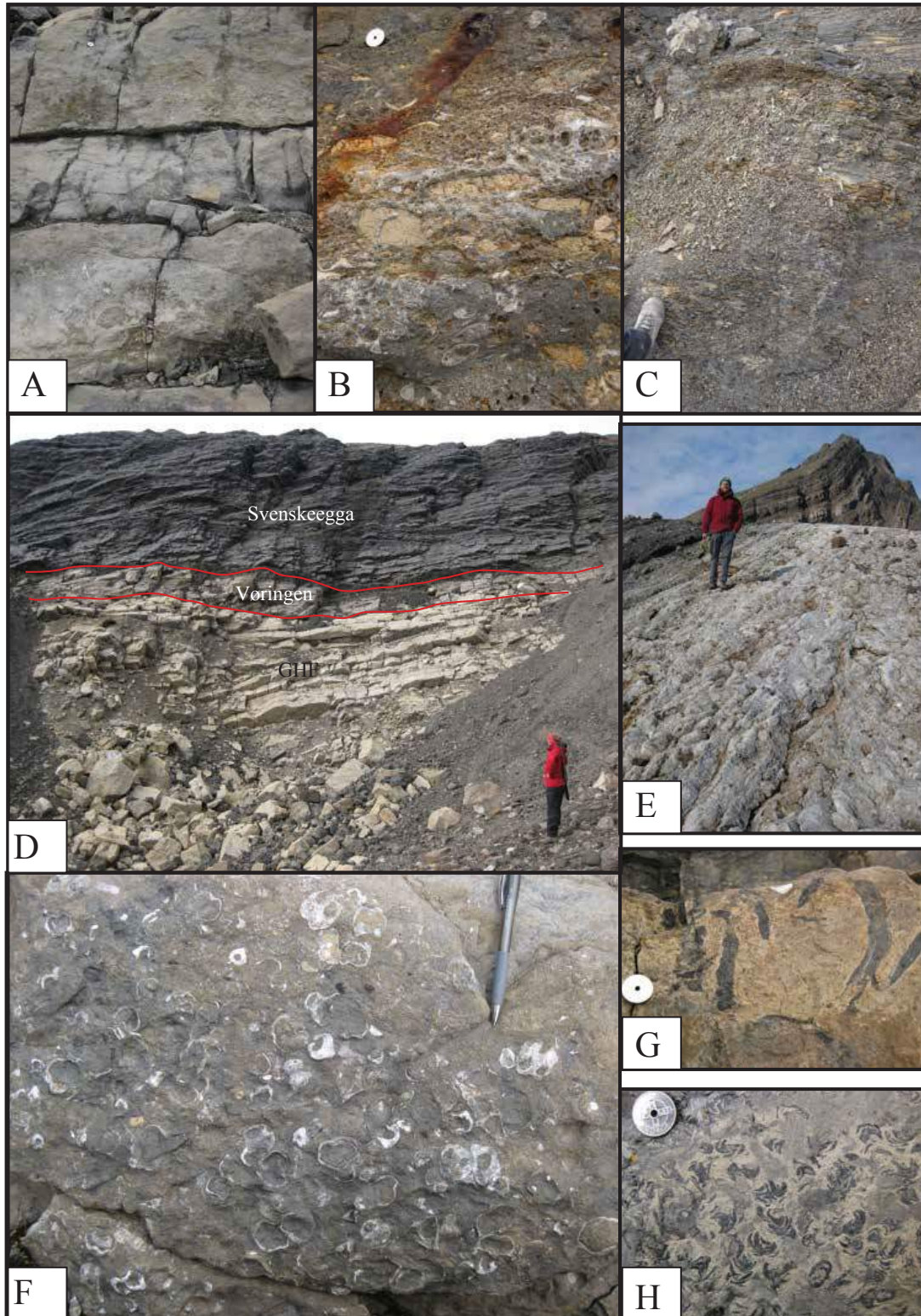


Figure 4. 5: Photos taken in field from the logged section at Mediumfjellet. **A)** Carbonates from the top of Gipshuken Formation, U0. **B)** Carbonate rock from the Vøringen Member, U1. **C)** Permian highly weathered shale, Kapp Starostin Formation. **D)** Overview photo of the lower part of the ridge. At the base is light yellow to greyish rocks where Vøringen Member is overlying carbonates from the Gipshuken Formation (GHF). On top is the dark grey to black spiculitic beds, U3. **E)** The light-colored spiculitic unit, U22. **F)** A carbonate bed full of brachiopods in the Kapp Starostin Formation, U10. **G)** Characteristic burrows in a carbonate bed, U10. **H)** Characteristic burrows found through the whole Kapp Starostin Formation, called *Lammellae ichnus*.

4.5 The stratigraphic importance of deformation

Lithology is an important factor when looking at how stress acts on a body of rock. This includes macro scale structures. A detachment zone likes to follow weak layers, such as evaporites or weak shales (Mitra 2003, Shaw et al. 2005). This is seen at the Mediumfjellet Mountain, where the major thrust follows the gypsum and anhydrites in the Gipshuken Formation, as well as the Triassic shale. The Mediumfjellet-Lappedalen thrust front is seen to be where the detachment zone meets an obstacle in the weak evaporites and climbs up section. The next detachment zone goes through the younger Triassic shales, and creates a flat-ramp-flat geometry, where the ramp cuts through the Kapp Starostin Formation (see Chapter 2; Figure 2.3).

4.6 Summary and interpretation

The observed lithology of the Gipshuken Formation is interpreted to be dolomite, while the different lithologies found in the Kapp Starostin Formation at Mediumfjellet are suggested to be:

- 1) Brachiopod limestone
- 2) Bryozoan limestone
- 3) Dark spiculite
- 4) Light-colored spiculite
- 5) Shale

The brachiopod limestone observed towards the base of the logged section is interpreted to be the Vøringen Member, and makes up the lowermost part of the Kapp Starostin Formation. The Vøringen Member is a marker bed for the boundary between the more easily weathered dolomite in the Gipshuken Formation and the cliff forming limestone and chert spiculites in the Kapp Starostin Formation (Dallmann et al. 1999). It is a bioclastic limestone, and has a thickness of up to 40 m in Svalbard (22 m in stratotype in outer Isfjorden) (Dallmann et al. 1999). At Mediumfjellet the limestone is very thin and observed to be only ~2 m thick. The limestone is described by earlier authors to be rich in brachiopods, bryozoans, crinoids and other marine fossils

(Dallmann et al. 1999, Grundvåg 2008), which fits with the observations done in field.

The lithology above the Vøringen Member is mainly comprised of spiculites, and some beds of carbonates and shale. The fieldwork has resulted in similar observations as mentioned in the type section in outer Isfjorden, but the boundary between Svenskeegga and Hovtinden Member is difficult to distinguish. The Svenskeegga Member consists of cherts and spiculitic shales, but also siliceous limestones where fossils like sponges, spicules, brachiopods, bryozoans and trace fossils (e.g. *Zoophycos*) are present, according to Dallmann et al. (1999). Based on the descriptions of Svenskeegga and Hovtinden Member in Dallmann et al. (1999), it is suggested that the whole section above Vøringen is equivalent to Svenskeegga Member. This however, is in contrast to what was suggested in Larsen (2009), where the Svenskeegga-Hovtinden boundary is placed 100 m lower in the stratigraphy (equivalent to U14/U15 boundary in the log in Figure 4.3). This interpretation gives a ~160 m thick succession of Svenskeegga Member at Mediumfjellet, which is similar to the type section of 165 m.

According to Ehrenberg et al. (2001) is the dolomite in Gipshuken Formation shallow marine deposits in an intertidal flat environment. The boundary between Gipshuken and Kapp Starostin marks a major disconformity. The Vøringen Member, who overlies the Gipshuken Formation, has been interpreted by Ehrenberg et al. (2001) to be an overall transgressive unit in an open shelf environment. However there are also internal karst surfaces present, indicating a fluctuating relative sea level. The overlying Svenskeegga Member is interpreted to be a shift to a cooler water environment and deeper marine shelf conditions, where the spiculites are deposited during a highstand (Ehrenberg et al. 2001, Blomeier 2011).

As discussed in Chapter 4.5, the lithology is very important when looking at deformation, influencing both macro and micro scale structures. The large-scale thrusts follow the weak layers of evaporites in Gipshuken Formation and weak shales in Triassic rock. The smaller fractures are also dependent on lithology and its rock mechanism. This results in some beds being more highly fractured than others. The fracture data will be looked further into in the next chapter; *Chapter 5 Results* and discussed in *Chapter 6 Discussion*.

CHAPTER 5 RESULTS AND STRUCTURAL DESCRIPTIONS

5.1 Introduction

The aim of this chapter is to present and analyze data collected during fieldwork. Interpretation of Lidarscan photos in Lime is an important part of the study, as well as microtextural analysis on rock samples.

The chapter starts with analyzing the macrostructures present in Mediumfjellet, then suggesting an estimation of the layer parallel shortening (LPS) in the area. The estimated LPS are based on measurements done in Lidarscan. Thereafter, the fractures from the field area will be discussed by looking at fracture characterization and orientation trends. They are analyzed in statistical plots, focusing on fracture frequency variations. The last part will present information obtained at micro-scale, by studying the lithology in thin-sections from the area.

5.2 Structural framework of the area

The study area is Mediumfjellet, located between Sveabreen and Wahlenbergbreen (Figure 5.1), with focus on the southwestern ridge partly in front of the Wahlenbergbreen. By comparing Lidarscan data of the mountain with field observations, it has been possible to make four cross-sections and interpret the tectonic macro structures in the area.

The Mediumfjellet thrust stack, which marks the thrust front towards east, is recognized to have 4 main thrusts:

- M1
- M2
- M3
- G

These thrusts have had a large tectonic impact on the area, which can be seen as folded and thrust rocks today. Each fold and thrust province will be discussed, and results based on field observations, Lidarscan, and descriptions from Bergh and Andresen (1990), Bergh et al. (2003) and Larsen (2009) is presented. The location of the four

cross sections has all been visited in field. Note the field observations have had the strongest influence on the final result. The dip of the thrusts and layering has been measured on photos.

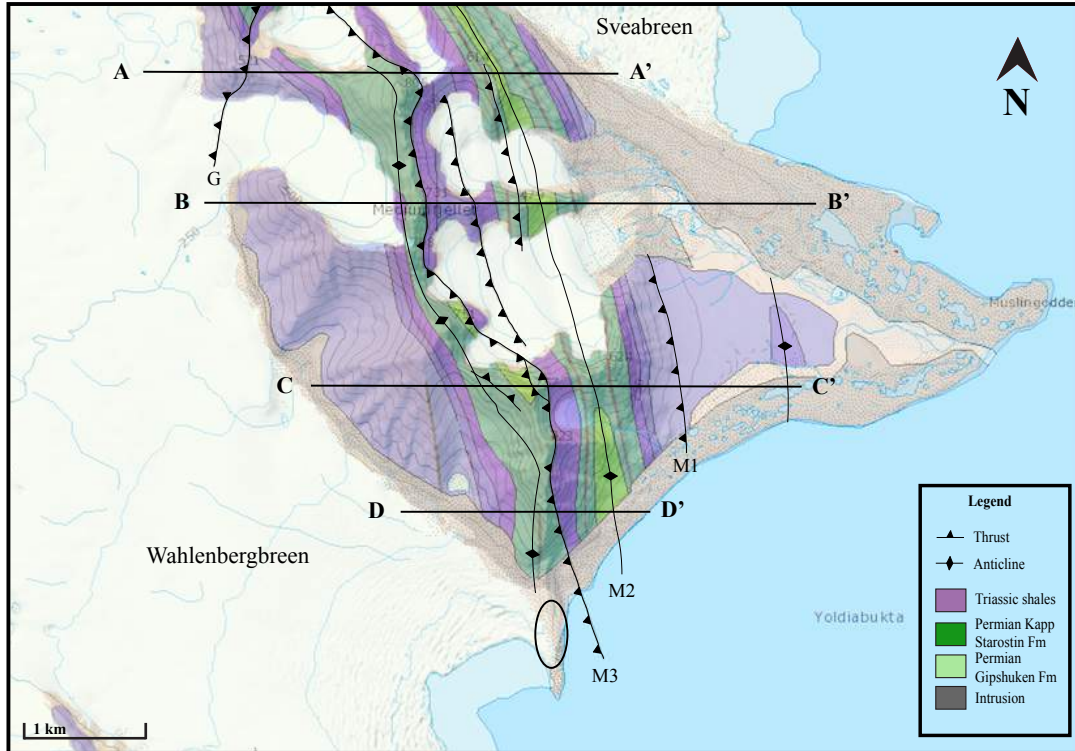


Figure 5. 1: Bedrock map displaying the location of the four profiles in Figure 5.2, and the main structural elements in the area. It has been done scanline measurements in the beds of dark and light green colors, of Permian strata. The black circle marks the location of fracture studies. Map modified from Norwegian Polar Institute.

5.2.1 M1 fold and thrust province

The M1 thrust was not investigated during fieldwork, but is included in the cross-sections based on results from Bergh and Andresen (1990), map by Bergh et al. (2003) and Larsen (2009). It is termed to be the easternmost thrust, and is marked on the map (Figure 5.1) and in profile C-C' (Figure 5.2). The thrust is barely exposed at the surface, but is suggested to be in the Triassic strata between Mediumfjellet and Muslingodden, where nearly flat-lying Triassic strata meets steeply dipping Triassic strata, both of the Bravaisberget Formation. The M1-thrust is seen as a nearly horizontal thrust, and the steeply dipping Triassic strata is suggested to be part of the M2 anticline located in the hangingwall of M1 (Bergh and Andresen, 1990). The footwall of M1 is suggested to be slightly folded (Bergh et al. 2003).

5.2.2 M2 fold and thrust province

Cutting up with its tip line in the center of a huge anticline, makes the M2-thrust easier to recognize than the M1-thrust (Figure 5.1). The anticline is comprised of Kapp Starostin Formation and some Triassic strata (e.g. Bergh and Andresen 1990). The thrust in the center of the anticline is constant through the whole mountain range, but a secondary thrust cuts through the backlimb of the fold in the north (cross-section A-A' and B-B'; Figure 5.2). This results in that part of the backlimb is moved up towards the anticline hinge. The thrusting limb is less folded when moving south. The geometry of the anticline changes slightly along strike, from a more symmetric anticline in the northern part, to an asymmetric fold with a gently dipping backlimb and an overturned forelimb towards south. Folded beds of Permian rocks are observed with overlying Triassic strata (cross-section B-B'), located in the hangingwall of M2. The folded Permian strata are seen to have an abrupt stop towards the east, while it is covered further west.

Observations done by Larsen (2009) give a WSW-dipping axial plane of the fold in the north, changing into a steeply west-dipping axial plane in the south, with a changing interlimb angle (from $\sim 30^\circ$ in cross-section A-A', to $\sim 60^\circ$ in the southern part of the mountain range). Intrusions can be seen in the anticline of all cross-section-areas. Older Lower Cretaceous intrusions follow the youngest layers of Kapp Starostin Formation (e.g. Gayer et al. 1966, Smith et al. 1976, Nejbort et al. 2011, Corfu et al. 2013). According to Larsen (2009) the intrusion is a low-angle-to-bedding dyke, which along strike seems to cut the Kapp Starostin Formation. An additional intrusion was observed in the Triassic strata of cross-section A-A'.

5.2.3 M3 fold and thrust province

The oldest and steepest dipping in-sequence thrust is M3, located west of M2. This structurally uppermost thrust can easily be seen from Yoldiabukta past Gavltinden, and cuts up-section through westerly dipping rocks of both the Gipshuken Formation and Kapp Starostin Formation (Chapter 2.5; Bergh and Andresen, 1990). The thrust places Permian strata on top of Triassic shales, and is best exposed in the southern part, closest to the studied ridge (Figure 5.1). The cross-sections in Figure 5.2 display that the M3-thrust creates a hangingwall anticline, comprised of Permian strata. The anticline is asymmetric with a moderately dipping backlimb and an overturned

forelimb. Several smaller thrusts splay off from the main thrust in cross-section D-D' and cut into the overlying hangingwall, comprised of the Kapp Starostin Formation. Similar observations are described in Larsen (2009) suggesting the anticline to have a moderate to steeply dipping backlimb, and a steep to overturned forelimb with an axial plain dipping towards SW. Bergh and Andresen (1990) describes the anticline to be a broad box/chevron-type in the northern part, with an interlimb angle of $\sim 60^\circ$, changing into tight chevron and box parasitic folds related to the major anticline in the southern part. They also describe the core to be of highly deformed evaporites with overturned folds and many shear zones. The splay-faults is also observed by Bergh and Andresen (1990), measured to have a dip of $\sim 40^\circ$, all interpreted as M3-thrusts.

The areas of cross-sections B-B' and C-C' are, however, more complex. A structurally lower thrust is observed in cross-section B-B', resulting in Triassic strata that are overlain by Permian strata twice. In cross-section C-C' is a structural higher thrust nucleating from M3, cutting through the already thrusting Permian rocks. It seems to be one major anticline in the Kapp Starostin Formation associated to each of those thrusts. The nucleated thrust merges into the M3 thrust further south, and according to Larsen (2009) can this creates a relay ramp. Out of the nucleated thrust, a back-thrust have developed, making it possible to see rocks of the Gipshuken Formation at the very top.

According to the map of Bergh et al. (2003) an intrusion is present west of M3, in area of cross-section C-C', and therefore included in the cross-section. They have also been interpreted to cut through the stratigraphy of Kapp Starostin Formation in the north, while running layer parallel towards south (Larsen 2009).

5.2.4 Gavltinden fold and thrust province

The Gavltinden (G) thrust was not investigated during fieldwork, but is included in the cross-section based on results from Bergh and Andresen (1990), map by Bergh et al. (2003) and Larsen (2009). The G thrust is the westernmost thrust, dipping $20-25^\circ$ to the west, cutting through both Permian and Triassic strata. It is present from south of Mediumbreen to Triryggtoppen, and can be seen in cross-section A-A' (Figure 5.2), forming the uppermost thrust sheet in the area (Bergh and Andresen, 1990).

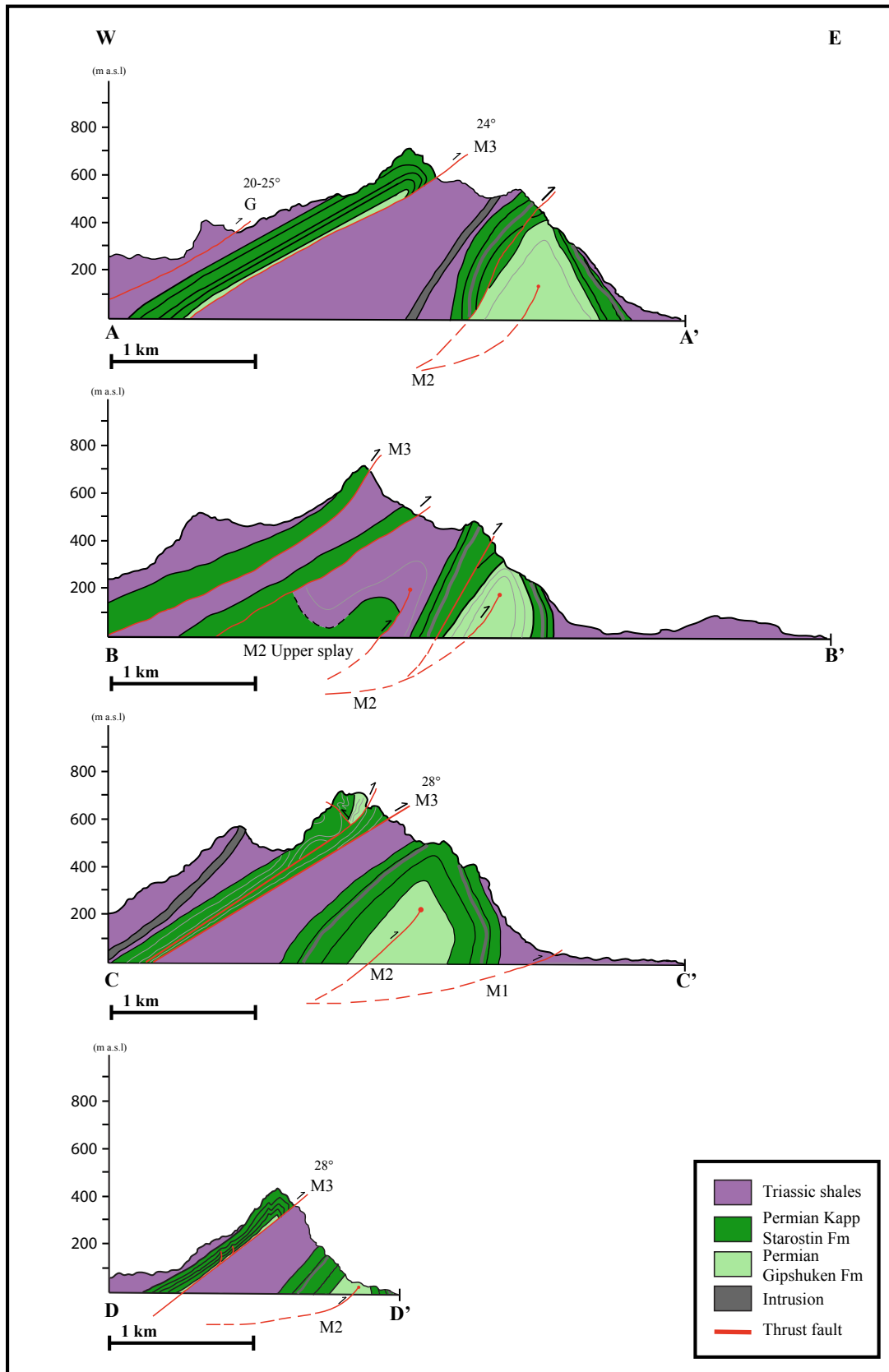


Figure 5. 2: Four geological cross-sections from Mediumfjellet. The cross-sections are based on field observations, Lidarscan interpretations and earlier work. The A-A' is the northernmost and the D-D' is the southernmost cross-section, which also is the cross-section closest to the field area. The profile displays how the structures changes in the N-S direction, and how smaller thrusts come and go while the main thrusts (M1, M2 and M3) are more or less constant. The position of the cross-sections can be seen on the map in Figure 5.1.

5.3 Lidarscan interpretations and layer parallel shortening (LPS)

The objective of this analysis is to come up with an estimate of the total shortening in the Mediumfjellet area. In a Fold and Thrust Belt there will be shortening related to deformation, with deformation happening at all scales; macro-, meso- and micro-scale (Pumpelly 1918, Ramsay and Huber 1983, Kligfield et al. 1984, Onasch and Dunne 1993, Wu 1993, Mitra 1994, Holl and Anastasio 1995, Smart et al. 1997). The macro-scale is expressed in the cross-sections. However, by analyzing marker beds in Lidarscan and applying the software Lime, it has been possible to estimate the additional shortening at a meso-scale. The recorded fracture system reflects a near micro-scale strain. The micro-, meso- and macro-scale in sum represent layer-parallel shortening (LPS).

5.3.1 Meso-scale shortening

Estimates of mesoscopic strain have been divided into:

- Fold shortening (S_F)
- Thrust shortening (S_T)
- Total shortening (E)

The fold shortening (ΔL), at a scale below that of the cross-section, is measured by finding the length of the folded bed (L_0) and the present length (L), see the following equation (1). Thrust shortening is the horizontal length from one marker bed in the footwall, to the same marker bed in the hangingwall. See the following equation (2). It is important to remember that these results are estimates. The uneven topography makes the measured line move in and out of the plane, and results in additional length in the measured marker beds (which would ideally be measured from a straight line from above). The data quality varies and the image resolution changes throughout the area. Box 1 (Figure 5.4) has a low image resolution, and it is difficult to interpret smaller thrusts. This likely reflects the results, as no thrusts has been observed and measured in box 1.

The meso-scale (100 m scale) measurements have focused on the shortening of individual beds in Mediumfjellet. The results, displayed in Table 5.1, give an average shortening per meter of the deformed beds (E), see the following equation (3):

$$(1) S_F = \Delta L = L - L_0$$

$$(2) S_T = T_1 + T_2 + T_n$$

$$(3) E = \frac{S_F + S_T}{L_0}$$

Box 1

Box 1 marks the area of an E-W striking mountainside, in the southern part of Mediumfjellet (Figure 5.3). The shortening at meso-scale has been estimated in individual beds (see Table 5.1), but because of low image resolution, no thrust shortening was possible to measure. The shortening has only been estimated in beds representing the backlimb of the anticline in M3. Most beds give a shortening below 10 percent/m, apart from bed MF1-bW that has a shortening of 26 percent/m. The high amount of shortening is due to the large fold this bed follows (Figure 5.4).

Box 2

The southern front of Mediumfjellet is presented in box 2. Parts of the mountainside are not striking E-W, which is the most convenient orientation as it then will be close to parallel to the transport direction, as in box 1 (Figure 5.3). To get the right amount of shortening, this angle therefore needs to be adjusted, assuming the mountainside has an orientation of 040° , striking NE. According to Wennberg (1994) and Bergh et al. (1997), the whole system is estimated to have a transport direction of 070° NE. The measured mountainside then needs to be adjusted 30° to get the estimated 070° . The adjusted length is calculated by using the cosinus formula. The measured and calculated lengths are given in Appendix 2, and the results can be seen in Table 5.1.

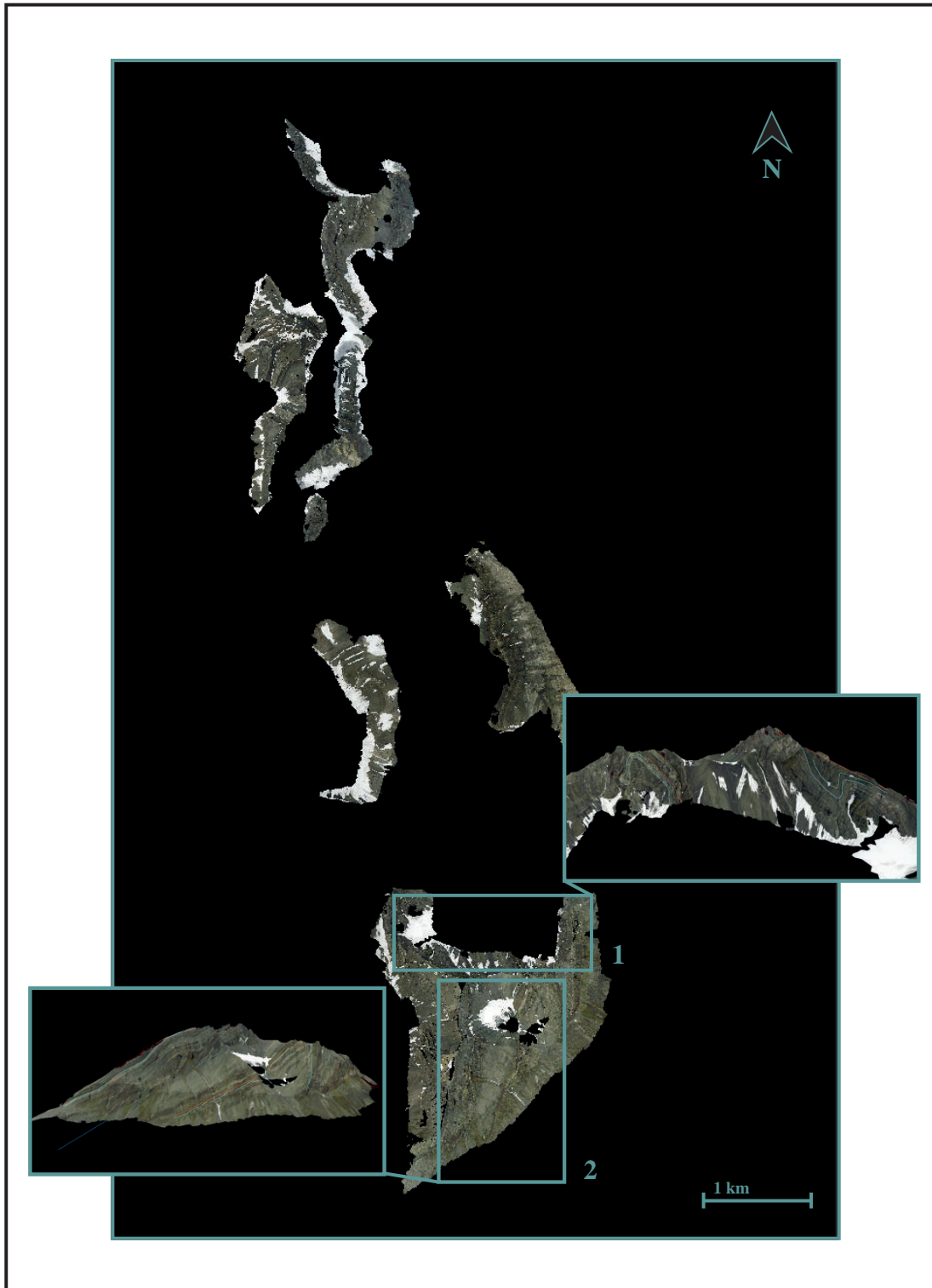


Figure 5. 3: Overview of areas covered by Lidar data, analyzed for layer-parallel shortening. The selected areas are divided into box 1 and 2, and are located in the southern part of Mediumfjellet mountain range.

Table 5. 1: Results from meso-scale shortening. The E value represents the amount of average shortening per meter for each layer. The amount of shortening is varying between beds.

Mesoscale shortening/m (E)							
Box	Measured bed	S _F (m)	S _T (m)	S _{F+T}	E _{Meso}	E _{Meso} %	Location
1	MF1-aW1	10	-	10	0.09	9	Backlimb
	MF1-aW2	6	-	6	0.06	6	Backlimb
	MF1-bW	36	-	36	0.26	26	Backlimb
	MF1-cW	3	-	3	0.03	3	Backlimb
2	MF2-a1	4	-	4	0.04	4	Backlimb
	MF2-a2	4	-	4	0.04	4	Backlimb
	MF2-a3	3	-	3	0.03	3	Backlimb
	MF2-a4	1	-	1	0.01	1	Backlimb
	MF2-a5	3	-	3	0.03	3	Backlimb
	MF2-a6	2	-	2	0.02	2	Hinge
	MF2-b1	2	-	2	0.02	2	Backlimb
	MF2-b2	7	-	7	0.07	7	Backlimb
	MF2-b3	7	-	7	0.07	7	Backlimb
	MF2-b4	2	-	2	0.02	2	Backlimb
	MF2-b5	3	-	3	0.03	3	Backlimb
	MF2-b6	24	-	24	0.22	22	Hinge
	MF2-c1	8	-	8	0.08	8	Backlimb
	MF2-c2	18	22	40	0.38	38	Backlimb
	MF2-c3	14	-	14	0.14	14	Hinge
	MF2-d1	9	-	9	0.09	9	Backlimb
	MF2-d2	2	-	2	0.02	2	Backlimb
	MF2-d3	3	-	3	0.03	3	Hinge
	MF2-e	15	10,9	25,9	0.25	25	Backlimb
	MF2-f1	13	9	22	0.22	22	Backlimb
	MF2-f2	57	36	93	0.65	65	Backlimb
MF2-g	77	-	77	0.47	47	Hinge	
MF2N-a	2	1,5	3,5	0.03	3	Backlimb	
MF2N-b1	5	-	5	0.05	5	Backlimb	
MF2N-b2	140	-	140	0.58	58	Hinge	
MF2N-b3	22	-	22	0.18	18	Forelimb	

Box 2 records the shortening of individual beds in backlimb, hinge zone and forelimb, but most of the data is taken from the backlimb (Figure 5.4). The shortening measured in beds of the backlimb is mostly below 10 percent/m, which is confirmed by the average value in Table 5.2. However, there are a few exceptions like MF2-c2 and MF2-f2, but note that all beds with a higher shortening also include thrusts. The shortening in the hinge zone is considerably greater, with an average of 24 percent/m, with no additional thrust shortening observed. There is only one shortening estimate

taken from the forelimb, which is not sufficient data to make any assumptions about the shortening.

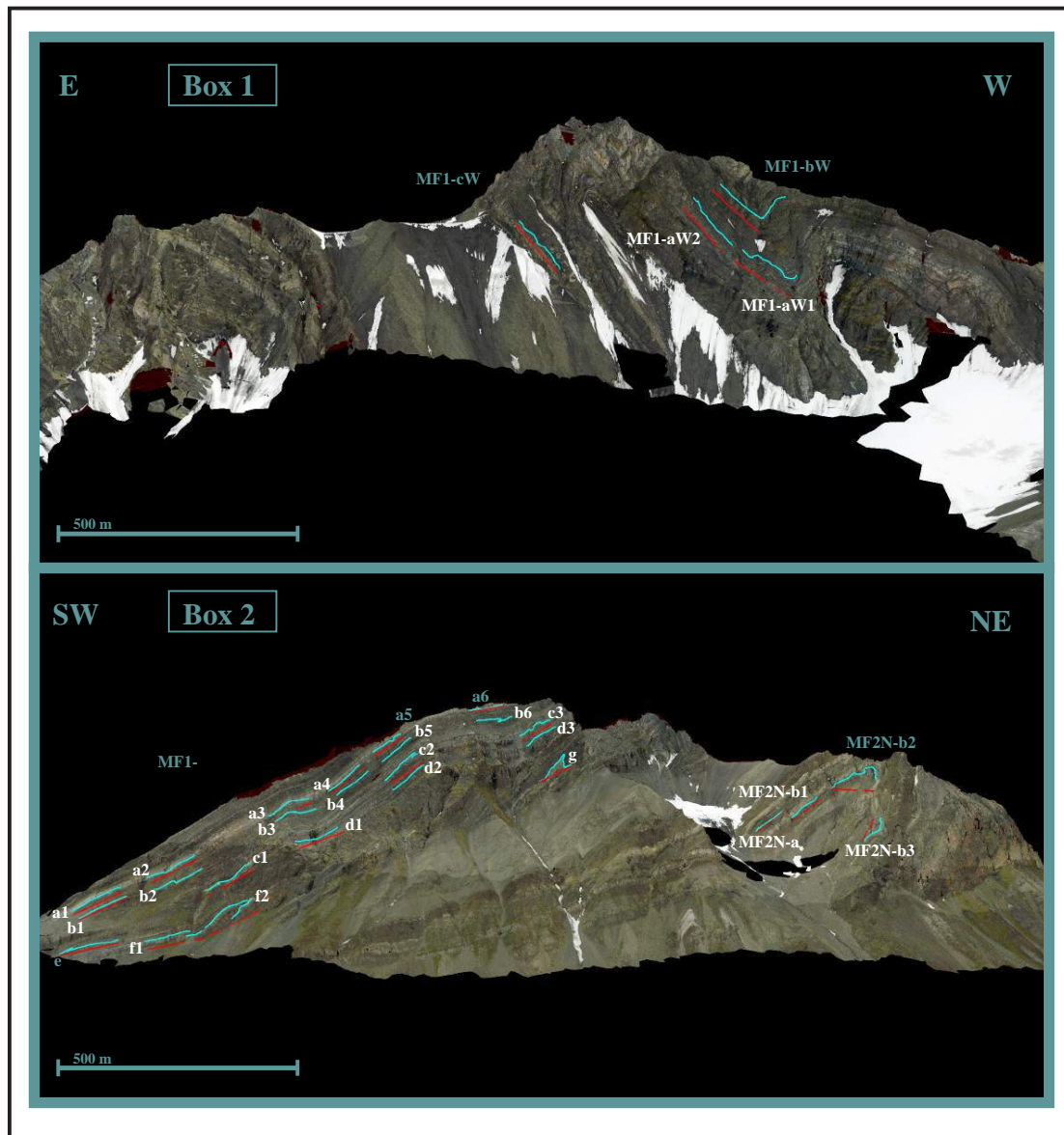


Figure 5. 4: Lidarscans displaying the mountainsides of box 1 and 2, with measured beds at meso-scale. Turquoise lines are L_0 , while red lines are L . Note the name of the measured beds.

Table 5. 2: The average total shortening (E%) in backlimb, hinge zone and forelimb. Note that the data is only from box 2.

Meso-scale average percentage shortening/m (E%)

	Backlimb	Hinge	Forelimb
Box 2	11	24	18

5.3.2 Macro-scale shortening

The macro-scale measurements have focused on the shortening of the thrust sediment packages in Mediumfjellet and the thrust shortening of these sediment packages. The fold shortening has been estimated in box 1, while measurements for both fold shortening and thrust shortening was performed for the southern front of Mediumfjellet, box 2. This is because most of the mountainside is exposed in box 2, compared to the partly glacier-covered mountainside in box 1. The total shortening estimated in box 2 will therefore represent the macro-scale shortening.

Box 1

In box 1 the fold shortening of the two major folds is estimated (Figure 5.5). The top and base of the bright marker bed was measured in both the eastern and western fold. Note that both folds show a higher amount of shortening along the base of the bed (see Table 5.3).

Table 5. 3: The shortening of the marker bed in the western and eastern fold of box 1. Note that the shortening is highest along the base of the bed.

Macro-scale shortening/m (E)						
Box	Measured bed	S_F (m)	S_T (m)	S_{F+T}	E_{Meso}	E_{Meso}%
1	MMF1-topW	145	-	145	0.27	27
	MMF1-baseW	195	-	195	0.33	33
	MMF1-topE	145	-	145	0.31	31
	MMF1-baseE	166	-	166	0.34	34

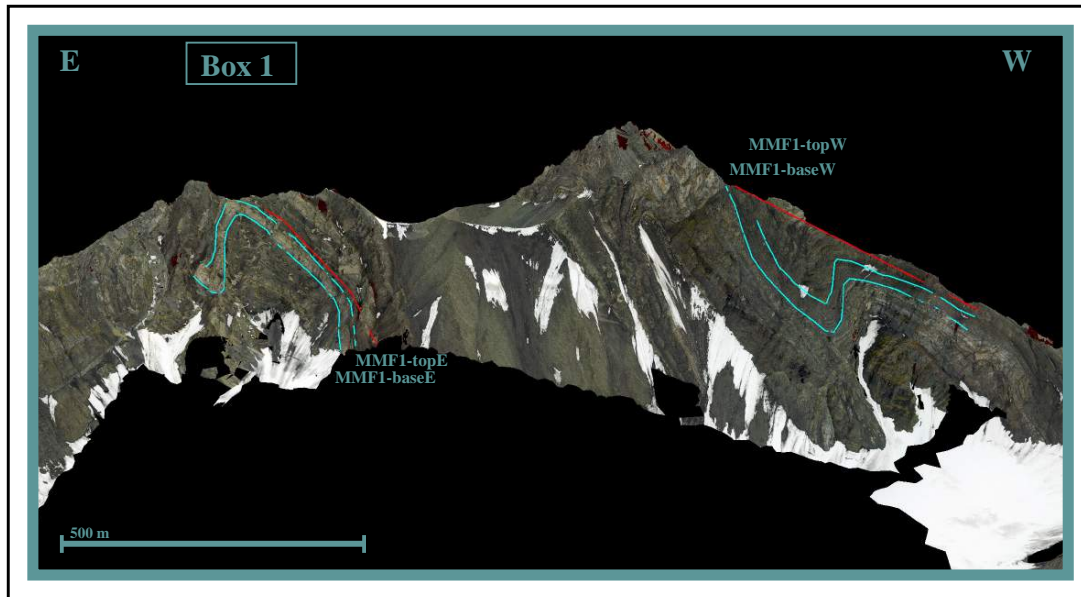


Figure 5. 5: Lidarscan displaying the mountainsides of box 1, with macro-scale measurements of the beds. The turquoise lines represent L_0 , while red lines represents L . Both folds have a higher estimated shortening along the base of the bed.

Box 2

The estimated macro-scale fold shortening in box 2 is based on the uppermost marker bed in the sediment packages (see Table 5.4; Figure 5.6). A complete table with all measurements and calculations can be found in Appendix 2.

The thrust shortening (S_T) is estimated based on a postulated geometry. By suggesting the two thrusts (M3 and M2) intersect right below the beach in front of Mediumfjellet, an estimated displacement can be measured (a straight line from the top of the mountain down to the beach). The top of the southern front of Mediumfjellet is 723 m.a.s.l., while the top of Mediumfjellet is 805 m.a.s.l. The difference is seen as minimum erosion, and the calculated length of this height difference is added to the displacement length (the height is the adjacent, while the angle for M3 = 28° is used). The thrust shortening is then calculated by using the sinus formula for a right triangle (the displacement is the hypotenuse and the angle of thrust M3 = 28°), and then corrected by using the cosinus formula) (Table 5.5).

Table 5. 4: Results from calculations of the macro-scale fold shortening (S_F) in the analyzed units 1 and 2.

Macro-scale Fold shortening (S_F)			
Measured unit	L (m)	L_0 (m)	S_F (m)
MMF2-W	990	1037	47
MMF2-E	1018	1715	697

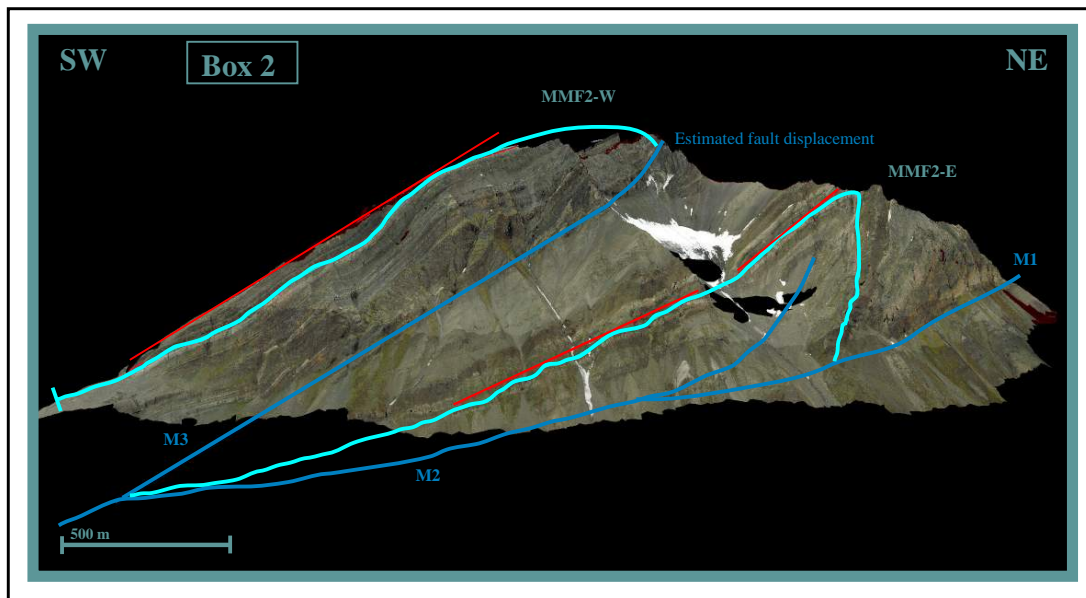
Table 5. 5: Results from macro-scale calculations of thrust shortening (S_T), due to the M3 thrust.

Macro-scale Thrust shortening (S_T)					
Measured displacement (m)	Min. erosion (m)	Added displacement (82m/cos28)	Total displacement (m)	S_T (measured) (m)	Corrected S_T (m)
1380	82	93	1473	692	599

When the fold and thrust shortening are estimated, the macro-scale average shortening per meter (E) will then be 49% (Table 5.6).

Table 5. 6: Results from macro-scale average shortening per meter (E). The estimated E value is 49 percent/m. Note that the original length, L_0 , and the fold shortening, S_F , are the sum of MMF2-W and MMF2-E in Table 5.4.

Macro-scale LPS/m (E)					
L_0 (m)	S_F (m)	S_T (m)	S_{F+T}	E_{Macro}	E_{Macro} %
2752	744	599	1343	0.49	49

**Figure 5. 6:** Lidarscan displaying the mountainside of box 2, with macro-scale measurements and interpreted major structures. The turquoise lines represent L_0 (the lines has been extended when interpreting the major structures), while the red lines represents L. The M2 and M3 thrusts are interpreted to intersect right below the surface. The thrusts are marked in dark blue.

5.3.3 Estimated total shortening in Mediumfjellet (Y)

To estimate the total shortening in the area (Y), the shortening at all scales should be included. The meso- and macro-scale shortening has previously been estimated. The remaining scale is shortening at micro-scale, which will be the shortening applied by shear fractures. The displacement of shear fractures have not been measured in the

field, but if we suggest a minimum shortening of a shear fracture to be 0.1 cm and a maximum of 1 cm, it is possible to estimate the shortening per meter of each lithology based on the fracture frequency (Table 5.7). However, the fracture frequency is based on all measured fractures, and not all are shear fractures. A great part of the measured fractures are joints, reflecting dilation, and thus will counteract the shortening. This will then be a maximum shortening estimation.

Table 5. 7: Estimated shortening at micro-scale for each lithology, based on the fracture frequency. Note that it is assumed a minimum shortening of 0.1 cm and a maximum shortening of 1 cm, for every fracture. The fracture frequency values are from Table 5.11.

Micro-scale shortening/m based on lithology (E)					
Lithology	Fracture frequency	Min. (E)	Min. E%	Max. (E)	Max. E%
Dolomite	1.93	0.002	0.2	0.019	1.93
Brachiopod limestone	1.21	0.001	0.1	0.012	1.21
Bryozoan limestone	2.29	0.002	0.2	0.023	2.29
Dark spiculite	1.68	0.002	0.2	0.017	1.68
Light-colored spiculite	1.35	0.001	0.1	0.014	1.35
Shale	1.82	0.002	0.2	0.018	1.82
Average	1.71	0.002	0.17	0.017	1.71

Based on the previous results, the total layer parallel shortening (Y) in Mediumfjellet is estimated to be minimum 64 percent/m, including the estimated minimum shortening at microscale. The maximum shortening is estimated to be 66%/m (Table 5.8). The total shortening estimations is based on the E_{micro} , which is the average shortening per meter in all lithologies, and the E_{Meso} that is the average of all measured beds in box 2.

Table 5. 8: Estimated total shortening per meter (Y) of the Mediumfjellet area. The average E_{Meso} is the average of measurements in box 2.

Total LPS (Y)				
	Average E_{Micro}	Average E_{Meso}	E_{Macro}	Y
Min. E	0.002	0.15	0.49	0.64
Max. E	0.017	0.15	0.49	0.66

5.4 Fracture characterization

The fractures are recorded from the mountain ridge southwest of Mediumfjellet thrust stack, in a long, west-dipping section (Figure 5.1). As previously described in Chapter 1.5, scanlines were made to collect fracture data. The mountain ridge has, unfortunately been covered by the surging Wahlenberg glacier in recent years. This has made the study area smaller every year.

Earlier workers (e.g. Bergh and Andresen 1990) interpreted the ridge to be a hangingwall flat over the M3-thrust. The lithology and stratigraphy are discussed in Chapter 4. All scanlines include: primarily fracture frequencies (fractures per meter), fracture orientation, lithology, bed thickness, whether the fractures were bed-confined or through-going, and other fracture characteristics as; calcite precipitation, slickensides and slip lineations where possible.

5.4.1 Bed-confined fractures (BC)

A measured fracture that only stays within one bed, independent of size, is termed bed-confined fracture (BC). BC fractures are observed in all scanlines and lithologies (Figure 5.7). Some fractures stop when they meet the bed boundary, while other fractures die out within the bed. Many of the bed-confined fractures are thin (hairline) fractures (Figure 5.7B) and very steeply dipping. Some fractures can turn into horizontal fractures, and then turn into steeply dipping fractures again (Figure 5.7C). A fracture called plumose joint was observed in the bryozoan limestone of U14, as a bed-confined fracture (Figure 5.7A). A plumose joint makes what looks like feather imprint on the fracture surface, and are created because of inhomogenities in the rock. The inhomogenities affects the stress present at the tip of the fracture, causing the fracture to bend (Woodworth, 1896).

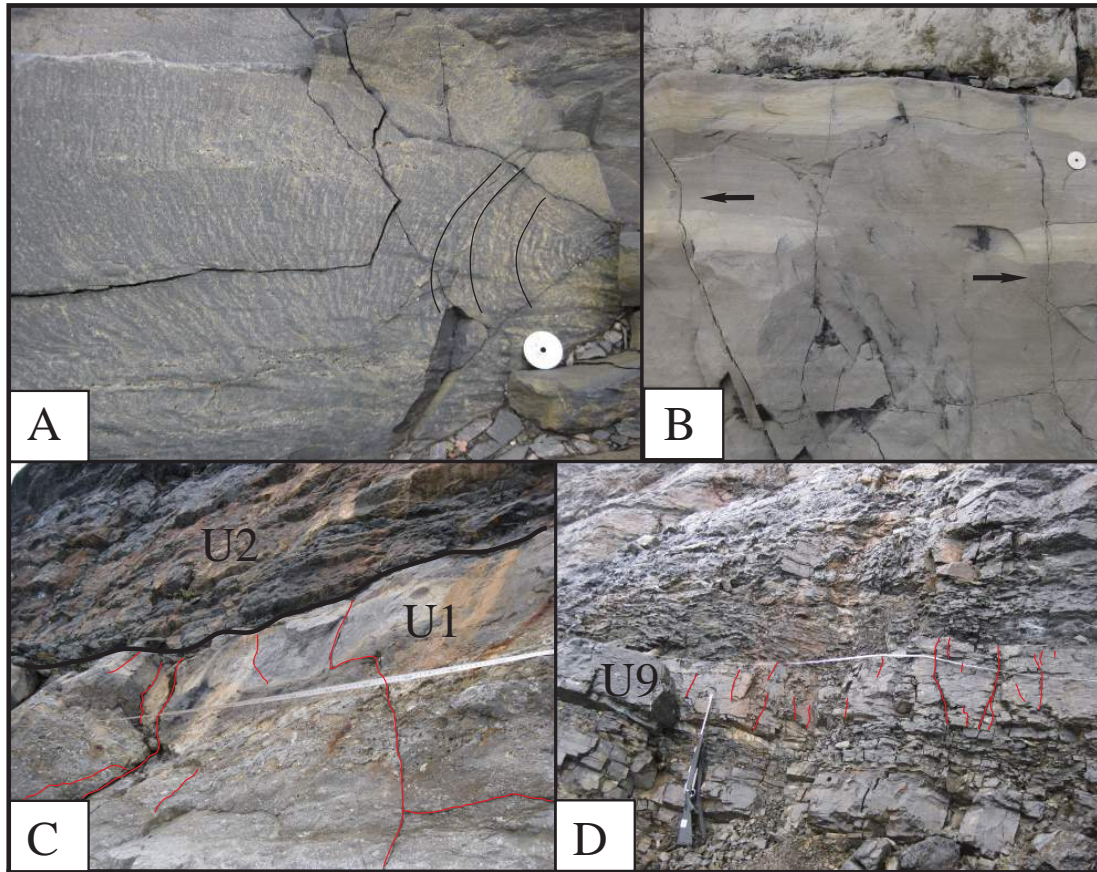


Figure 5. 7: Examples of bed-confined fractures in field. **A)** A plumose joint in the bryozoan limestone of U14. See coin for scale. **B)** Hairline bed-confined fractures in the Gipshuken Formation, U0. See coin for scale. **C)** Bed from the Vøringen Member with bed-confined fractures. One of the fractures is steep, but changes into a horizontal fracture before it changes back to a steep fracture. This fracture also arrests a low-angled fracture (to the right in the photo). **D)** Bed-confined fractures in shale (see rifle for scale).

5.4.2 Through-going fractures (TG)

Through-going fractures are not restricted by the bed, but cut through two or several beds (Figure 5.8). Through-going fractures are seen in almost all scanlines, and are present in all lithologies.

5.4.3 Calcite precipitation (CP)

Some fractures have precipitated calcite on the fracture surface, referred to as calcite precipitation (CP) (Figure 5.8A). Some fractures are open with CP on each fracture surface, while other fractures are closed because they are entirely filled with calcite. CP is observed in both BC and TG fractures, and all lithologies except shale.

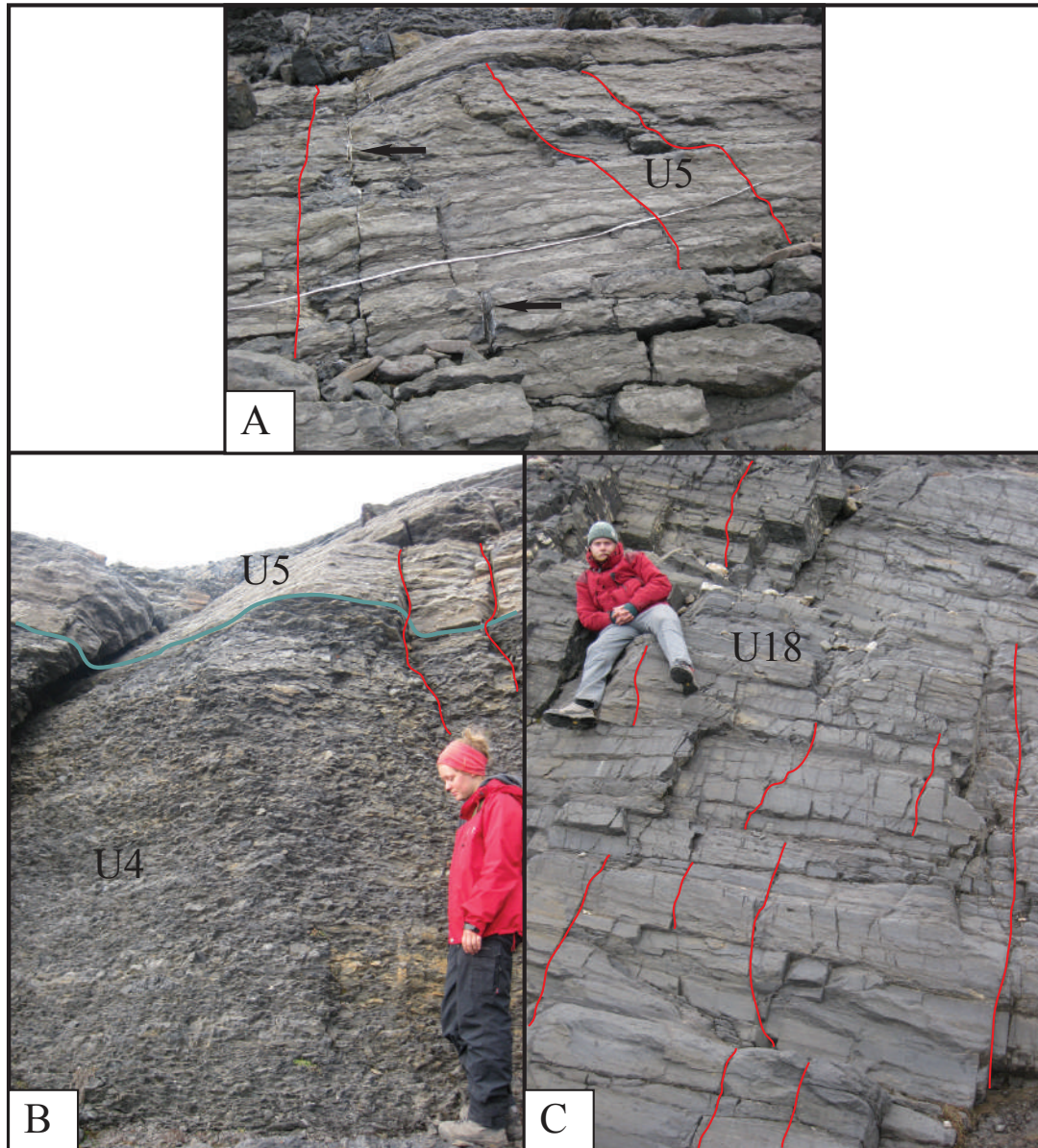


Figure 5. 8: Examples of through-going fractures in field (TG). **A)** Through-going fractures in a bryozoan limestone, U5. Some of the fractures have calcite precipitation (see arrows). **B)** Fractures going through several beds and different lithologies (through both dark spiculite and bryozoan limestone). **C)** Dark spiculite with TG fractures marked in red.

5.4.4 Slip lineations on fracture plain

Even though the fracture plain at first seems smooth and regular, it is not. When the fracture developed, irregularities in the rock made small tracks or hairline thick lines, referred to as slip lineations. These lines are made in the brittle regime by frictional sliding, and give information about the orientation the rock had when it was fractured (net slip) (Lisle and Srivastava, 2004). On a fracture plain, there can also be steps present, which indicate the direction of the slip. Steps were observed on slickensides

in scanline SAS 1.13, indicating a reverse movement. Slip lineations were only observed in four scanlines, indicating a N-S net slip (Table 5. 9).

Table 5. 9: Slickenside and slip lineation recorded in the field area. The slip lineations indicate a N-S directed net slip.

Scanline	Slickenside	Slip lineation	Lithology
SAS 1.13	Not measured	? → 190 ? → 193	Dolomite
SAS 16.13	030/52	52 → 200	Dark spiculite
SAS 18.13	058/58	48 → 180	Light-colored spiculite
SAS 5.14	Not measured	Not measured	Dark spiculite

5.5 Fracture orientation trends

To be able to see trends within the field area and distinguish trends within the different lithologies, the measured fracture orientations have been combined in stereonet. A presentation of all the fracture trends, regardless of lithology can be seen in Figure 5.9.

Plot (poles)	Plot (planes)	n (number of measured fractures)	Set	Text
		728	All data	All fracture data collected during fieldwork, displaying the main trends.
		183	1	Set 1, striking almost E-W with a steep dip towards NNW.
		137	2	Set 2, the opposing set to 1. Striking almost E-W, but with a steep dip towards SSE.
		105	3	Set 3, striking NNW-SSE, dipping steeply towards NE.
		17	4	Set 4, the opposing set to 3. Striking NNW-SSE, dipping steeply towards SW.
		75	5	Set 5, striking NW-SE, dipping steeply towards NNE.
		48	6	Set 6, striking NE-SW, dipping steeply towards SE.
		21	7	Set 7, striking NNE-SSW, dipping steeply towards SE.
		67	8	Set 8, striking close to N-S, dipping moderately towards E.
		3	9a	Set 9a, striking NNW-SSE, dipping steeply towards NE. Are based on limited data, and can be seen as something between set 3 and 8.
		4	9b	Set 9b, striking WNW-ESE, dipping steeply towards SSW. Are based on limited data.
		13	9c	Set 9c, striking NE-SW, dipping steeply towards NW.
		10	9d	Set 9d, striking NE-SW, dipping steeply towards WNW. This set is similar to set 9c, but has a steeper dip, and striking more N-S.

Figure 5. 9: Overview of all the main fracture sets. Note the difference in measured fractures for each set, and the high number of measured fractures in set 1, 2 and 3.

In total, the orientation of 728 fractures was measured, displaying two main trends in the stereonet. One trend is striking nearly E-W, dipping steeply towards NNW and SSE, referred to as set 1 and 2. The other trend is striking NNW-SSE, dipping steeply towards NE and SW, and is referred to as set 3 and 4. These sets accounts for as much as 61% of all fracture orientations measured. Figure 5.10 display sets 1 to 4 in a bryozoan limestone. There are in total eight different sets (set 1-8) with the additional set 9, displaying the accommodation sets in four subsets.

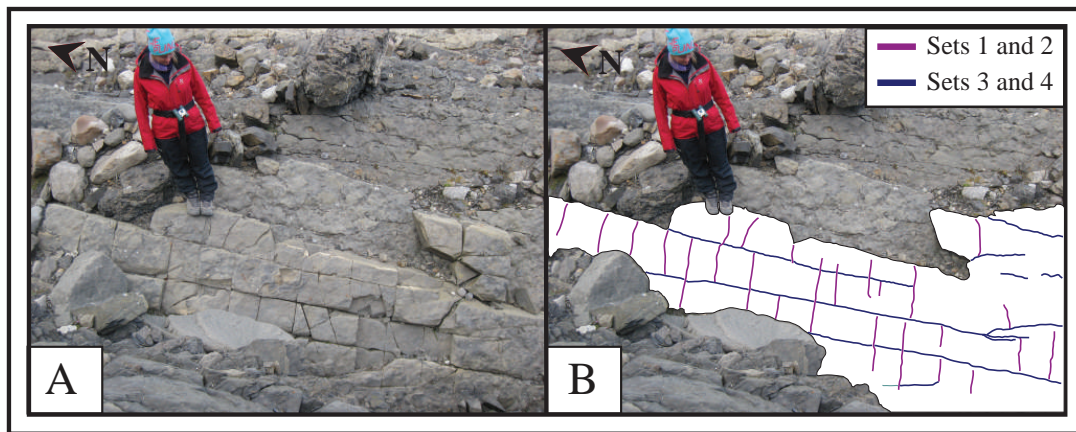


Figure 5. 10: **A)** Fractures from U13 (bryozoan limestone). Scanline was taken along strike. **B)** Interpretation of fractures on bedding surface from a photography taken in field. There is two main fracture orientation; nearly E-W (sets 1 and 2) and NNW-SSE (set 3 and 4). These sets are the major sets in the field area, but in the bryozoan limestone the major sets are sets 3 and 6.

To be able to distinguish if the different lithologies have different fracture sets, the fracture orientations have also been grouped based on lithology. Figure 5.11 displays the main fracture sets of dolomite, brachiopod limestone, bryozoan limestone, dark spiculite, light-colored spiculite and shale. The lithologies have been divided into different lithostratigraphical units (LSU). The different LSU are also displayed in Figure 5.12, linked to the lithostratigraphical log.

LSU A refers to the dolomite lithology, and show two main trends (Figure 5.11):

1. Nearly E-W striking fractures, dipping 80-90° NNW (set 1)
2. Nearly E-W striking fractures, dipping 80-90° SSE (set 2)

This is similar fracture orientations as two of the main trends displayed for all fractures (Figure 5.9).

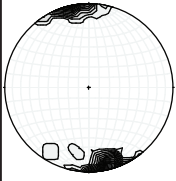
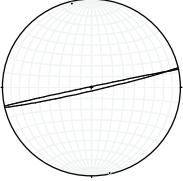
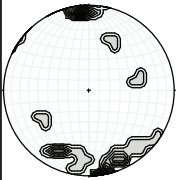
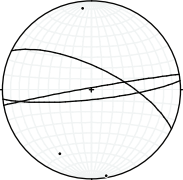
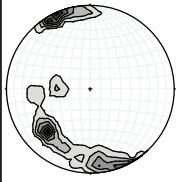
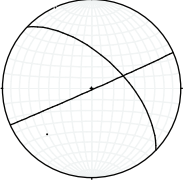
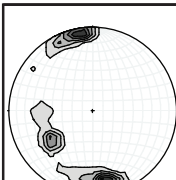
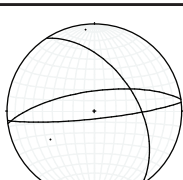
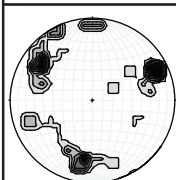
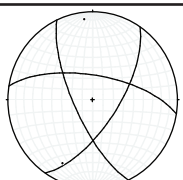
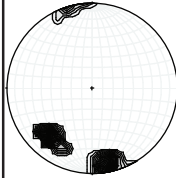
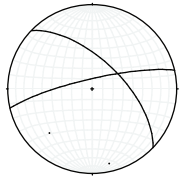
Plot (poles)	Plot (planes)	n (number of measured fractures)	Lithology	Text	Set	LSU	ff
		57	Dolomite	The main fracture sets in the dolomite of Gipshuken Fm. has a strike close to E-W. This is then set 1 and 2 fractures.	1 + 2	A	1,93
		17	Brachiopod limestone	There is three main sets in the brachiopod limestone. Two is striking close to E-W and then set 1 and 2. The third are striking NW-SE and of set 5.	1 + 2 + 5	B	1,21
		287	Bryozoan limestone	There is two main sets, striking NNW-SSE and NE-SW. The fractures striking NNW-SSE is of set 3, while the ones striking NE-SW is of set 6. Note the high number of fractures representing these sets in this lithology.	3 + 6	C	2,29
		304	Dark spiculite	There is three main fracture sets in the dark spiculite lithology. One striking NNW-SSE, which is set 3, then two are striking close to E-W and is then set 1 and 2 fractures. Note the high number of fractures representing these sets in this lithology.	1 + 2 + 3	D	1,68
		43	Light-colored spiculite	There is three main fracture sets in the light-colored spiculite lithology. One are striking NNW-SSE and represent set 4. Second is striking NW-SE, and is then set 5. The third are striking NNE-SSW, and is then of set 7.	4 + 5 + 7	E	1,35
		20	Shale	There is two main fracture sets present in the shale lithology. One striking close to E-W, which is then set 1, while the other one is striking NNW-SSE representing set 3.	1 + 3	F	1,82

Figure 5. 11: Scheme of main fracture sets in the different lithologies. Note that the bryozoan limestone and the dark spiculite have the concentration of measured fractures.

LSU B (brachiopod limestone), C (bryozoan limestone), D (dark spiculite) and F (shale) show similar main trends, and are discussed together (Figure 5.11):

1. Nearly E-W striking fractures, dipping 80-90° NNW (set 1)
2. From nearly E-W to NE-SW striking fractures, dipping 80-90° SSE/SE (set 2, 6)
3. NW-SE to NNW-SSE striking fractures, dipping 50-70° NE/NNE (set 3, 5)

The LSU of brachiopod limestone (B), bryozoan limestone (C), dark spiculite (D) and shale (F) are similar. However, when looking at the fracture frequency there is variations. This is further discussed in Chapter 5.6.

LSU E refers to the light-colored spiculite, and show three main trends (Figure 5.11):

1. NNW-SSE striking fractures, dipping 70-80° SW (set 4)
2. NW-SE striking fractures, dipping 60-70° NNE (set 5)
3. NNE-SSW striking fractures, dipping 60-70° SE (set 7)

This lithology has an unusual combination of fracture sets. The light-colored spiculite is a strong rock as reflected in the low fracture frequency ($ff = 1.35$) (Figure 5.11).

Note the distribution of measured fractures for the different lithologies. The bryozoan limestone (LSU C) and the dark spiculite (LSU D) take up ~80% of all the measured fracture orientations.

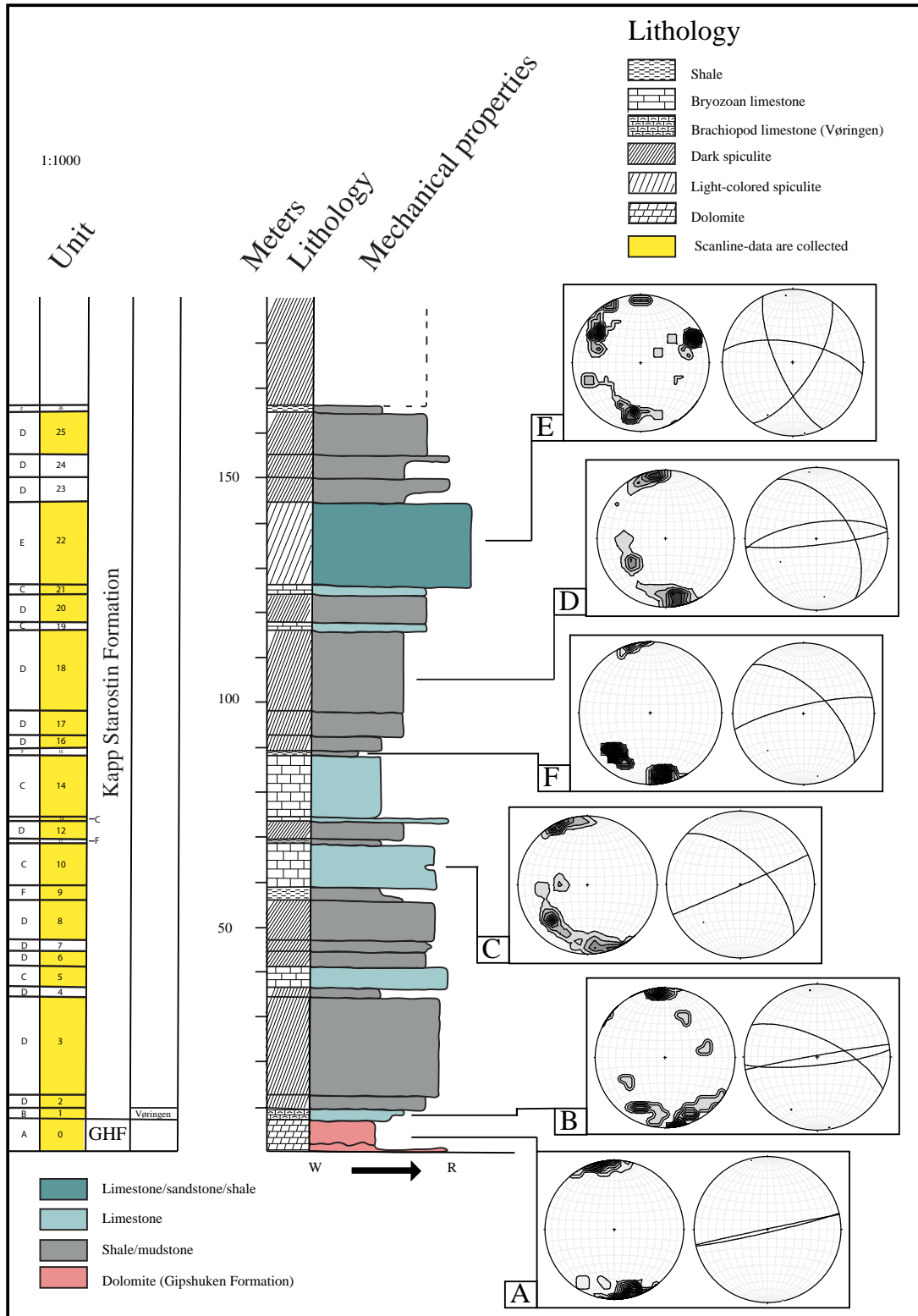


Figure 5. 12: Lithostratigraphical log with LSU. The main trends of the different LSU are displayed in schmidt net to the right of the log.

5.6 Fracture frequency variations

The statistical analysis in this section is based on presenting fracture frequency, by looking at:

- a) Fracture frequency for all fractures measured
- b) Fracture frequency for all bed-confined fractures (BC)
- c) Fracture frequency for all through-going fractures (TG)
- d) Fracture frequency for different lithologies
- e) Fracture frequency variations compared with bed thickness

By displaying the data in statistical error-bar plots, they are presented so they can give information about fracture trends. The presented graphs are made for displaying if there are any trends between fracture frequency and bed thickness.

Plots based on a, b, c and d display the fracture frequency for all scanlines measured in field, not considering the lithology or bed thickness. The average fractures per meter are shown with a dot for each scanline. Standard deviation is the boxes, and minimum and maximum values are shown as error bars with cap. The red line marks the total average. Individual plots for each scanline presenting fracture frequency for total fractures, bed-confined and through-going fractures can be seen in Appendix 3.

5.6.1 Comparing fracture frequency for all scanlines

The plot in Figure 5.13 displays the fracture frequency for each scanline and the average fractures per meter for all scanlines. Most of the scanlines have their scanline average close to or below three fractures per meter. It is only three scanline measured that has a fracture frequency as high as close to four fractures per meter. Those scanlines are SAS 1.13, SAS 12.13 and SAS 13.14A, all taken in different lithologies (see Table 5.10). The average fracture frequency is below two fractures per meter. Though, many scanlines has higher fracture frequency than two. The maximum fracture frequency is as much as nine fractures per meter, measured in a dark spiculitic bed. The main trend is however below two, as indicated by the total average (red line). Note that some of the boxes representing standard deviation go below zero, and even above the highest number of fractures per meter (e.g. SAS 7.13 and SAS 2.13). This is because standard deviation is a statistical result, not a real measured number. Any result sufficiently large enough below mean will give a negative number, as in SAS 7.13.

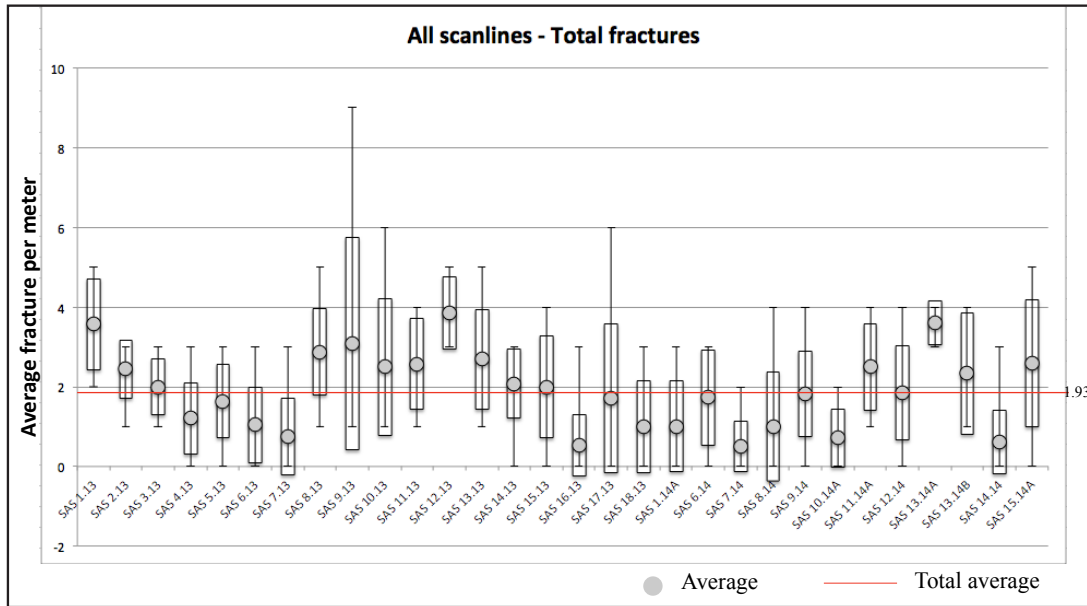


Figure 5. 13: Comparing fracture frequency for all fractures. The grey dot marks the average for each scanline, while the red line displays the total average of 1.93.

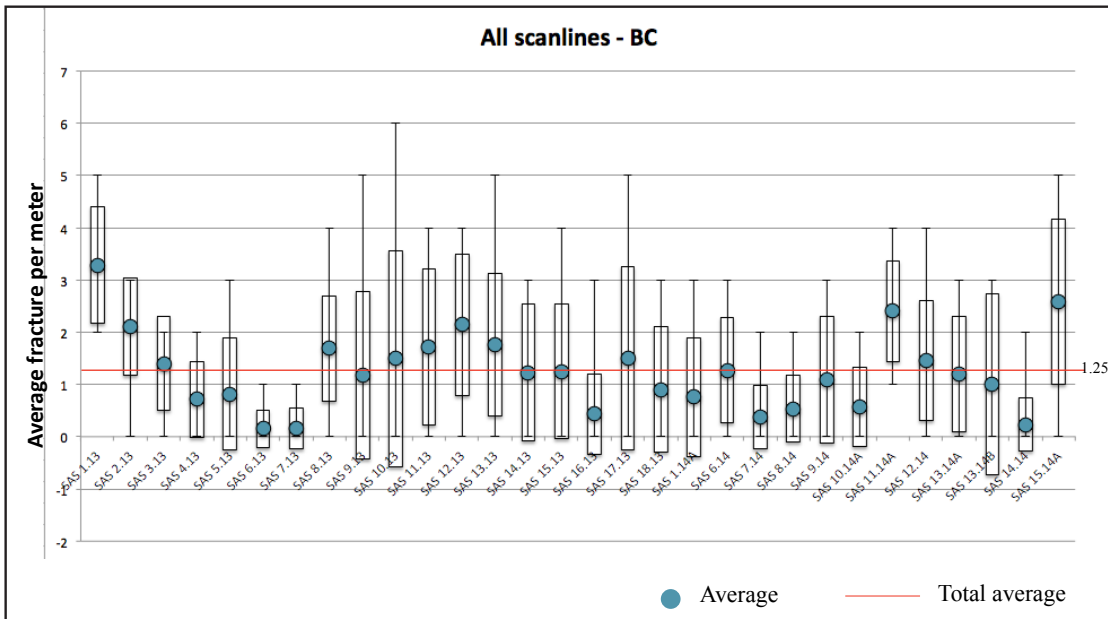


Figure 5. 14: Comparing fracture frequency for bed-confined fractures (BC). The blue dot marks the average for each scanline, while the red line displays the total average.

5.6.2 Comparing fracture frequency for bed-confined fractures

The dataset is fundamentally divided into bed-confined fractures (BC) and through-going fractures (TG). The plot in Figure 5.14 display fracture frequency for all scanlines measured in field, representing only the bed-confined fractures (BC). The data looks similar to the presentation of all data in Figure 5.13, except from the

scanlines to the right in the plot (SAS 13.14A, SAS 13.14B and SAS 14.14). They have a lower fracture frequency than what was seen in Figure 5.13, and are all collected from dark spiculite. The average fracture frequency is slightly more than one fracture per meter, which is lower than the total average for all scanlines. One scanline, SAS 1.13, differ from the rest, with an average fracture frequency above three. The scanline are taken from the dolomitic bed in the Gipshuken Formation just above the assumed location of the M3 thrust. Note that the maximum fracture frequency varies throughout the different scanlines.

5.6.3 Comparing fracture frequency for through-going fractures

TG fractures are those fractures going through two or multiple beds. These types of fractures are naturally often more evolved. The plot in Figure 5.15 shows fracture frequency for all scanlines measured in the field, representing only the through-going fractures (TG). The total average clearly shows that there are less through-going fractures present in the field area, than bed-confined fractures. The total average is only 0.68, compared to the total average in the BC plot of 1.25. All scanlines except SAS 9.13 (dark spiculite), SAS 12.13 (bryozoan limestone) and SAS 13.14A (dark spiculite) have the scanline average fracture frequency close to or below one. Except the scanline SAS 13.14, all scanlines has at least one meter where no through-going fractures have been measured.

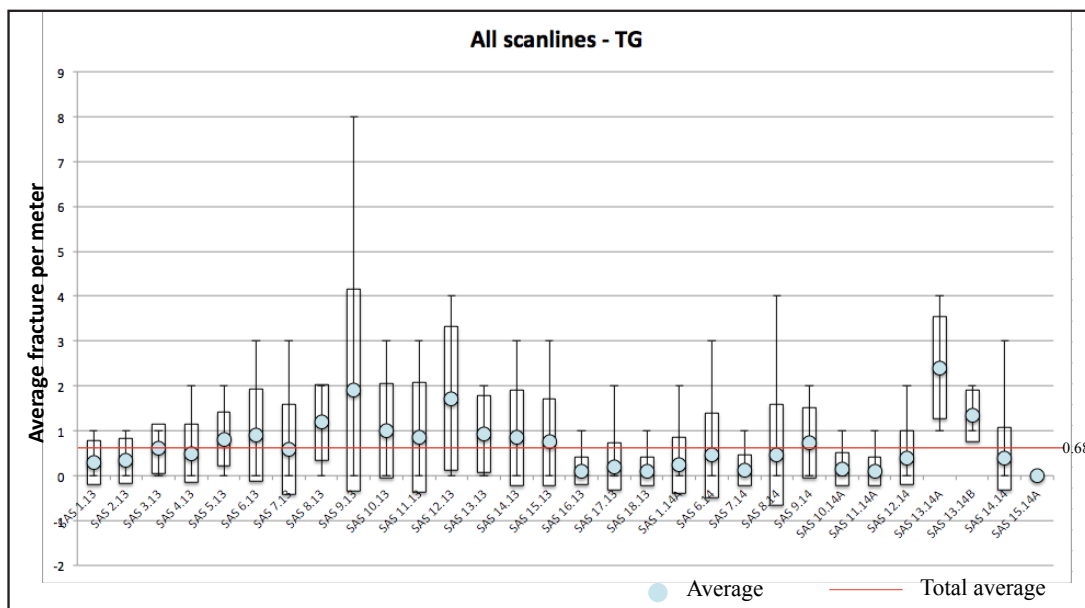


Figure 5. 15: Comparing fracture frequency for through-going fractures (TG). The light blue dot marks the average for each scanline, while the red line displays the total average.

5.6.4 Comparing fracture frequency for lithologies

A fracture frequency plot are presented for the different lithologies studied in the field area:

- Dolomite
- Brachiopod limestone
- Bryozoan limestone
- Dark spiculite
- Light-colored spiculite
- Shale

Figure 5.16 presents the fracture frequency for all scanlines measured in the field, grouped after lithology. Table 5.10 display the lithology each scanline are collected from. The fracture frequency plot shows no clear trend for any of the lithologies, however it is mainly the bryozoan limestone and the dark spiculite that has sufficient data to distinguish a trend. This reflects that ~80% of the study area is comprised of bryozoan limestone and dark spiculite. The bryozoan limestone has a fracture frequency between two and three fractures per meter, having most of the scanline averages above the total average (red line). The dark spiculite has a lower average fracture frequency. In this lithology most of the scanlines have their average close to or below two. Table 5.11 gives a short overview of the data from the plot in Figure 5.16. The plot and table (Figure 5.16; Table 5.11) show that the bryozoan limestone generally has a higher fracture frequency than the dark spiculite. If focusing on maximum and minimum values of fracture frequency, the result is however different. The dark spiculite has a much higher maximum value of fractures per meter, than what is present in the bryozoan limestone. It is important to notify that some of the dark spiculite beds were so fractured it made it difficult to distinguish the actual fractures.

Table 5. 10: Overview of the scanlines taken in the different lithologies.

Lithology	Scanlines
Dolomite	1.13, 2.13, 3.13
Brachiopod limestone	4.13
Bryozoan limestone	6.13, 10.13, 11.13, 12.13, 13.13, 1.14, 3.14, 11.14, 12.14, 15.14
Dark spiculite	5.13, 7.13, 8.13, 9.13, 14.13, 15.13, 16.13, 2.14, 4.14, 5.14, 6.14, 7.14, 8.14, 10.14, 13.14, 14.14
Light-colored spiculite	17.13, 18.13
Shale	9.14

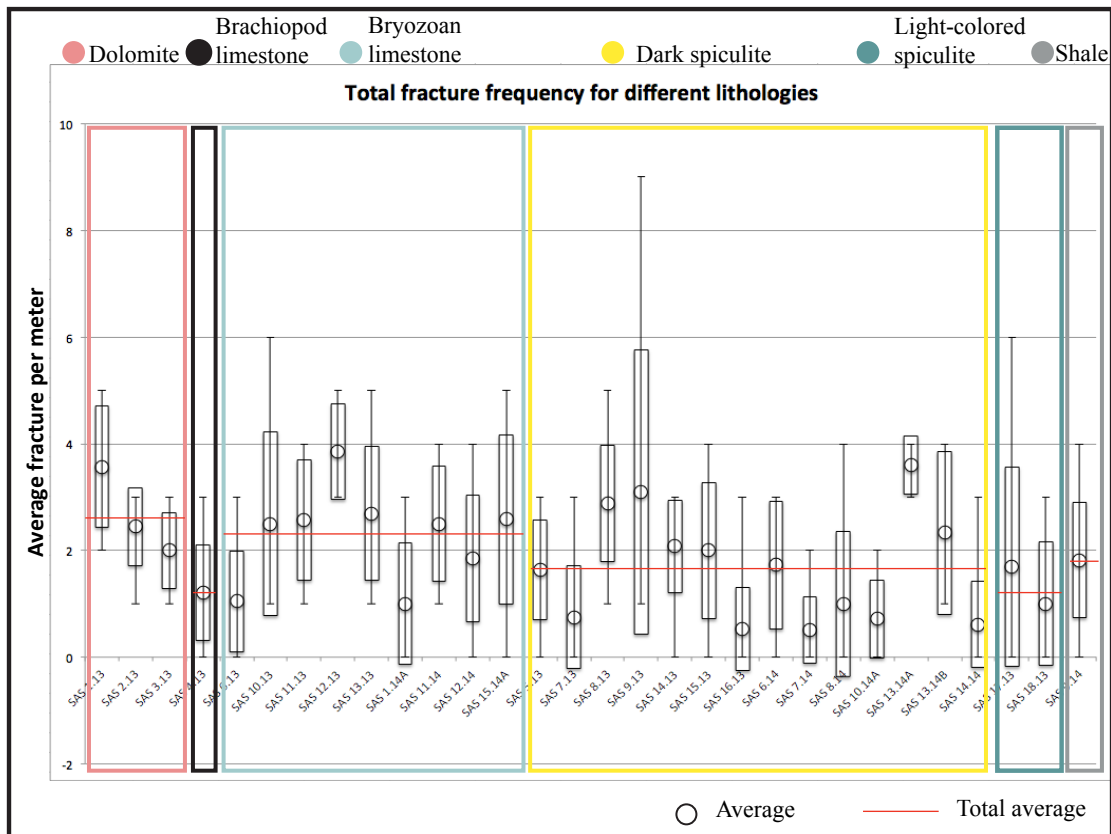


Figure 5. 16: Comparing fracture frequency for lithologies. The dot marks the average for each scanline, while the red line displays the total average of each lithology. Note that only bryozoan limestone and dark spiculite have sufficient data for interpretations.

Table 5. 11: Total average fracture frequency for all scanlines recorded in the different lithologies

Lithologies	Fracture frequency, Total average	Max	Min	Number of scanlines
Dolomite	1.93	5	1	3
Brachiopod limestone	1.21	3	0	1
Bryozoan limestone	2.29	6	0	10
Dark spiculite	1.68	9	0	16
Light-colored spiculite	1.35	6	0	2
Shale	1.82	4	0	1

5.6.5 Fracture frequency compared with bed thickness

The following plots display the fracture frequency compared with bed thickness for all scanlines. The thickness was measured as true bed thickness where it was possible, and estimated when needed. Figure 5.17 presents the fracture frequency compared with bed thicknesses measured in field, regardless of lithology. The bed thickness was sometimes fluctuating, and two beds could merge into one laterally.

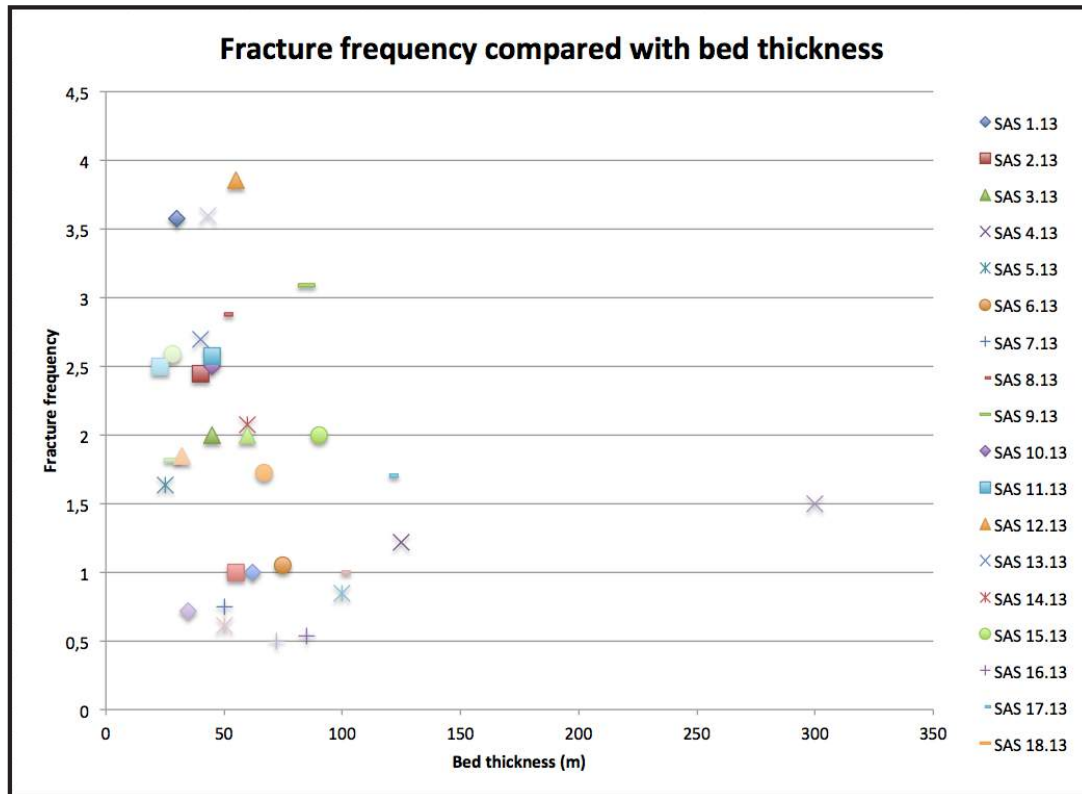


Figure 5. 17: Plot displaying all scanlines measured compared to bed thickness. A diffuse trend gives a higher fracture frequency for thinner beds.

The plot in Figure 5.17 shows a spread in data where there are 0-2 fractures per meter, being present in beds from ~30 cm to about 1.5 m. When the fracture frequency becomes higher than two, it is mostly in thinner beds with a thickness of 50 cm or less. This suggests higher fracture frequency in thinner beds than in thicker beds, but the trend are diffuse. This plot is for all data and includes all lithologies. To see if this applies to all or just some lithologies, a second plot are made (Figure 5.18).

Focusing on the two lithologies that have sufficient data, the plot in Figure 5.18 display trends for both bryozoan limestone and dark spiculite.

The bryozoan limestone seems to have a weakly expressed trend of a higher fracture frequency in thinner beds. Either there are 1 or 4 fractures per meter; they are all in beds with a thickness of ~30-70 cm. The dark spiculite have generally thicker beds, were 0-2 fractures per meter are normal in 35-100 cm thick beds.

The plot shows that the bryozoan limestone has a higher fracture frequency than the spiculite beds. The spiculitic beds are generally thicker, and have a lower fracture frequency. This fits the diffuse trend that was given in Figure 5.17, where thicker beds have less fractures per meter than thinner beds.

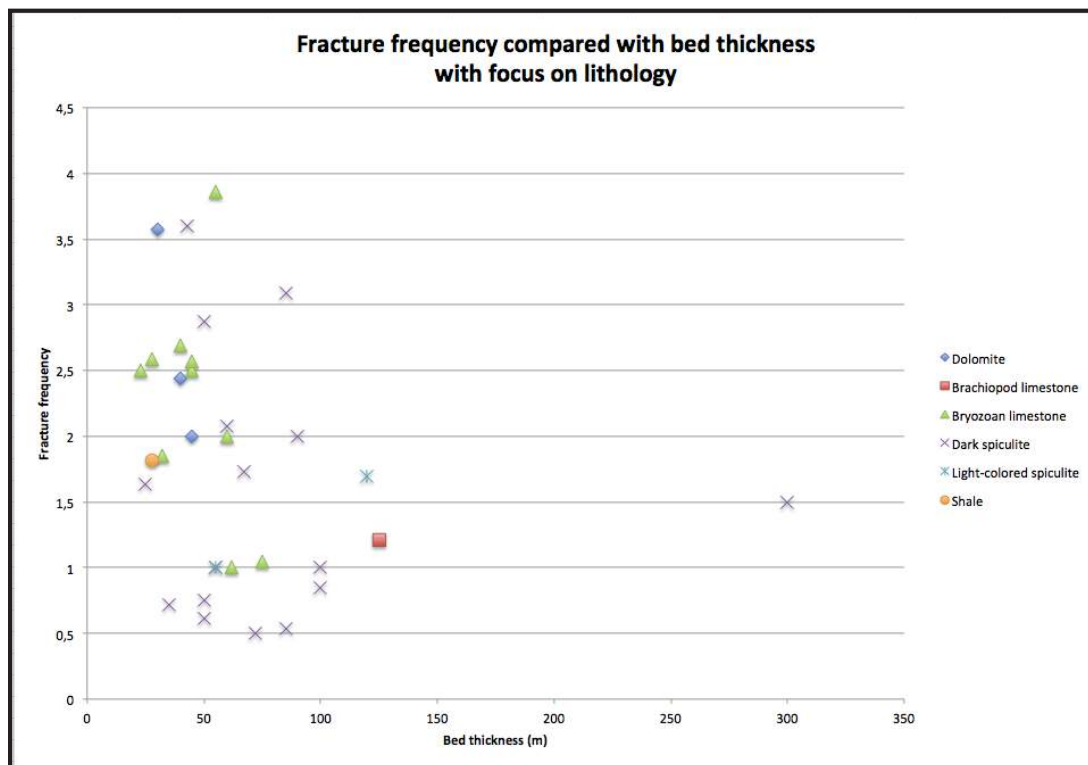


Figure 5. 18: Plot displaying all scanlines measured compared to bed thickness, with focus on lithology. Only bryozoan limestone and dark spiculite have sufficient data to be discussed. The bryozoan limestone gives a trend of higher fracture frequency in thinner beds, while the dark spiculite does not have a clear trend.

To better distinguish a trend for bryozoan limestone and dark spiculite, a log-log plot has been made out of the plot in Figure 5.18, with additional linear trend lines (Figure 5.19). As the previous plots (Figure 5.17; Figure 5.18) the log-log plot shows no clear trends either for the bryozoan limestone or dark spiculite. The bryozoan limestone gives the best-fit linear trend line of the two lithologies ($R^2 = 0.18$). It is however low,

and does not confirm any clear trend between bed thickness and fracture frequency for either bryozoan limestone or dark spiculite.

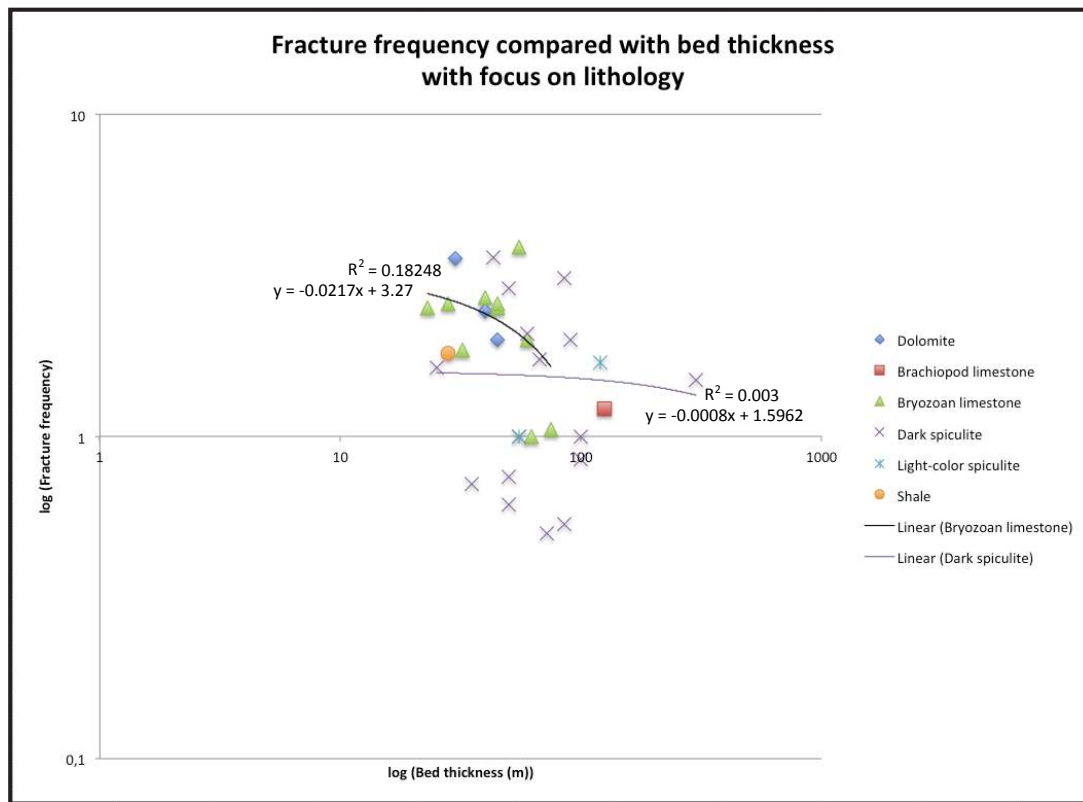


Figure 5. 19: A log-log plot of bed thickness compared to fracture frequency that give a best-fit line of $R^2 = 0.182$ for the bryozoan limestone, and $R^2 = 0.003$ for the dark spiculite. The result does not support any trend between the bed thickness and the fracture frequency.

5.7 Microtextural analysis

This chapter will present the thin sections that have been made from the sampled rock specimens. A total of 11 thin sections were made, and 5 of these were selected for further studies under the SEM (scanning electron microscope). The SEM study gives a better understanding of the different lithologies (mineralogy and texture). An ordinary optical microscope was used (see Chapter 1.6.6) to observe fractures and to distinguish various minerals and their abundance, in plane polarized and cross-polarized light. However some minerals are hard or even impossible to recognize under the optical microscope. The backscatter-electron microscopy (BSE) allows the mapping of chemical elements in various components of the sample, which subsequently facilitates the identification of the mineralogy of allochems and cement. Although

abundant brachiopods and bryozoans were observed at outcrop, surprisingly few were observed in the thin sections.

However, the BSE has its limitations as well, e.g. fractures filled with calcite cement cannot be deciphered from the calcitic matrix if their elemental composition are similar. This will also be the case for spicules in a spiculitic matrix (Goldstein et al. 1981).

5.7.1 Observations

The table (Table 5.12) offers an overview of all the studied thin sections, and those inspected further under the SEM. All samples show a mixture of carbonate and silica, and most rocks are fractured. Calcite and dolomite can be difficult to separate under the optical microscope and are therefore described as calcite/dolomite from observations under the optical microscope. The samples are divided into those lithologies suggested in Chapter 4, which they are sampled from (see Figure 4.3).

Table 5. 12: Studied thin sections. Out of the 11 thin sections made, 5 were studied further under the SEM. Note that two samples were taken of U8, one during fieldwork in 2013(a) and one in 2014 (b). See Chapter 4 for lithology descriptions.

Thin section	Lithology	SEM	Spicules	Fractures
U0	Dolomite	Yes	No	Yes, filled with quartz
U2	Dark spiculite	No	Yes	Yes, filled with calcite/dolomite and quartz
U3	Dark spiculite	No	Yes	Yes, filled with calcite/dolomite and quartz
U5	Limestone	Yes	Yes	No
U8a	Dark spiculite	No	Yes	Yes, filled with calcite/dolomite
U8b	Dark spiculite	Yes	Yes	Yes, filled with quartz
U14	Limestone	Yes	Yes	Yes, open
U17	Dark spiculite	No	Yes	Yes, filled with calcite/dolomite
U18	Dark spiculite	No	Yes	Yes, filled with quartz
U22	Light-colored spiculite	No	Yes	Yes, filled with calcite/dolomite and quartz
U24	Dark spiculite	Yes	Yes	Yes, filled with calcite/dolomite and quartz

Sample U0 from Gipshuken Formation

The thin section from U0 has a dark matrix (both in planar polarized and cross polarized light) with pearly white colored sub-angular to well-rounded allochems, fractures filled with quartz, and calcite cemented macro-pores (Figure 5.20A). The longest axis of the pearly white colored allochems are ~0.2 mm. The cement filling macro-pores has a similar pearly white color, up to 1.5 mm on the longest axis, with clear twinning. Opaque minerals are also present. U0 was chosen for the SEM, and several elemental analyses were performed. The analyses were performed on three different areas of the sample, and the results from Test 1 are displayed in Figure 5.21. The SEM results indicate a matrix rich in Ca, Mg and Si. There are abundant crystals rich in Ca and Ca-Mg, with some crystals rich in iron sulphate. See Appendix 5 for all the SEM elemental results.

Interpretation:

This is a rock with allochems floating in a matrix rich in dolomite, calcite and silica, with calcite cement filling macro-pores. The thin section is classified according to Dunham (1962) as a mudstone to wackestone. The calcite/dolomite ratio was not distinguished, but because this sample is from the Gipshuken Formation, it is suggested to be a dolomite (Lauritzen 1983).

Samples from bryozoan limestone, Kapp Starostin Formation

The two thin sections, U5 and U14, consist of a micritic matrix. There are also monaxon sponge spicules present, where an abundance of spicules are replaced with calcite. U5 is full of chaotically oriented sponge spicules (up to 0.38 mm long) floating in a micritic groundmass (Figure 5.20B). Elemental analysis of matrix and spicules revealed that the former is composed of a Si-rich matrix with spicules composed of Ca. A white circular feature filled in with matrix, with a diameter of ~50 μm , consists of iron sulphide. A photo is displayed in U5 Test 2 in Appendix 5. There were also observed white framboids of iron sulfide in both thin sections. Except from the spine of a brachiopod (0.2 mm in diameter), few micro- and macro- fossils of bryozoans have been observed. It is only observed fractures in U14, which have hairline thin open fractures. See Appendix 5 for all element measurements.

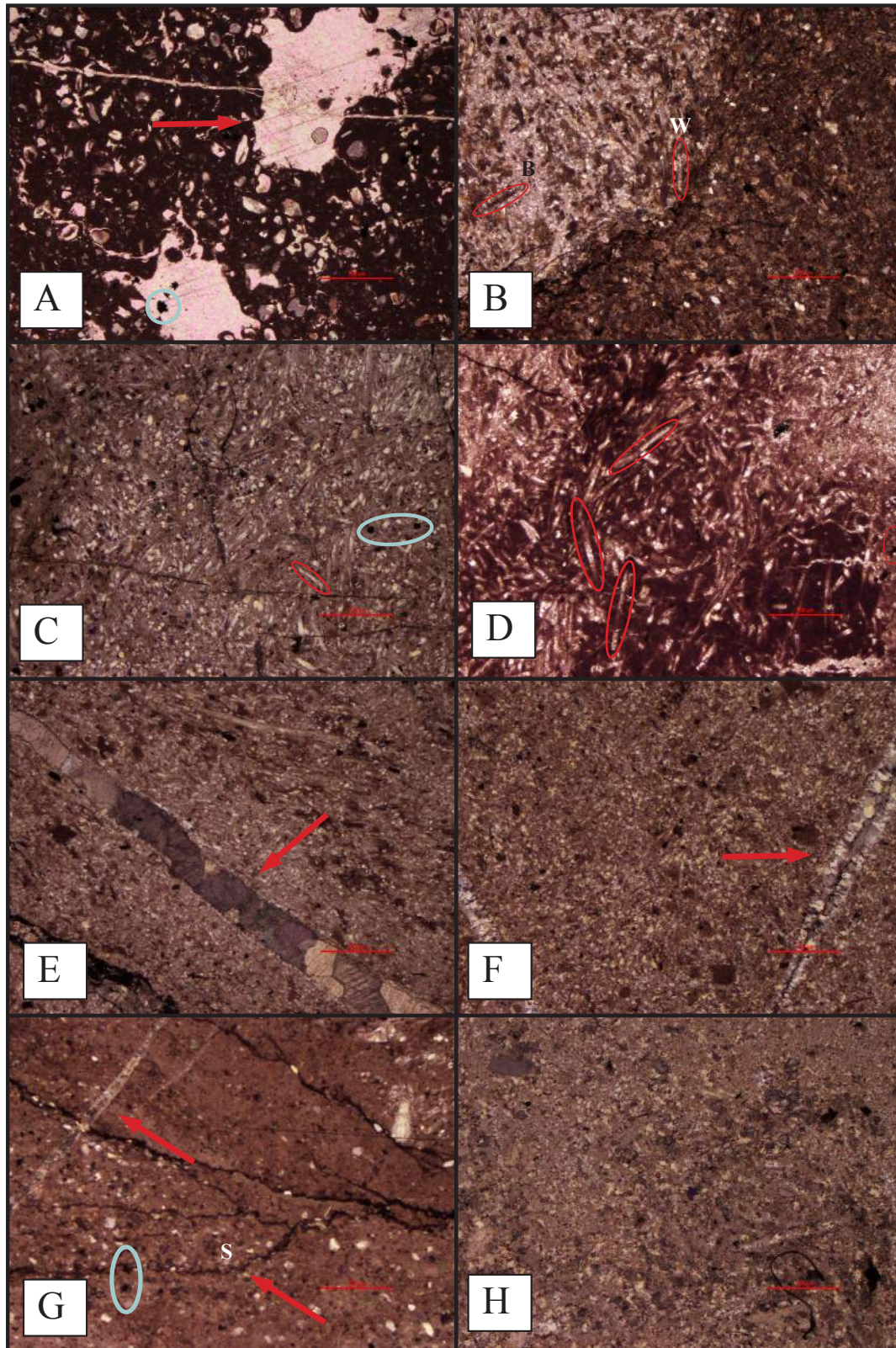


Figure 5. 20: Photos taken with an optical microscope of selected thin sections. All photos are taken in cross-polarized light. **A)** Thin section of U0, where the arrow point towards calcite cement filling in a macropore. The cement has twinning. The turquoise circle marks an opaque mineral. **B)** Thin section of U5 (bryozoan limestone) is full of chaotically oriented spicules floating in a fine-grained matrix of mainly calcite/dolomite, and silica-rich crystals. Red circles mark spicule (W) and spicule replaced with calcite (B). **C)** U17 (dark spiculite); the red circle marks a spicule in the thin section. Several spicules can be observed. Some opaque minerals are encircled in turquoise (black minerals). **D)** U24 (dark spiculite); thin section with abundant spicules (marked by red circle). **E)**

U3 (dark spiculite); a fracture filled with calcite/dolomite (marked by the red arrow). Note the twinning of the crystals. **F**) U3 (dark spiculite); a fracture filled with quartz (marked by the red arrow). **G**) U8 (dark spiculite); arrow points towards a calcite/dolomite filled fracture. The turquoise circle marks two opaque minerals. Note the incipient stylolites marked by the red arrow (S). **H**) Thin section of U22, the light-colored spiculite. Very few spicules are observed, but it is rich in microcrystalline quartz. Note red line (500 μm) for scale.

Interpretation:

The microtextural analysis of U5 gives a silica-rich matrix and lots of calcite-filled sponge spicules. U14 has a similar texture and composition, but with less abundant sponge spicules. They are both classified as limestones (mudstone to wackestone) because the components are bioclastic dominated. However they are not technically limestones *per se*, because the silica-rich matrix and additional silica-rich spicules make up more than 50 % of the samples (Ehrenberg et al. 2001). It will continued to be determined as a bryozoan limestone, based on the outcrop studies described in Chapter 4 and that it is bioclastic dominated. The white framboids in both of the samples are made up of iron sulphide. This micromorphological feature is typical for pyrite, and based on their chemical composition and morphology; they are suggested to be pyrite crystals. The mineral in the circular infilled feature, of iron sulphide, is more difficult to distinguish, and further discussed in Chapter 5.7.2.

Samples from dark spiculite, Kapp Starostin Formation

Several thin sections are studied from the lithology termed dark spiculite (U2, U3, U8a, U8b, U17, U18 and U24). They are all more or less dominated by sponge spicules (Figure 5.20C and D). The monaxon sponge spicules are up to 0.5 mm long, and are locally chaotically oriented and locally parallel oriented. Some spicules are crosscut, and have a diameter of up to 0.02 mm. SEM studies revealed that not all spicules are rich in silica, but instead replaced with calcite, as observed in U5 and U14.

The matrix is microcrystalline and difficult to distinguish in an optical microscope. The chemical element analysis in backscatter secondary electron (BSE) mode indicates a Si-rich matrix of samples U8b and U24. While studies under an optical microscope show calcite-cemented macro-pores in some of the thin sections (U2 and U17), with the longest axis of ~ 1 mm. The elemental analysis under (BSE) of thin section U2 gives a chemical composition of both Ca and a high Ca-Mg ratio. Fractures are present in all the studied thin sections, and are up to 0.09 mm wide (Figure 5.20E, F and G). U8b is highly fractured, with quartz-filled fractures. Some thin sections have

fractures only filled with quartz, others have only calcite/dolomite filled or both (see Table 5.12). The calcite/dolomite crystals present in the fractures are mostly anhedral, with twinning and up to 0.8 mm on the longest axis. The relief is high in cross-polarized light. The quartz crystals present in fractures are anhedral. In U3 the fractures filled with calcite/dolomite crosscuts the fractures filled with quartz (also observed in U2). Two thin sections are taken from U8. The fractures observed in U8a are filled either with calcite/dolomite or quartz and have incipient stylolites present, while the fractures in U8b are only filled with quartz.

Opaque minerals are observed as well and are displayed in Figure 5.20C. Observations under the SEM showed white framboids of iron sulfide in both thin sections. See Appendix 5 for all element measurements.

Interpretation:

The microtextural analysis of this unit reveals that it is dominated more or less by sponge spicules, in a silica-rich clayey matrix. The BSE elemental analysis confirms the observations done in an optical microscope, of calcite and dolomite filled macropores. The fractures filled with different minerals in U8a and U8b might indicate local variations in diagenesis. The crosscutting calcite/dolomite-filled fractures in U2 and U3 indicate a paragenetic sequence where the oldest fractures are quartz filled, and younger fractures are filled with calcite/dolomite. Based on its chemical composition and morphology the framboids rich in iron sulphides are interpreted to be pyrite. It is then suggested that many of the opaque minerals observed under an optical microscope are pyrite crystals. In field, U24 was seen as a unit rich in pyrite crystals. Based on the previous interpretation pyrite have been observed in thin section U24, but not as abundant as expected. A photo of some pyrite crystals taken with the SEM, from the thin section of U24, can be seen in Figure 5.22.

Sample from light-colored spiculite, Kapp Starostin Formation

The thin section U22 was taken from the bright-colored marker bed, named earlier as light-colored spiculite. The sample contains poorly sorted monaxon sponge spicules, up to 1 mm in length. However, the major component is microcrystalline quartz. Observations of the microcrystalline quartz under an optical microscope show anhedral crystals with extinction, but no twinning. The crystals are nearly transparent and difficult to observe in planar parallel light, but are easy to distinguish in crossed

polarized light, meaning they are of first order interference colors, and determined to be quartz crystals (Figure 5.20H). Based on its rhombohedral morphology one dolomite crystal are distinguished. Some calcite crystals with longest axis of 0.3 mm, and some opaque minerals are also observed. They are all observed under an optical microscope, and all have a high relief in cross-polarized light.

Interpretation:

The microtextural analysis of this unit indicates a highly silicified rock, where some sponge spicules are observed. Originally this unit has most likely been almost entirely built up of sponge spicules. Dissolution and precipitation of the sponge spicules has made it into a chert (Ehrenberg et al. 1998). Based on its origin and its bright color, it is decided to continue using the name light-color spiculite.

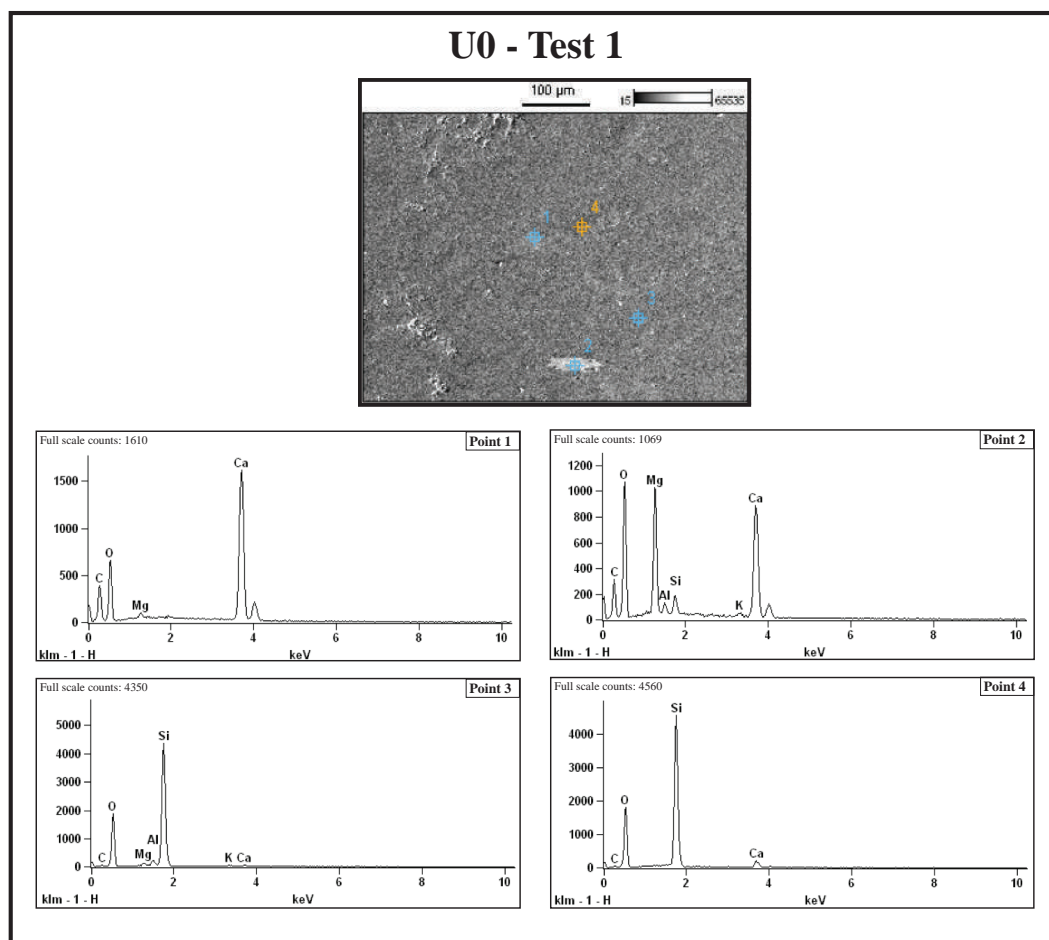


Figure 5. 21: Photo and graphs from spot analysis of sample U0. The four measurement spots are labeled with numbers in the photo, and corresponding elemental results are shown in the graphs below. The results indicate a clayey matrix, but carbonate is also a major component.

5.7.2 *Conclusions from thin section studies*

The main components in the Kapp Starostin Formation are silica-rich minerals and calcite/dolomite, with subordinate pyrite. This was expected, based in outcrop observations and rock samples (see Chapter 4). The amount of sponge spicules is very high, even in the carbonate units. In general, the lithology in the Kapp Starostin Formation is highly silicified.

In several thin sections it is observed needles filled with calcite. These are spicules that have been dissolved and later replaced with secondary carbonate cement. This resulted in a higher percentage of carbonate in the samples. In thin section of U14 there is a mixture of silica spicules and calcite-replaced spicules, while in U5 the majority of the sponge spicules are replaced with calcite. Fractures have been observed in all thin sections except U5. The calcite/dolomite filled fractures cross-cutting the quartz-filled fractures in U2 and U3 might suggest two generations of fracturing. U5 also has a white circular infilled feature, made up of iron sulphide (FeS_2). This is interpreted to be a fossil, which has been replaced by pyrite. The same clear white color can be found on framboids, also made of iron sulphide, which makes them pyrite crystals. The white colored framboids are observed under the BSE, and the bright color reflects higher atom numbers than the surrounding elements (Goldstein et al. 1981). Pyrite may form early during burial of organic matter in sedimentary rocks where there is oxidation of organic matter with sulfate. Pyrite was observed in U5, U14 and U24, and can be seen in Figure 5.22. The photo is taken from U24.

Macrofossils (whole sponges specimens, crinoids, bryozoans and brachiopods) were observed in both U0 and U14 in field. The lack of macrofossils, excluding spicules, observed in thin sections is not expected. An explanation can be locally low fragmentation of macrofossils, or it can simply be due to locally lower concentration of fossils in the sampled rocks.

According to Ehrenberg et al. (2001) is the porosity in the bryozoan limestone only 0-5%. The dark spiculite is estimated to be 5-10%, where all pores are micropores. Both the bryozoan limestone and the dark spiculite have a low porosity. The light-colored spiculite has areas of high porosity (10-30%) that surrounds tight chert nodules of low porosity. This gives a varying permeability (Ehrenberg et al. 2001). The porosity measurements are all taken from wells on the Finnmark platform. Those measurements have not been compared with porosity estimated from image analysis of

thin sections from the present study. In as much as the epoxy that was used to impregnate the thin sections was not stained it proved difficult to distinguish between pores, calcite, dolomite and quartz. Porosity estimation of BSE images is possible when samples are impregnated with unstained epoxy, but this was not carried out in the present study due to time limitations.

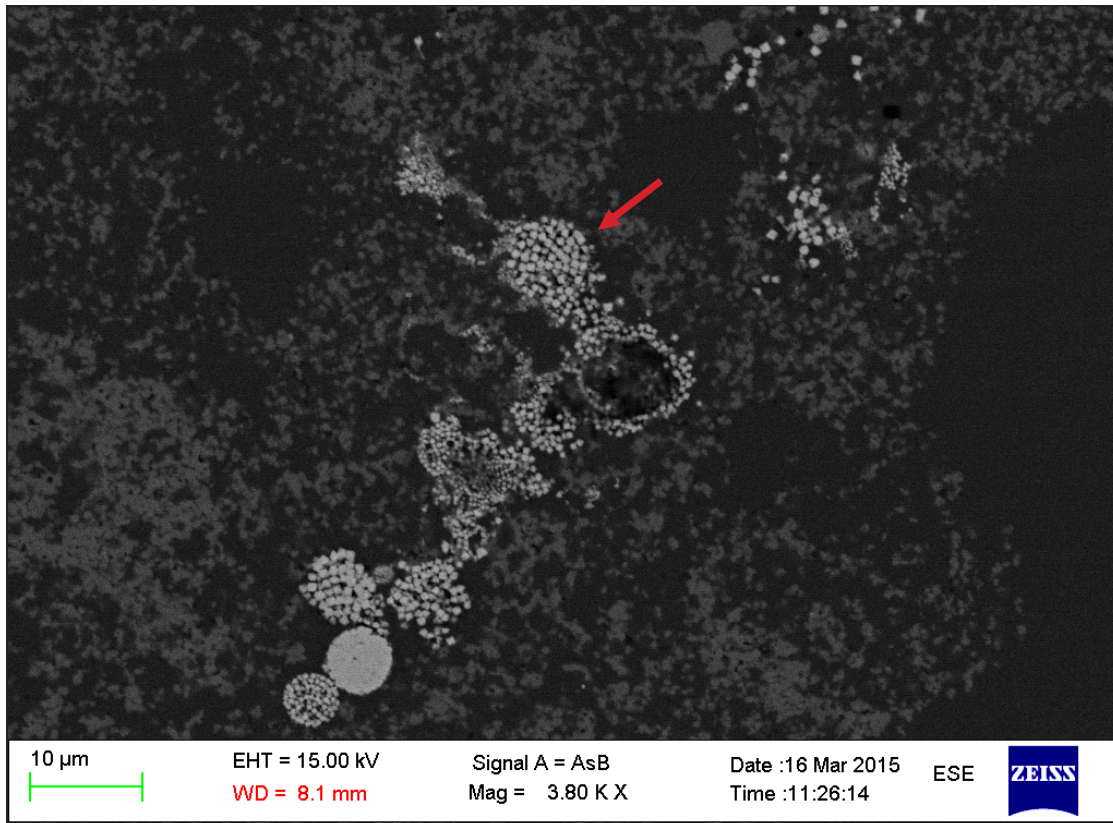


Figure 5. 22: Photo from SEM-studies displaying pyrite crystals in U24. Note the small framboids that are typical of early diagenetic pyrite formation mediated by sulphate reducing bacteria (e.g. Raiswell 1982).

CHAPTER 6 STRUCTURAL ANALYSIS AND DISCUSSION

6.1 Introduction

Fracture systems in the Permian Kapp Starostin Formation of the Tertiary Fold and Thrust Belt of Spitsbergen, at the southern tip of Mediumfjellet north of Isfjorden have been studied to inform: (1) Deformation mechanisms in fold-thrust belts, and (2) fractured reservoirs and their characteristics

Key aspects of this study are:

- How is the pattern and evolution of the investigated fractures, and how do they link to lithologies with general characteristics?
- How do the small-scale deformation relate to the fold-thrust belt?
- Can fractures be connected to layer parallel shortening and dilation during cataclastic flow?
- Are the mapped fractures important for fluid flow, and how can these data be used as an analogue for fractured reservoirs in fold-thrust belts?

A summary of the key results from Chapter 5 will be given first, as a short and informative background for the ensuing discussion.

6.2 Summary of fracture distribution and characteristics

This chapter analyzes and interprets the results described in Chapters 4 and 5. The key observations are:

- The Mediumfjellet thrust stack is on a macro-scale comprised of three in-sequence thrusts (M1, M2 and M3), and one out-of-sequence thrust (G).
- The total layer parallel shortening, parallel to tectonic transport in the Mediumfjellet thrust stack is estimated to be in the minimum range of 64 percent/m.
- The study area is in the southwestern part of the Mediumfjellet thrust stack, in a long, west-dipping section above the M3 thrust. In total eight fracture sets

are distinguished, with major fracture sets striking nearly E-W (sets 1 and 2) and NNW-SSE (sets 3 and 4).

- One lithology within the Permian Gipshuken Formation (dolomite), and five lithologies within the Permian Kapp Starostin Formation (brachiopod limestone, bryozoan limestone, dark spiculite, light-colored spiculite and shale) have been analyzed for fracturing.
- The highest fracture frequency occurs in the bryozoan limestone. However, the spiculitic beds are locally highly fractured. The Gipshuken Formation dolomite has the second highest fracture frequency in total. On the contrary, the brachiopod limestone of the Vøringen Member has the lowest fracture frequency, both compared with the other carbonate rocks and in total.
- Fracture analysis suggests a trend giving a generally higher fracture frequency in thinner beds than thicker beds; however, this trend is weakly expressed. The bryozoan limestone confirms this trend, though diffuse, while the dark spiculite do not display any higher fracture frequency for thinner beds.

Fracture characteristics are described separately for the different lithologies in the study area. The parameters are: orientations, type, fill and terminations. Table 6.1 summarizes the fracture characteristics of the different lithologies, which are described in more detail in Chapter 5.

Table 6. 1: Table summarizing the main properties of the fractures measured in the different lithologies. CP: calcite precipitation, TG: through-going fractures, BC: bed-confined fractures.

Lithology	Major orientation	Fracture sets	Dominant fracture type	Fill	Termination
Dolomite	Nearly E-W	1 + 2	Tension fractures	CP	TG, BC
Brachiopod limestone	Nearly E-W and NW-SE	1 + 2 + 5	Tension fractures	CP	TG, BC
Bryozoan limestone	NNW-SSE and NE-SW	3 + 6	Tension fractures	CP	TG, BC
Dark spiculite	Nearly E-W and NNW-SSE	1 + 2 + 3	Tension fractures	CP	TG, BC
Light-colored spiculite	NW-SE, NNW-SSE and NNE-SSW	4 + 5 + 7	Tension fractures	CP	TG, BC
Shale	Nearly E-W and NNW-SSE	1 + 3	Tension fractures	No fill	TG, BC

6.3 Large-scale structures and their lateral variability

Tectonic influence as for instance outlined by Fischer and Wilkerson (2000), is obviously important when looking at the fracture development in the study area. In addition to the four main thrusts, a fairly major thrust is observed in the north (cross-section A-A' and B-B'; Figure 5.2) cutting the backlimb of the M2-thrust anticline. There, a part of the M2 anticline backlimb is moved up towards the anticline hinge. Because of its cutting relationship to the anticline, this thrust is suggested to be younger with an out-of-sequence status. Similar observations was made by Larsen (2009), suggesting a displacement of ~20 m. The geometry of the M2 anticline is also changing along strike, with a stronger fault-propagation character southwards and a more open geometry northwards, which suggests an increase in shortening towards the south. In the mountainside of cross-section B-B', folded Permian beds with overlying Triassic strata are observed in the hangingwall of M2. The Permian folded beds stop abruptly towards the east. In this case it is suggested that the Permian beds are thrust up by a small eastern thrust (M2 upper splay). The beds get covered

toward the west but are likely cut by a larger thrust structurally below the M3-thrust, which is observed higher up in the mountainside. The folded Permian strata have not been described in earlier work, and the new observation makes the hangingwall of M2 prone to more deformation than earlier suggested in publications of e.g. Bergh and Andresen (1990) and Larsen (2009).

The M3 thrust sheet has by earlier workers (e.g. Bergh and Andresen 1990), been interpreted to be fault-bend-folded; the lateral variations (N-S) of the M3 thrust indicate a changing thrust ramp. According to Wennberg (1994) and Bergh et al. (1997) the transport direction is estimated to have been $\sim 070^\circ$. Based on this estimation it is suggested that the M3 thrust have mostly oblique to frontal ramps. The type of ramps in Mediumfjellet is discussed in Larsen (2009), where oblique ramps or ridges are suggested, giving a similar result. Larsen (2009) also suggested the possibility of a ridge and furrow appearance along the thrust surface of M3 (Chapter 3.2.2).

6.4 Fractures related to the fold-thrust belt

The measured fractures are from the hangingwall flat above the M3-thrust, located at the southern front of Mediumfjellet. The dominating fracture orientations in the study area are i) nearly E-W (sets 1 and 2) and ii) NNW-SSE (sets 3 and 4) (Figure 5.9), as explained in section 5.5. However iii) NW-SE (set 5), iv) NE-SW to NNE-SSW (sets 6 and 7) and v) nearly N-S (set 8) fractures are also of importance. The fractures do have a generally steep angle to the bedding, ranging from $50-90^\circ$. As the structural position is that of a flat over the M3 thrust, the succession of rock have most likely been transported above the basal detachment zone, passing a fixed-hinge syncline set up by the M1-M2 thrust system. According to Bergh and Andresen is the Mediumfjellet thrust stack also a piggyback sequence (see Chapter 3.2.1), and the succession will then have experienced some rotation.

The major fracture sets, making up $\sim 44\%$ of all measured fractures, are sets 1 and 2. Similar fracture sets striking nearly E-W are observed in Mediumfjellet by Larsen (2009). They are found mostly in the backlimb of thrust anticlines. After the classification of Hancock (1985), sets 1 and 2 cause extension in the ac plane (see Chapter 3.4).

These fracture sets are interpreted to be joints, as few slip lineations has been observed in field. These joints are steeply dipping fractures. It is suggested they are mainly foreland failure fractures, or so-called “indenter joints”, forming parallel to the highest horizontal stress axis (σ_H) at an early stage and in front of the developing FT-Belt, following the analysis of Engelder and Geiser (1980) (see Figure 6.1). The indenter joints cause a nearly E-W shortening and a nearly N-S directed extension in the Mediumfjellet mountain chain. This elongation is estimated in Chapter 6.6.1 to be in order of 0.002 percent/m.

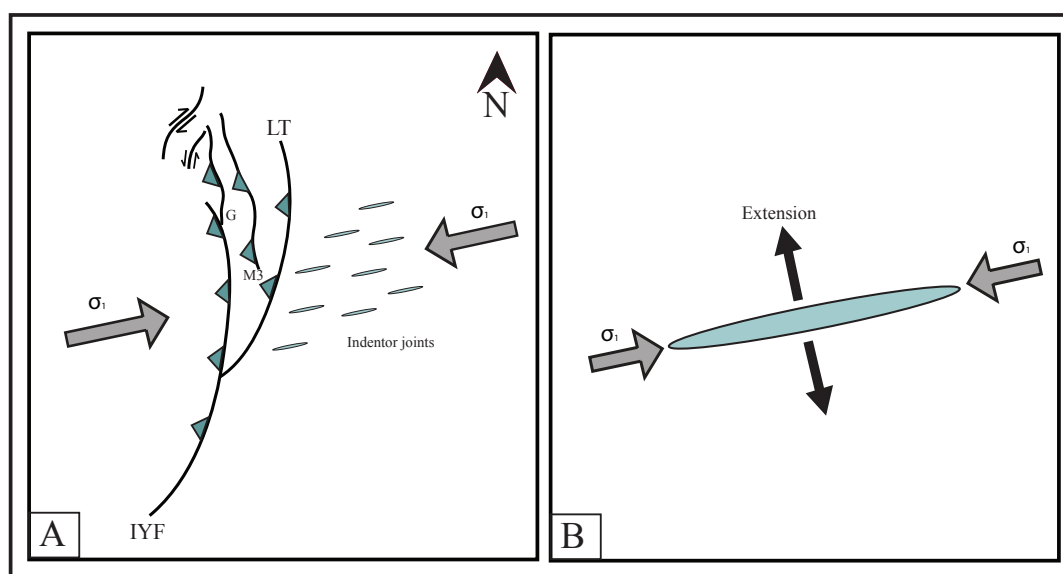


Figure 6. 1: **A)** A NE-SW to E-W oriented shortening, related to the main thrusts in the Mediumfjellet area, with fractures striking (indenter joints) parallel to σ_1 (σ_H). IYF – Isfjorden-Ymerbukta Fault, LT – Lappedalen thrust. Modified from Braathen et al. (1999). **B)** Illustration on how joints leads to extension perpendicular to the σ_1 (σ_H) and parallel to σ_3 (σ_h) in a compressional regime (elasto-brittle shortening).

Set 3 represents the third major fracture set. Accompanied by set 4, they form fractures striking NNW-SSE (see Figure 6.2). Similar fracture sets striking NNW-SSE is recorded by Larsen (2009), in the backlimb of the macroscopic anticlines. After the classification of Hancock (1985), the fractures cause extension in the bc plane (see Chapter 3.4). These fractures are interpreted to be joints striking nearly perpendicular to the main transport direction and the fractures of set 1 and 2. There is two possible interpretations for their formation; (i) joints forming parallel to the fixed syncline, as it pass the hinge zone, or (ii) joints forming due to the curvature of the ramp geometry. Either way they are formed due to layer parallel shortening, and will counteract the shortening in a nearly E-W direction.

Fractures oriented NW-SE (sets 5) and NE-SW (sets 6 and 7), can be interpreted as conjugate $hk0$ fractures, having an acute angle to a , and can be seen as shear fractures (see Chapter 3.4; Figure 6.2; Hancock 1985). This interpretation is based on the fractures orientation and the slip lineations found in fractures with an orientation similar to set 7. Larsen (2009) divided fractures striking between NE-SW and E-W into one set, and fractures striking between N-S and NE-SW into another set. These fractures were all together interpreted to be $hk0$ fractures, occurring frequently in the backlimb. These observations conform to fracture systems observed in this thesis.

The fractures trending nearly N-S (set 8) could be related to folding (joints), as it runs nearly parallel to the macroscopic fold axis (Figure 6.2). However, the fractures strike parallel to the Billefjorden-Lomfjorden lineament (striking approximately N-S), and are instead interpreted to relate to this structure.

Joints exhibiting symmetry with the fold axis is commonly interpreted to be of syn-folding origin (Hancock 1985), whereas joints with an orientation parallel or normal to the fold axis, are interpreted to be related to layer parallel shortening. Fractures that form conjugated pairs where the acute bisector is perpendicular to the fold, is seen as shear fractures, formed during layer parallel shortening (Stearns and Friedman 1972, Hancock 1985, Fischer and Wilkerson 2000).

The fracture sets collected for this thesis are, as described above, similar to the fracture sets observed by Larsen (2009), especially in the backlimb of the major folds of Mediumfjellet. It is also possible to relate them to the classification of fractures in a fold by Hancock (1985). This means that even though the fractures are collected from apparently unfolded strata above a thrust flat, they are likely influenced by the same stresses driving the deformation system overall, similar fracture networks can be observed in the less strained backlimb of a fold and in the intensely folded part. This arguments the importance of layer parallel shortening.

It is important to notice that these fracture data is based on scanlines were the majority are measured parallel to the N-S striking bedding as controlled by the nature of the outcrop (only eight short scanlines are dip parallel). This means that low-angled shear fractures have been difficult to observe, and accordingly are suppressed in the database.

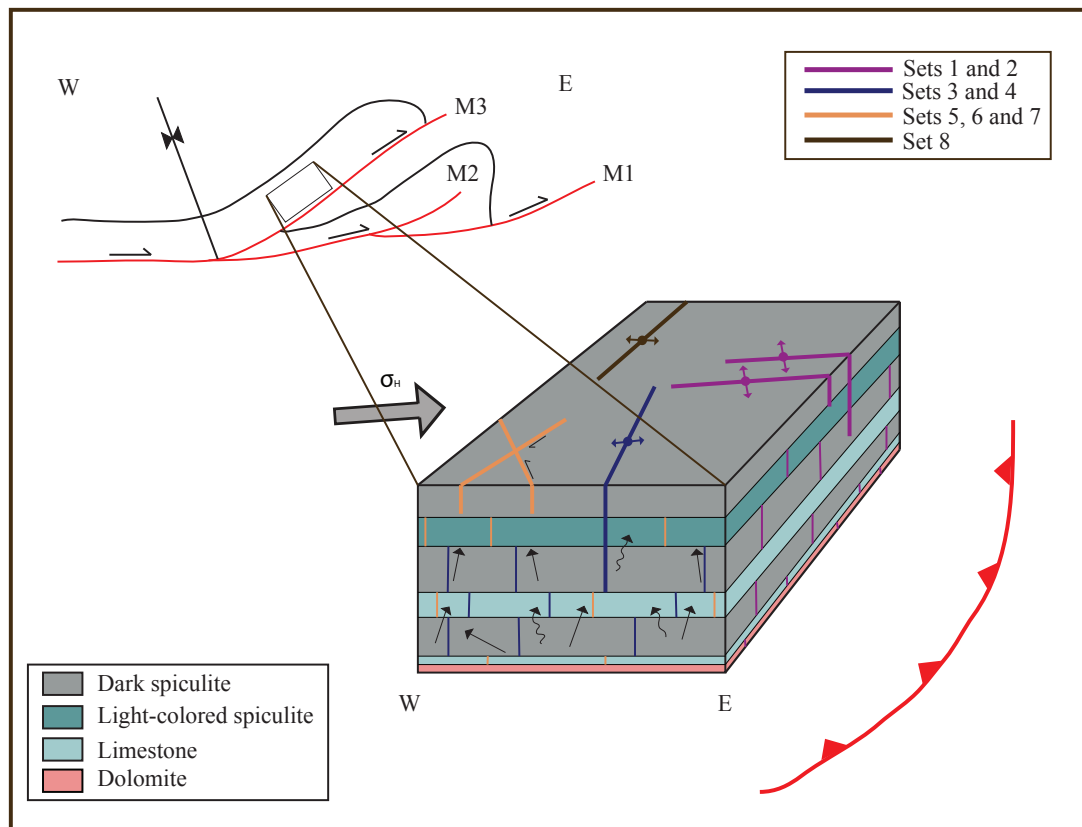


Figure 6. 2: Schematic box model of structural location and fracture systems in the studied thrust flat. Sets 1 and 2 are striking close to parallel to σ_1 , and interpreted to be joints. While sets 3 and 4 are interpreted to be joints, striking perpendicular to the transport direction. Sets 5-7 are seen as shear fractures striking NW-SE to NNW-SSE and NE-SW. Set 8, striking nearly N-S, is interpreted to be fractures related to the Billefjorden-Lomfjorden lineament. Note that the colored arrows on the joints sets, display the direction of extension caused by the joint set. The black arrows illustrate possible fluid pathways. Most fractures are steeply dipping, leading to vertical connectivity, where the porosity is seen to be highest in the bryozoan limestone, while the dark spiculite has the best permeability (see discussion in Chapter 6.7).

6.5 Fracture systems in a lithostratigraphic framework

Comparison of fracture frequency of the different lithologies in the study area shows that the fracture frequency fluctuates between the different lithologies (see Chapter 5.6.4). This trend fits with findings of Hugman and Friedman (1979), who showed that a dominant factor for fracturing was the effect of the texture or grain size. The results give a higher fracture frequency for bryozoan limestones than for the dominating spiculitic lithology (see Figure 6.3). As earlier mentioned, the spiculitic beds are sometimes so fractured at the surface; it is hard to measure the orientation of single fractures. Based on this observation and the related uncertainty around the importance of surface processes, the fracture frequency for dark spiculite can be higher than what the results display. The dolomite and the shale have a similar

fracture frequency, as does the brachiopod limestone and the light-colored spiculite. However, these four lithologies have only one to three scanlines recorded for each lithology, which limit the possibility of comparison. The varying fracture frequency between the different lithologies is suggested to be the result of varying mechanical properties. Factors controlling these properties should be a result of; i) bed thickness, ii) lithology, iii) diagenetic history, or iv) all the previous combined.

Earlier work (e.g. Ladeira and Price 1981, Huang and Angelier 1989, Underwood et al. 2003, Cook et al. 2006, Wennberg et al. 2006) suggests that the fracture frequency is controlled by bed thickness and lithologies of different mechanical properties. For this analysis, the reader is referenced to the mechanical stratigraphy of Chapter 4 (Figure 4.3). According to Ladeira and Price (1981) it is common that the fracture frequency is almost proportional to the bed thickness, with higher fracture frequencies in thinner beds. The overall fracture frequency compared with bed thickness in this study shows, however, no clear trend (Figure 5.17). A diffuse trend of higher fracture frequency within thinner beds might be present, but this is discussable. As a comparison, Wennberg et al. (2006) could not find any clear correlation between the fracture frequency and the bed thickness. Accordingly, they reached a similar conclusion as this study.

For two units, bryozoan limestone and dark spiculite, there could be a trend. The bryozoan limestone has a slightly higher fracture frequency in thinner beds that hints at a trend. On the contrary, the spiculitic beds, which are generally thicker than the beds in bryozoan limestone, do not show the suggested trend (Figure 5.18).

Layered rocks with weak intercalating bedding interfaces are characterized by BC fractures, while the stronger bed boundaries normally have higher probabilities for TG fractures (Cooke and Underwood 2001).

Scanlines measured in units with intercalating thin layers of mud between the beds show an average/m that is higher for BC than TG fractures as shown in Table 6.2. However, scanlines measured in sections without shale interlayers, suggesting stronger bed interfaces, have even higher average/m of BC than TG fractures (Table 6.2). This study shows no correlation between intercalating weak layers and BC fractures, as the BC fractures are even more common where there is strong bed interfaces, and do not support the results made by Cooke and Underwood (2001).

Table 6. 2: Average fractures/m of BC (bed-confined) and TG (through-going) fractures. BC fractures are more common both in strata with weak layers between the beds, and stronger bed interfaces. The results also display that there is a higher amount of BC fractures, than TG fractures in the studied mountain ridge.

Bed interfaces	BC (fractures/m)	TG (fractures/m)
Weak	1.09	0.71
Strong	1.47	0.60

Tectonic thrusting and folding may not be the only reason for macro-scale deformation. Rocks of the Mediumfjellet thrust stack is highly silicified due to its spicules, and thin section studies reveal that several units contain microcrystalline silica. When the temperature rises in a clastic sedimentary basin, prone to burial, thermochemical processes occur. The siliceous ooze heats and compacts, as it converts from opal A to opal CT, and results in compaction and lowering of the porosity. The end result is fracturing and faulting at a km-scale (see Chapter 3.3.2), through a process that may have formed during early burial of the sediments (Hein et al. 1978, Bohrmann et al. 1994, Davies 2005). This is especially relevant for the highly silicified dark spiculitic units with undulating bedding, which has closely spaced, bed-confined fractures (especially unit 2 and 6; Figure 4.3). Many of these fractures are interpreted to be diagenetic fractures (see Chapter 3.3.3). This process is also discussed in Larsen (2009) from her studies of the fractures in Mediumfjellet massive further north.

At microscale there were observed fractures in almost all thin sections. These fractures were filled with quartz and/or calcite/dolomite. Dolomitization can also be a reason for fracturing, because the process creates a volume reduction of 13% (see Chapter 3.3.2) (Weyl 1960). According to Wierzbicki et al. (2006), dolomite is more brittle than calcite, and will accordingly fracture more easily. This cannot be verified in this study, as the bryozoan limestone has the highest fracture frequency among the carbonates. However, the limestones in the Kapp Starostin Formation are strongly influenced by spicules giving a high Si-content. These rocks may not be representative for a classical limestone.

This study suggests that the fracture frequency is controlled by lithology and diagenetic processes, while the bed thickness is of minor importance. The highest fracture frequency is found in the bryozoan limestone, which is observed to be strong rocks, resistant towards erosion (Figure 4.3). This is supported by studies of Nelson (2001), who suggests that stronger and more brittle rocks have a higher fracture frequency. The bryozoan limestone is rich in fossils, changing between mudstone, wackestone, floatstone and rudstone through the formation. According to Gross (1993), tensile stress is concentrated around fossils, and make fractures form more easily here than elsewhere (see Chapter 3.3.4). This could partly explain the high fracture frequency.

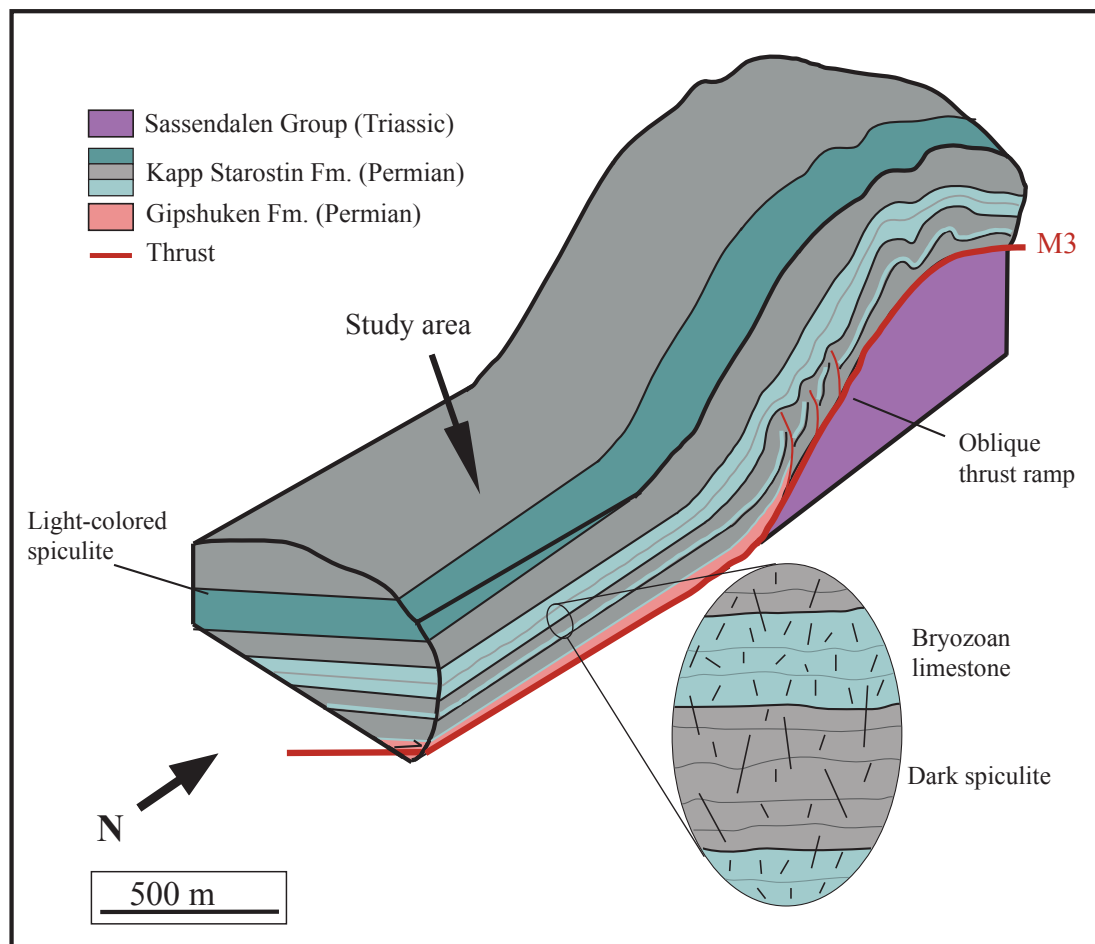


Figure 6. 3: Schematic three-dimensional block diagram of the study area, showing variations in fracture frequency for bryozoan limestone and dark spiculite in the Kapp Starostin Formation. Highest fracture frequency is observed to be in the bryozoan limestone. However, there is more through-going fractures present in the dark spiculite, than what is present in the bryozoan limestone.

6.6 Strain by cataclastic flow

6.6.1 Mesoscopic deformation

By using Lidarscan, the amount of mesoscopic shortening in the area has been estimated; for backlimb, hinge zone and forelimb of major thrust with related folds. The lowest rate of shortening is found to be in the backlimb, 11 percent/m, while the hinge zone has shortened the most with 24 percent/m. Only one measurement was done for the forelimb, due to difficulties of following layers, and estimated to have a shortening of 18 percent/m.

By adding the average meso-scale shortening to the estimated macro- and micro-scale shortening, the total LPS in the Mediumfjellet area are estimated to be minimum 64 percent/m. However, there are several factors that might influence the final result:

- The measured distances are not straight lines, but moving along the 3D model, and are therefore not giving the real distances. Projecting them onto the same plane should rectify some of the errors in the measured distances.
- Low and variable image resolution can hide smaller thrusts and smaller folds.
- The estimated micro-scale shortening is partly based on assumptions, covering subsurface and removed (by erosion) parts.

Shortening estimates have also been performed by earlier workers; Bergh and Andresen (1990) suggested the shortening in the Lappdalen-Mediumfjellet area to be 40%. Wennberg et al. (1994) came up with an estimation of 35% shortening in the Lappdalen area, while Bergh et al. (1997) suggested a shortening of 45% from east of Lappdalen to the Protektorfjellet thrust in the Western Zone of basement-involved thrusting. All the previous estimations are less than the shortening estimated in this thesis. However, this thesis includes the shortening at macro-, meso-, and micro-scale, compared to the previous papers that estimated shortening solely from the macro-scale cross-sections. The macro-scale shortening in this thesis has been estimated to be 49 percent/m, which is closer to previous estimations. The results are also expected to differ some, due to slightly different study areas.

The estimated micro-scale shortening is based on an assumed shortening by shear fractures of minimum 0.1 cm. This is, however, not a fully valuable assumption as slip lineations has been observed along only five fractures. Due to this observation, it

is suggested that most of the measured fractures are instead joints. Joints cause both elasto-brittle shortening along the fracture and extension perpendicular to the structure (Figure 6.1B). By assuming the average opening of a joint to be 0.1 cm, the LPE (layer parallel extension) will be 0.002 percent/m. This is based on that all fractures are instead joints, and will be a maximum estimation of extension. Segall and Pollard (1983) report on similar studies of a granodiorite in Sierra Nevada, suggesting joints to cause an elongation in the order of 10^{-4} (or 0.01%).

6.6.2 Sub-mesoscopic deformation (microscopic deformation)

The sub-mesoscopic or microscopic deformation is an important factor influencing the total deformation. With respect to folding and overall layer strain, brittle deformation at micro-scale might appear ductile at the meso- and macro-scale. An important part of this deformation is fracturing. When a rock fractures it causes strain in the rock and might lead to dilation. Extension creates joints, while compression causes shear fractures, stylolites and thrusts faults (see Chapter 3.3.3).

When measuring the fold shortening in box 1 (Chapter 5.3; Figure 5.5), at macro-scale in Lidarscan, the measured base of a bed in the fold has a higher rate of shortening than the top of the same bed. This suggests internal strain, and may reflect a fold mechanism ascribed to orthogonal flexure, where the outer part of the fold becomes stretched while the inner part is shortened. The major fracture network mapped in the field area indicates that the main deformation mechanism is flexural flow. According to Ismat and Mitra (2001) (see Chapter 3.4.1), a well-developed fracture network with blocks bounded by fractures indicates that there has been deformation by cataclastic flow. A blocky fracture system is present at Mediumfjellet, suggesting that the fracture network led to meso- and macro-scale folding by cataclastic flow seen as large-scale ductile deformation (Figure 6.4).

The Kapp Starostin Formation is comprised of lithologies with different mechanical properties, resulting in different fracture sets, divided into LSU (see Figure 5.11).

Brittle layers with interbedded thin weak layers will form minor faults along bedding, contributing to flexural slip (Shaw et al. 2005). In this thesis it is, however, observed that most brittle layers are characterized by frictional flow on fractures, instead of flexural slip along layers. This results in cataclastic flow, meaning that it is the brittle layers that are acting most ductile at a large scale.

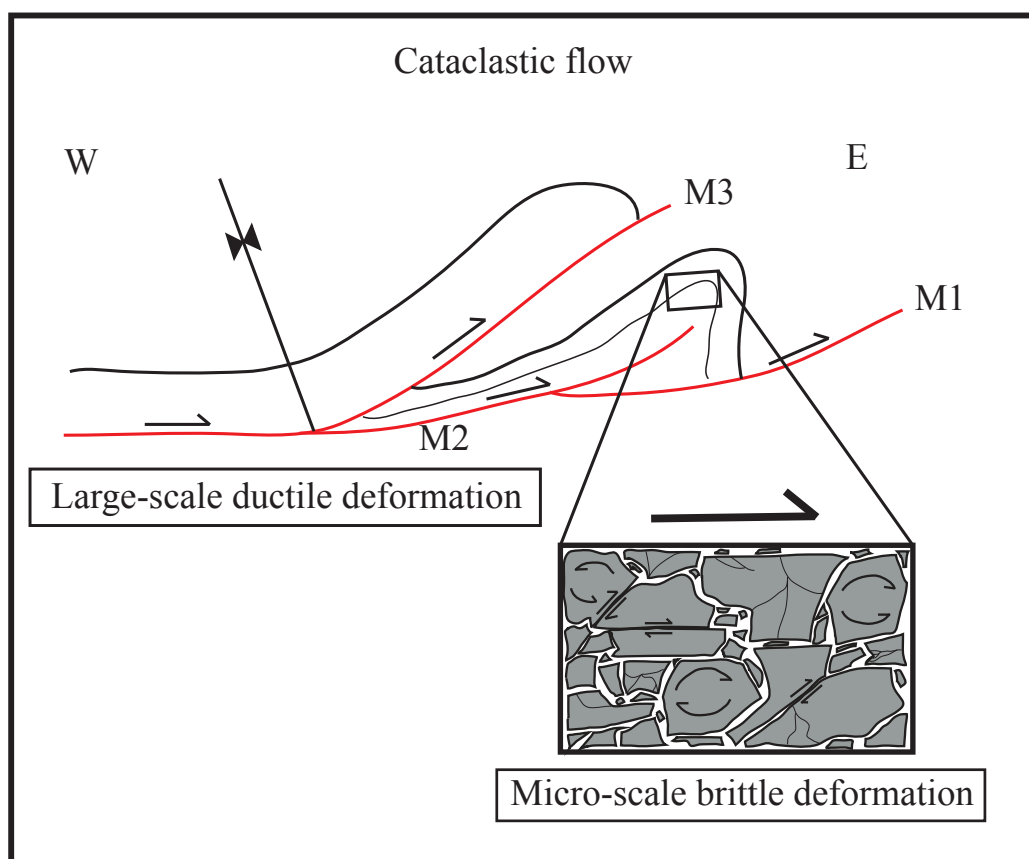


Figure 6. 4: Illustration of how brittle deformation at micro-scale seems ductile at meso- and macro-scale, due to cataclastic flow. This deformation mechanism includes micro-scale fracturing, rotation and frictional sliding of the grains.

Fractures have previously been described in relation to folding, forming as a result of folding. However, layer parallel shortening (LPS) results in thickening of beds and fracturing. This thesis observes that there are similar fracture networks in both folded and unfolded strata. Based on these results, it is suggested that folding is not the controlling factor for LPS. Instead, LPS is suggested to form first, being a prerequisite for folding, suggesting instead that the local LPS controls the large-scale folding.

6.7 Possible fluid flow and similar fracture reservoirs

This section discusses possible fluid flow pathways in the Kapp Starostin Formation, offering an analogue to a fractured reservoir, which is one of the aims of this thesis. Similar FT-Belts (Zagros and the South-Pyrenees) will also be mentioned for comparison.

Fracture data from this study give a higher amount of bed-confined (~67%) fractures than through-going fractures (~33%), with most TG fractures in the dark spiculite. This is further argued by the strength of bedding interfaces, as shown in Chapter 6.5. Both BC and TG fractures are observed to have calcite precipitation, and quartz-filled fractures are observed at microscale. Tension fractures (joints) are seen to be the dominating type of fractures; however, shear fractures are present as low-angled to bedding structures and some conjugate sets. Stylolite has been observed in dolomite and brachiopod limestone at outcrop-scale and in thin sections of dark spiculite.

Based on earlier work (Ehrenberg et al. 2001) the matrix in the Kapp Starostin Formation has an average low porosity and permeability due to secondary mineralogy filling pore spaces (both the spiculitic beds and the more carbonate-rich beds). The possibility for fluid flow in such tight lithologies is then highly depended on the fracture systems (e.g., Odling 1992, Aydin 2000, Odling et al. 2004). The connectivity between vertical open fractures and the fracture length is an important factor when discussing horizontal fluid migration (Odling et al. 1999). As mentioned in Chapter 3.5, major through-going fractures are important to fluid flow, while the shorter fractures mainly contribute to the porosity (Tsang 1984, Odling et al. 1999, Cooke et al. 2006). This is especially important for rocks with a low primary porosity and permeability as for instance the rocks present in the Kapp Starostin Formation.

Aydin (2000) suggests three types of structures that affect the properties of fluid flow; i) shear fractures (faults), ii) fractures (joints, veins and dikes), iii) compaction structures (solution seams and compaction bands). The fractures normally contribute to the fluid flow, while compaction structures act as barriers.

In the paper by Ogata et al. (2014) it is suggested that calcite and quartz precipitated in carbonate and siliciclastic beds, relate to diagenesis. These diagenetic horizons can contain intervals with sealed fractures leading to a baffled connectivity, and may cause a vertical compartmentalization of the reservoir unit. They also suggest that the fractures sealed by elastic strain relatively easily can be opened when subjected to small pressure increments (see Chapter 3.5).

Due to the Kapp Starostin Formation's suggested low porosity, the succession fits a Type-I reservoir after the classification system of Nelson (2001) (see Chapter 3.5).

The potential for being a carrier or reservoir rock has been considered for all stratigraphical layers. Overall, high percentage of bed-confined fractures gives a good

permeability, while the through-going fractures provides contact between the beds. The brachiopod limestone has the highest fracture frequency of the measured lithologies, and is then seen to be the best reservoir unit. It is, however, the dark spiculite that has most TG fractures and makes up major parts of the succession. According to Wennberg et al. (2006), beds with the smallest storage capacity and poorest contact between the matrix system and fracture system give the most effective transport system. Since the dark spiculite beds have a higher amount of TG fractures and lower fracture frequency, which most likely gives a lower porosity than the bryozoan limestone, they could work as good conduits for transporting the fluids into the bryozoan limestones (see Figure 6.2 for suggested fluid flow pathways).

In both the Zagros and the South-Pyrenees, there are producing fractured reservoirs in the FT-Belts (Fard et al. 2006, Wennberg et al. 2006, Ahmadhadi et al. 2007, Rudkiewicz et al. 2007, Shackleton et al. 2011). The detachment zone of the Zagros FT-Belt cuts through weak layers such as salt. The Early Cambrian Hormuz Salt represents the basal detachment of this FT-Belt, with major thrust splays creating fault-propagation folds. The Mid-Miocene Gachsaran Formation is another shallower but important detachment zone, with additional in-sequence and out-of-sequence thrusting (Fard et al. 2006). Multilevel detachments and fault-propagation folds mimic observations of the Mediumfjellet mountain range.

In a study of fractured folds in the Zagros FT-Belt, Wennberg et al. (2006) determined the major fractures to have a steep angle to bedding, be bed-confined and parallel to the fold axis. As previously described, the fractures in this study are observed to have a steep angle to bedding, where the majority of fractures are bed-confined. The major fracture sets are striking parallel (sets 1 and 2) and perpendicular (sets 3 and 4) to the transport direction (σ_H). The fractures striking perpendicular to the transport direction are oriented parallel to the major folds in the thrust stack. Based on these observations, Mediumfjellet thrust stack and the Zagros FT-Belt are suggested to have a similar fracture network.

The Pyrenees FT-Belt has two foreland basins (Aquitaine on the northern French side and Ebro basin on the southern Spanish side) as outlined in Travé et al. (2007). However, it has a similar detachment zone on both sides, following evaporitic beds, resulting in macroscale folds of the more rigid lithologies (Travé et al. 2007).

Fractures above the L'Escala Thrust have been studied by Travé et al. (2007), which according to Muñoz et al. (1986) is a part of the Alps-L'Escala hangingwall antiform, located within the south-eastern Pyrenean foreland basin. The studied fractures are divided into three sets: (1) pre-thrust extensional fractures, (2) thrust-related shear-fractures, (3) post-thrust fractures including sinistral strike-slip faults and NW-SE extensional fractures. Based on studies from the Southern Pyrenees, Travé et al. (2007) suggested that the fractures and faults could have a major control on the fluid distribution.

The studied fracture network in Mediumfjellet thrust stack does also show pre-thrust extensional fractures, created in the foreland of the FT-Belt (indentor joints). Further shear fractures and extensional fractures are related to the layer parallel shorting, suggesting similar fracture sets as studied in the Southern Pyrenees.

CHAPTER 7 CONCLUSION AND FUTURE WORK

7.1 Conclusions

This study addresses deformation characteristics and mechanisms in a fold-thrust belt, targeting, the highly silicified strata of the Kapp Starostin Formation of Spitsbergen's fold-thrust belt as an analogue to fractured reservoirs. Based on outcrop observations coupled with lidarscan analysis and thin sections studies, the following conclusion can be drawn:

- The Mediumfjellet fold-thrust stack consists of four major thrusts, termed M1, M2, M3 and G. A new observation is a macro-scale structure in the stack, where folded Permian strata relates to a major thrust-splay in the M2-thrust's hangingwall. This contributes to more shortening than earlier suggested.
- The dominating fracture orientations are i) nearly E-W, which is suggested to be indentor joints, and ii) NNW-SSE, suggested to be related to a fixed hinge syncline above a thrust ramp-flat bend, and/or the curvature of the ramp geometry. Fractures in apparently unfolded strata can be compared to fractures in folded strata.
- Fracture frequency is observed to be dependent on the lithology and their pseudo-mechanical properties, while no clear trend can be defined between fracture frequency and bed thickness. It is the bryozoan limestone that is seen to have the highest fracture frequency among the studied lithologies. Both layered rocks with weak intercalating bedding and rocks with strong interfaces are characterized by bed-confined fractures.
- Parts of the deformation are most likely linked to diagenetic fracturing when silica converts from opal A to opal CT. Calcite to dolomite reactions could also be of importance for some units.
- Lidarscan estimates of shortening in the Mediumfjellet mountain range suggests highest shortening in the hinge zone, summing to around 24

percent/m, while the backlimb has the least shortening with nearly 11 percent/m. The total Layer Parallel Shortening in Mediumfjellet is estimated to be 64 percent/m in an E-W direction, while the Layer Parallel Extension accounts for 0.002 percent/m in an N-S direction.

- Based on the well-developed blocky fracture system present in the studied rocks, the Mediumfjellet thrust stack has most likely experienced meso- and macro-scale folding by cataclastic flow. The cataclastic flow is especially relevant for the more brittle layers, where frictional flow on fractures contributes to large-scale ductile deformation rather than layer parallel flexural slip. The results suggest that local layer parallel shortening controls large-scale folding.
- The high percentage (~67%) of bed-confined fractures gives a good porosity, while the through-going fractures ensure contact between fracture networks. The bryozoan limestone has the highest fracture frequency and is therefore seen as the best reservoir rock in the study area. The many similarities between Mediumfjellet and producing fractured reservoirs in fold-thrust belts suggests Mediumfjellet represents a viable analogue for fractured reservoirs in fold-thrust belts.

7.2 Future work

Svalbard has a dynamic landscape, as evident by the surging Wahlenbergreen in the field area covering more of the mountain ridge every year. While some outcrops get covered by for instance glaciers, new outcrops appear by glacial retreat. The folded Permian strata in the M2 hangingwall are a striking example. A renewed closer study on the folded Permian strata and its geometry along strike, including newly exposed outcrops will likely add new understanding to the Mediumfjellet thrust stack.

Even though 80% of the Kapp Starostin Formation is comprised of bryozoan limestone and dark spiculite, the other lithologies represent important contributors to the total deformation in the area. Studying those lithologies and especially collecting scanlines in dip-parallel section will add understanding of low-angle-to-bedding structures and thereby fracture development in the thrust front.

Further studies of fracture systems in the Permian Kapp Starostin Formation in the so-called undeformed foreland to the east would identify variability in fracture systems, and inform the discussion of more local folding mechanisms versus regional fracturing.

CHAPTER 8 REFERENCES

- Ahmadhadi, F., O. Lacombe, and J.-M. Daniel, 2007, Early reactivation of basement faults in Central Zagros (SW Iran): evidence from pre-folding fracture populations in Asmari Formation and lower Tertiary paleogeography, *Thrust Belts and Foreland Basins*, Springer, p. 205-228.
- Anell, I., A. Braathen, S. Olaussen, and P. Osmundsen, 2013, Evidence of faulting contradicts a quiescent northern Barents Shelf during the Triassic: first break, v. 31.
- Awdal, A. H., 2009, Fracture Analysis and Conceptual Model of the Shiranish Formation in Taq Taq Field, Kurdistan Region, NE Iraq. Master thesis, Dep. of Earth Science, University of Bergen, Bergen, Norway, p. 77-78.
- Aydin, A., 2000, Fractures, faults, and hydrocarbon entrapment, migration and flow: *Marine and Petroleum Geology*, v. 17, p. 797-814.
- Bergbauer, S., and D. D. Pollard, 2004, A new conceptual fold-fracture model including prefolding joints, based on the Emigrant Gap anticline, Wyoming: *Geological Society of America Bulletin*, v. 116, p. 294-307.
- Bergh, S., H. Maher, and A. Braathen, 2011, Late Devonian transpressional tectonics in Spitsbergen, Svalbard, and implications for basement uplift of the Sørkapp–Hornsund High: *Journal of the Geological Society*, v. 168, p. 441-456.
- Bergh, S. G., and A. Andresen, 1990, Structural development of the Tertiary fold - and - thrust belt in east Oscar II Land, Spitsbergen: *Polar Research*, v. 8, p. 217-236.
- Bergh, S. G., A. Braathen, and A. Andresen, 1997, Interaction of basement-involved and thin-skinned tectonism in the Tertiary fold-thrust belt of central Spitsbergen, Svalbard: *AAPG bulletin*, v. 81, p. 637-661.
- Bergh, S. G., Y. Otha, A. Andresen, H. D. Maher, A. Braathen, and W. K. Dallmann, 2003, Map: ST. JONSFJORDEN, Svalbard 1: 100 000: Norwegian Polar Institute, Theme map nr. 34.
- Birkenmajer, K., 1972, Tertiary history of Spitsbergen and continental drift: *Acta Geologica Polonica*, v. 22, p. 193-218.
- Birkenmajer, K., 1975, Caledonides of Svalbard and plate tectonics: *Bulletin of the Geological Society of Denmark*, v. 24, p. 1-19.
- Birkenmajer, K., 1981, The geology of Svalbard, the western part of the Barents Sea, and the continental margin of Scandinavia, *The Arctic Ocean*, Springer, p. 265-329.
- Birkenmajer, K., and T. Morawski, 1960, Dolerite intrusions of Wedel-Jarlsberg Land, Vestspitsbergen: *Studia Geologica Polonica*, v. 4, p. 103-123.
- Blinova, M., R. Thorsen, R. Mjelde, and J. I. Faleide, 2009, Structure and evolution of the Bellsund Graben between Forlandsundet and Bellsund (Spitsbergen) based on marine seismic data.: *Norw. J. Geol.*, 89 (3), p. 215-228.
- Blomeier, D., A. Dustira, H. Forke, and C. Scheibner, 2011, Environmental change in the Early Permian of NE Svalbard: from a warm-water carbonate

- platform (Gipshuken Formation) to a temperate, mixed siliciclastic-carbonate ramp (Kapp Starostin Formation): *Facies*, v. 57, p. 493-523.
- Blomeier, D., M. Wisshak, W. Dallmann, E. Volohonsky, and A. Freiwald, 2003, Facies analysis of the Old Red Sandstone of Spitsbergen (Wood Bay Formation): Reconstruction of the depositional environments and implications of basin development: *Facies*, v. 49, p. 151-174.
- Bohrmann, G., A. Abelman, R. Gersonde, H. Hubberten, and G. Kuhn, 1994, Pure siliceous ooze, a diagenetic environment for early chert formation: *Geology*, v. 22, p. 207-210.
- Boyer, S. E., and D. Elliott, 1982, Thrust systems: *AAPG Bulletin*, v. 66, p. 1196-1230.
- Braathen, A., and S. G. Bergh, 1995, Kinematics of Tertiary deformation in the basement-involved fold-thrust complex, western Nordenskiöld Land, Svalbard: tectonic implications based on fault-slip data analysis: *Tectonophysics*, v. 249, p. 1-29.
- Braathen, A., S. G. Bergh, and H. D. Maher, 1999, Application of a critical wedge taper model to the Tertiary transpressional fold-thrust belt on Spitsbergen, Svalbard: *Geological Society of America Bulletin*, v. 111, p. 1468-1485.
- Braathen, A., K. Bælum, H. Maher Jr, and S. J. Buckley, 2011, Growth of extensional faults and folds during deposition of an evaporite-dominated half-graben basin; the Carboniferous Billefjorden Trough, Svalbard: *Norwegian Journal of Geology*, v. 91, p. 137-161.
- Buckley, S., J. Vallet, A. Braathen, and W. Wheeler, 2008a, Oblique helicopter-based laser scanning for digital terrain modelling and visualisation of geological outcrops: *International Archives of the Photogrammetry, Remote Sensing and Spatial Information Sciences*, v. 37, p. 493-498.
- Buckley, S. J., J. Howell, H. Enge, and T. Kurz, 2008b, Terrestrial laser scanning in geology: data acquisition, processing and accuracy considerations: *Journal of the Geological Society*, v. 165, p. 625-638.
- Butler, R. W., 1982, The terminology of structures in thrust belts: *Journal of structural geology*, v. 4, p. 239-245.
- Bælum, K., and A. Braathen, 2012, Along-strike changes in fault array and rift basin geometry of the Carboniferous Billefjorden Trough, Svalbard, Norway: *Tectonophysics*, v. 546, p. 38-55.
- Cooke, M. L., J. Simo, C. A. Underwood, and P. Rijken, 2006, Mechanical stratigraphic controls on fracture patterns within carbonates and implications for groundwater flow: *Sedimentary Geology*, v. 184, p. 225-239.
- Cooke, M. L., and C. A. Underwood, 2001, Fracture termination and step-over at bedding interfaces due to frictional slip and interface opening: *Journal of Structural Geology*, v. 23, p. 223-238.
- Corfu, F., S. Polteau, S. Planke, J. I. Faleide, H. Svensen, A. Zayoncheck, and N. Stolbov, 2013, U-Pb geochronology of Cretaceous magmatism on Svalbard and Franz Josef Land, Barents Sea Large Igneous Province: *Geological Magazine*, v. 150, p. 1127-1135.
- Critelli, S., and W. E. Reed, 1999, Provenance and stratigraphy of the Devonian (old red sandstone) and Carboniferous sandstones of Spitsbergen, Svalbard: *European journal of mineralogy*, v. 11, p. 149-166.

- Cutbill, J., and A. Challinor, 1965, Revision of the stratigraphical scheme for the Carboniferous and Permian rocks of Spitsbergen and Bjørnøya: *Geol. Mag.*, v. 102, p. 418-439.
- Dallmann, W., A. Andersen, S. Bergh, and H. Maher Jr, 1993, Tertiary fold-and-thrust belt of Spitsbergen Svalbard: *Norsk Polarinstitutt Meddelelser*, v. 128, p. 5-46.
- Dallmann, W. K., H. Dypvik, J. Gjelberg, W. B. Harland, E. Johannessen, H. Keilen, G. Larssen, A. Lønøy, P. Midbøe, A. Mørk, J. Nagy, I. Nilsson, A. Nøttvedt, S. Olaussen, T. Pcelina, R. Steel, and D. Worsley, 1999, Lithostratigraphic lexicon of Svalbard: review and recommendations for nomenclature use: Upper Palaeozoic to Quaternary bedrock. Chapter 2 - Upper Paleozoic Lithostratigraphy, Norsk Polarinstitutt.
- Davies, R. J., 2005, Differential compaction and subsidence in sedimentary basins due to silica diagenesis: A case study: *Geological Society of America Bulletin*, v. 117, p. 1146-1155.
- Dershowitz, W. S., and H. H. Herda, 1992, Interpretation of fracture spacing and intensity: The 33th US Symposium on Rock Mechanics (USRMS).
- Doblas, M., 1998, Slickenside kinematic indicators: *Tectonophysics*, v. 295, p. 187-197.
- Donath, F. A., and R. B. Parker, 1964, Folds and folding: *Geological Society of America Bulletin*, v. 75, p. 45-62.
- Dravis, J. J., 1980, Sedimentology and diagenesis of the Upper Cretaceous Austin Chalk Formation, south Texas and northern Mexico: Ph. D thesis, Rice University, Huston, Texas, p. 513.
- Dunham, R. J., 1962, Classification of carbonate rocks according to depositional texture. In Ham, W. E. (ed.): *Classification of Carbonate Rocks: AAPG Memoir*, v. 1, p. 108-121.
- Ehrenberg, S., E. B. Nielsen, T. A. Svånå, and L. Stemmerik, 1998, Diagenesis and reservoir quality of the Finnmark carbonate platform, Barents Sea: results from wells 7128/6-1 and 7128/4-1: *Norsk geologisk tidsskrift*, v. 78, p. 225-251.
- Ehrenberg, S., N. Pickard, L. Henriksen, T. Svana, P. Gutteridge, and D. Macdonald, 2001, A depositional and sequence stratigraphic model for cold-water, spiculitic strata based on the Kapp Starostin Formation (Permian) of Spitsbergen and equivalent deposits from the Barents Sea: *AAPG bulletin*, v. 85, p. 2061-2088.
- Elvevold, S., W. Dallmann, and D. Blomeier, 2007, *Geology of Svalbard*, Norwegian Polar Institute.
- Embry, A. F., and J. E. Klovan, 1972, Absolute water depth limits of Late Devonian paleoecological zones: *Geologische Rundschau*, v. 61, p. 672-686.
- Engelder, T., and P. Geiser, 1980, On the use of regional joint sets as trajectories of paleostress fields during the development of the Appalachian Plateau, New York: *Journal of Geophysical Research: Solid Earth (1978-2012)*, v. 85, p. 6319-6341.
- Engelder, T., and A. Lacazette, 1990, Rock joints: Natural hydraulic fracturing: *AA Balkema*, Rotterdam, p. 35-44.
- Engen, Ø., J. I. Faleide, and T. K. Dyreng, 2008, Opening of the Fram Strait gateway: a review of plate tectonic constraints: *Tectonophysics*, v. 450, p. 51-69.

- Erslev, E. A., 1991, Trishear fault-propagation folding: *Geology*, v. 19, p. 617-620.
- Faleide, J., S. Gudlaugsson, O. Eldholm, A. Myhre, and H. Jackson, 1991, Deep seismic transects across the sheared western Barents Sea-Svalbard continental margin: *Tectonophysics*, v. 189, p. 73-89.
- Faleide, J. I., A. Myhre, and O. Eldholm, 1988, Early Tertiary volcanism at the western Barents Sea margin. In: *Early Tertiary Volcanism and the opening of the NE Atlantic* (Eds A. C. Morton and L. M. Parson): *Spec. Publ. Geol. Soc. Lond.*, v. 39, p. 135-146.
- Faleide, J. I., F. Tsikalas, A. J. Breivik, R. Mjelde, O. Ritzmann, O. Engen, J. Wilson, and O. Eldholm, 2008, Structure and evolution of the continental margin off Norway and the Barents Sea: *Episodes*, v. 31, p. 82.
- Faleide, J. I., E. Vågnes, and S. T. Gudlaugsson, 1993, Late Mesozoic-Cenozoic evolution of the south-western Barents Sea in a regional rift-shear tectonic setting: *Marine and Petroleum Geology*, v. 10, p. 186-214.
- Fard, I. A., A. Braathen, M. Mokhtari, and S. A. Alavi, 2006, Interaction of the Zagros Fold-Thrust Belt and the Arabian-type, deep-seated folds in the Abadan Plain and the Dezful Embayment, SW Iran: *Petroleum Geoscience*, v. 12, p. 347-362.
- Fischer, M. P., and M. S. Wilkerson, 2000, Predicting the orientation of joints from fold shape: Results of pseudo-three-dimensional modeling and curvature analysis: *Geology*, v. 28, p. 15-18.
- Fredriksen, K. R., 1988, Sedimentologiske og diagenetiske undersøkelser av Kapp Starostinformasjonen på Akseløya og Mariaholmen, Bellsund, Svalbard. *Candidatus Scientiarum thesis*, Department of Geology, Tromsø University, Norway, p. 286.
- Friedman, M., O. Kwon, and V. L. French, 1994, Containment of natural fractures in brittle beds of the Austin Chalk, rock mechanics, models and measurements challenges from industry.: *Proceedings of the 1st North American Rock Mechanics Symposium*, p. 833-840.
- Friend, P. F., B. Williams, M. Ford, and E. Williams, 2000, Kinematics and dynamics of Old Red Sandstone basins: *Geological Society, London, Special Publications*, v. 180, p. 29-60.
- Gabrielsen, R., R. Færseth, L. Jensen, J. Kalheim, and F. Riis, 1990, Structural elements of the Norwegian continental shelf: *NPD-Bulletin*, v. 6, p. 5-26.
- Gabrielsen, R., O. Kløvjan, H. Haugsbø, P. Midbøe, A. Nøttvedt, E. Rasmussen, and P. Skott, 1992, A structural outline of Forlandsundet Graben, Prins Karls Forland, Svalbard: *Norsk geologisk tidsskrift*, v. 72, p. 105-120.
- Gaina, C., L. Gernigon, and P. Ball, 2009, Palaeocene–Recent plate boundaries in the NE Atlantic and the formation of the Jan Mayen microcontinent: *Journal of the Geological Society*, v. 166, p. 601-616.
- Gayer, R. A., D. G. Gee, T. S. Winsnes, W. B. Harland, R. H. Wallis, J. A. Miller, and H. R. Spall, 1966, Radiometric age determinations on rocks from Spitsbergen: *Norwegian Polar Institute*, v. 137, p. 4-39.
- Gjelberg, J., and R. Steel, 1981, An outline of Lower-Middle Carboniferous sedimentation on Svalbard: Effects of tectonic, climatic and sea level changes in rift basin sequences: *Geology of the North Atlantic Borderlands - Memoir 7*, p. 543-561.

- Goffey, G. P., J. Craig, T. Needham, and R. Scott, 2010, Fold–thrust belts: overlooked provinces or justifiably avoided?: Geological Society, London, Special Publications, v. 348, p. 1-6.
- Goldstein, J. I., D. E. Newbury, P. Echlin, D. C. Joy, C. Fiori, and E. Lifshin, 1981, Scanning electron microscopy and X-ray microanalysis. A text for biologists, materials scientists, and geologists, Plenum Publishing Corporation.
- Grabowski, G. J., 1984, Generation and migration of hydrocarbons in Upper Cretaceous Austin Chalk, south-central Texas, in J. G. Palacas, ed., Petroleum geochemistry and source rock potential of carbonate rocks: AAPG Studies in Geology, v. 18, p. 97-125.
- Gradstein, F. M., J. G. Ogg, and A. G. Smith, 2004, A geologic time scale 2004, v. 86, Cambridge University Press.
- Groshong, R., 1975, Strain, fractures, and pressure solution in natural single-layer folds: Geological Society of America Bulletin, v. 86, p. 1363-1376.
- Gross, M. R., 1993, The origin and spacing of cross joints: examples from the Monterey Formation, Santa Barbara Coastline, California: Journal of Structural Geology, v. 15, p. 737-751.
- Grundvåg, S.-A., 2008, Facies analysis, sequence stratigraphy and geochemistry of the middle-upper Permian Kapp Starostin Formation, central Spitsbergen: Unpublished Master thesis, Faculty of Science, University of Tromsø, Tromsø, Norway, 37-176 p.
- Hancock, P., 1985, Brittle microtectonics: principles and practice: Journal of structural geology, v. 7, p. 437-457.
- Haremo, P., A. Andresen, H. Dypvik, J. Nagy, A. Elverhøi, T. A. Eikeland, and H. Johansen, 1990, Structural development along the Billefjorden Fault Zone in the area between Kjellströmdalen and Adventdalen/Sassendalen, central Spitsbergen: Polar Research, v. 8, p. 195-216.
- Harland, W., 1965, The tectonic evolution of the Arctic-North Atlantic region: Philosophical Transactions of the Royal Society of London, Series B, v. 258, p. 59-75.
- Harland, W. B., 1969, Contribution of Spitsbergen to Understanding of Tectonic Evolution of North Atlantic Region: Chapter 58: Arctic Regions: AAPG Memoir, v. 12, p. 828-862.
- Harland, W. B., L. M. Anderson, D. Manasrah, N. J. Butterfield, A. Challinor, P. A. Doubleday, E. K. Dowdeswell, J. A. Dowdeswell, I. Geddes, and S. R. Kelly, 1997, The geology of Svalbard: Geological society Memoir No. 17, London.
- Hein, J. R., D. W. Scholl, J. A. Barron, M. G. Jones, and J. Miller, 1978, Diagenesis of late Cenozoic diatomaceous deposits and formation of the bottom simulating reflector in the southern Bering Sea: Sedimentology, v. 25, p. 155-181.
- Helland-Hansen, W., 1990, Sedimentation in Paleogene Foreland Basin, Spitsbergen (1): AAPG Bulletin, v. 74, p. 260-272.
- Helland-Hansen, W., 2010, Facies and stacking patterns of shelf-deltas within the Paleogene Battfjellet Formation, Nordenskiöld Land, Svalbard; implications for subsurface reservoir prediction.: Sedimentology, v. 57(1), p. 190-208.
- Henriksen, L., 1988, En sedimentologisk og diagenetisk undersøkelse av Kapp Starostinformasjonen på Akseløya og Mariaholmen, Svalbard. Candidatus

- Scintiarum thesis, Department of Geology, Tromsø University, Norway, p. 316.
- Holl, J. E., and D. J. Anastasio, 1995, Cleavage development within a foreland fold and thrust belt, southern Pyrenees, Spain: *Journal of Structural Geology*, v. 17, p. 357-369.
- Huang, Q., and J. Angelier, 1989, Fracture spacing and its relation to bed thickness: *Geological Magazine*, v. 126, p. 355-362.
- Hugman, R. H. H., and M. Friedman, 1979, Effects of texture and composition on mechanical behavior of experimentally deformed carbonate rocks: *AAPG Bulletin*, v. 63, p. 1478-1489.
- Irwin, G., 1957, Relation of stresses near a crack to the crack extension force: 9th Cong. App. Mech., Brussels.
- Ismat, Z., and G. Mitra, 2001, Folding by cataclastic flow at shallow crustal levels in the Canyon Range, Sevier orogenic belt, west-central Utah: *Journal of Structural Geology*, v. 23, p. 355-378.
- Jamison, W. R., 1987, Geometric analysis of fold development in overthrust terranes: *Journal of structural Geology*, v. 9, p. 207-219.
- Kastner, M., J. Keene, and J. Gieskes, 1977, Diagenesis of siliceous oozes—I. Chemical controls on the rate of opal-A to opal-CT transformation—an experimental study: *Geochimica et Cosmochimica Acta*, v. 41, p. 1041-1059.
- Kellogg, H. E., 1975, Tertiary stratigraphy and tectonism in Svalbard and continental drift: *AAPG Bulletin*, v. 59, p. 465-485.
- Kligfield, R., J. Crespi, S. Naruk, and G. H. Davies, 1984, Displacement and southern Appalachian Valley and Ridge and Plateau Provinces, West Virginia and Virginia: *AAPG Bulletin*, v. 70, p. 1674-1684.
- Ladeira, F., and N. Price, 1981, Relationship between fracture spacing and bed thickness: *Journal of Structural Geology*, v. 3, p. 179-183.
- Larsen, T., 2009, Fractured carbonates in the Mediumfjellet thrust-stack in the Tertiary fold-and-thrust belt of Spitsbergen: Unpublished Master thesis, University of Tromsø, Tromsø, Norway, p. 27-102.
- Lauritzen, Ø., 1983, Karstic surface in the Lower Permian sabkha sequence of the Gipshuken Formation, central Spitsbergen, Svalbard: *Polar Research*, v. 1, p. 157-160.
- Leever, K. A., R. H. Gabrielsen, J. I. Faleide, and A. Braathen, 2011, A transpressional origin for the West Spitsbergen fold - and - thrust belt: Insight from analog modeling: *Tectonics*, v. 30.
- Lind, I. L., 1993, Stylolites in chalk from Leg 130, Ontong Java Plateau, in W. H. Berger, L. W. Kroenke, and L. A. Mayer, eds.: *Proceedings of the Ocean Drilling Program, Scientific Results*, v. 13, p. 445-452.
- Lisle, R. J., and D. C. Srivastava, 2004, Test of the frictional reactivation theory for faults and validity of fault-slip analysis: *Geology*, v. 32, p. 569-572.
- Lowell, J. D., 1972, Spitsbergen Tertiary orogenic belt and the Spitsbergen fracture zone: *Geological Society of America Bulletin*, v. 83, p. 3091-3102.
- Lyberis, N., and G. Manby, 1993, The origin of the West Spitsbergen Fold Belt from geological constraints and plate kinematics: implications for the Arctic: *Tectonophysics*, v. 224, p. 371-391.
- Maher, H., S. Bergh, A. Braathen, G. Manby, and N. Lyberis, 2001, Discussion on pre-ocean opening compression of the Northwestern Atlantic margin:

- evidence from eastern Greenland *Journal*, Vol. 157, 2000, 707–710:
Journal of the Geological Society, v. 158, p. 728-730.
- Maher, H. D., S. Bergh, A. Braathen, and Y. Ohta, 1997, Svartfjella, Eidembukta, and Daudmannsodden lineament: Tertiary orogen - parallel motion in the crystalline hinterland of Spitsbergen's fold - thrust belt: *Tectonics*, v. 16, p. 88-106.
- Maher, H. D., A. Braathen, S. Bergh, W. Dallmann, and W. B. Harland, 1995, Tertiary or Cretaceous age for Spitsbergen's fold - thrust belt on the Barents Shelf: *Tectonics*, v. 14, p. 1321-1326.
- Maher, H. D., and C. Craddock, 1988, Decoupling as an alternate model for transpression during the initial opening of the Norwegian - Greenland Sea: *Polar Research*, v. 6, p. 137-140.
- Maher Jr, H. D., 2001, Manifestations of the Cretaceous High Arctic large igneous province in Svalbard: *The Journal of Geology*, v. 109, p. 91-104.
- Margat, J., and J. Van der Gun, 2013, *Groundwater around the world: a geographic synopsis*, CRC Press, London, UK, p. 35-64.
- McCann, A. J., and W. K. Dallmann, 1996, Reactivation history of the long-lived Billefjorden Fault Zone in north central Spitsbergen, Svalbard: *Geological Magazine*, v. 133, p. 63-84.
- McClay, K., 1992, Glossary of thrust tectonics terms: *Thrust tectonics*, v. 419, p. 419-433.
- McClay, K. R., 2004, *Thrust Tectonics and Hydrocarbon Systems: AAPG Memoir 82*, AAPG.
- Menéndez, B., W. Zhu, and T.-F. Wong, 1996, Micromechanics of brittle faulting and cataclastic flow in Berea sandstone: *Journal of structural geology*, v. 18, p. 1-16.
- Mitra, G., 1994, Strain variation in thrust sheets across the Sevier fold-and-thrust belt (Idaho-Utah-Wyoming): Implications for section restoration and wedge taper evolution: *Journal of Structural Geology*, v. 16, p. 585-602.
- Mitra, S., 1990, Fault-Propagation Folds: Geometry, Kinematic Evolution, and Hydrocarbon Traps (1): *AAPG Bulletin*, v. 74, p. 921-945.
- Mitra, S., 2003, A unified kinematic model for the evolution of detachment folds: *Journal of Structural Geology*, v. 25, p. 1659-1673.
- Mogi, K., 1967, Effect of the intermediate principal stress on rock failure: *Journal of Geophysical Research*, v. 72, p. 5117-5131.
- Morley, C., 1988, Out - of - sequence thrusts: *Tectonics*, v. 7, p. 539-561.
- Muñoz, J., A. Martínez, and J. Vergés, 1986, Thrust sequences in the eastern Spanish Pyrenees: *Journal of Structural Geology*, v. 8, p. 399-405.
- Mäkel, G., 2007, *The modelling of fractured reservoirs: constraints and potential for fracture network geometry and hydraulics analysis: Geological Society, London, Special Publications*, v. 292, p. 375-403.
- Nathorst, A. G., 1910, *Beiträge zur Geologie der Bären-Insel, Spitzbergens und des König-Karl-Landes*, v. 10, Uppsala University Geological Institute Bulletin.
- Nejbert, K., K. P. Krajewski, E. Dubińska, and Z. Pécskay, 2011, Dolerites of Svalbard, north-west Barents Sea Shelf: age, tectonic setting and significance for geotectonic interpretation of the High-Arctic Large Igneous Province: *Polar Research*, v. 30.

- Nelson, R., 2001, *Geologic analysis of naturally fractured reservoirs*, 2nd Edition, Gulf Professional Publishing, p. 332.
- Nystuen, J. P., A. Andresen, R. A. Kumpulainen, and A. Siedlecka, 2008, Neoproterozoic basin evolution in Fennoscandia, East Greenland and Svalbard: *Episodes*, v. 31, p. 35.
- Odling, N., P. Gillespie, B. Bourguine, C. Castaing, J. Chiles, N. Christensen, E. Fillion, A. Genter, C. Olsen, and L. Thrane, 1999, Variations in fracture system geometry and their implications for fluid flow in fractured hydrocarbon reservoirs: *Petroleum Geoscience*, v. 5, p. 373-384.
- Odling, N., S. Harris, and R. Knipe, 2004, Permeability scaling properties of fault damage zones in siliclastic rocks: *Journal of Structural Geology*, v. 26, p. 1727-1747.
- Odling, N. E., 1992, Permeability of natural and simulated fracture patterns: *Structural and Tectonic Modelling and Its Application to Petroleum Geology*, edited by RM Larsen et al, p. 365-380.
- Ogata, K., K. Senger, A. Braathen, J. Tveranger, and S. Olaussen, 2014, The importance of natural fractures in a tight reservoir for potential CO₂ storage: a case study of the upper Triassic–middle Jurassic Kapp Toscana Group (Spitsbergen, Arctic Norway): *Geological Society, London, Special Publications*, v. 374, p. 395-415.
- Onasch, C. M., and W. M. Dunne, 1993, Variation in quartz arenite deformation mechanisms between a roof sequence and duplexes: *Journal of Structural Geology*, v. 15, p. 465-475.
- Orvin, A. K., 1940, *Outline of the geological history of Spitsbergen*: Skrift. Svalbard og Ishavet, no. 78, p. 1-57.
- Paterson, M. S., 1978, *Experimental Rock Deformation - the Brittle Field.*: Springer-Verlag, New York., p. 173-174.
- Price, R. A., 1967, The tectonic significance of mesoscopic subfabrics in the southern Rocky Mountains of Alberta and British Columbia: *Canadian Journal of Earth Sciences*, v. 4, p. 39-70.
- Priest, S. D., 1993, *Discontinuity analysis for rock engineering.*: Chapman & Hall, London, UK, p. 32.
- Pumpelly, R., 1918, *My reminiscences*: Henry Hold and Company, New York, v. 2.
- Rafaelsen, B., G. Elvebakk, K. Andreassen, L. Stemmerik, A. Colpaert, and T. J. Samuelsen, 2008, From detached to attached carbonate buildup complexes—3D seismic data from the upper Palaeozoic, Finnmark Platform, southwestern Barents Sea: *Sedimentary Geology*, v. 206, p. 17-32.
- Ramberg, I. B., A. Nøttvedt, I. Bryhni, A. Solli, and Ø. Nordgulen, 2006, Landet blir til: Norges geologi, Norsk geologisk forening, p. 279.
- Ramsay, J., 1967, *Folding and Fracturing of Rocks*: McGraw-Hill, New York.
- Ramsay, J., and M. Huber, 1983, *The techniques of modern structural geology: Strain Analysis*. Academic Press, London, v. 1, p. 3-7.
- Ramsey, J. M., and F. M. Chester, 2004, Hybrid fracture and the transition from extension fracture to shear fracture: *Nature*, v. 428, p. 63-66.
- Ray, S. K., 2006, Scaling properties of thrust fault traces in the Himalayas and inferences on thrust fault growth: *Journal of structural geology*, v. 28, p. 1307-1315.

- Renshaw, C. E., T. A. Myse, and S. R. Brown, 2003, Role of heterogeneity in elastic properties and layer thickness in the jointing of layered sedimentary rocks: *Geophysical research letters*, v. 30.
- Roeder, D., 2010, *Fold–thrust belts at Peak Oil*: Geological Society, London, Special Publications, v. 348, p. 7-31.
- Rowley, D. B., and A. L. Lottes, 1988, Plate-kinematic reconstructions of the North Atlantic and Arctic: Late Jurassic to present: *Tectonophysics*, v. 155, p. 73-120.
- Rudkiewicz, J. L., S. Sherkati, and J. Letouzey, 2007, Evolution of maturity in Northern Fars and in the Izeh Zone (Iranian Zagros) and link with hydrocarbon prospectivity, *Thrust Belts and Foreland Basins*, Springer, p. 229-246.
- Salvini, F., and F. Storti, 2001, The distribution of deformation in parallel fault-related folds with migrating axial surfaces: comparison between fault-propagation and fault-bend folding: *Journal of Structural Geology*, v. 23, p. 25-32.
- Schultz, R. A., and H. Fossen, 2008, Terminology for structural discontinuities: *AAPG bulletin*, v. 92, p. 853-867.
- Secor, D., 1969, Mechanics of natural extension fracturing at depth in the earth's crust: *Research in tectonics: Geological Survey of Canada Special Paper*, p. 68-52.
- Secor, D. T., 1965, Role of fluid pressure in jointing: *American Journal of Science*, v. 263, p. 633-646.
- Segall, P., and D. D. Pollard, 1983, Joint formation in granitic rock of the Sierra Nevada: *Geological Society of America Bulletin*, v. 94, p. 563-575.
- Senger, K., J. Tveranger, K. Ogata, A. Braathen, and S. Planke, 2014, Late Mesozoic magmatism in Svalbard: A review: *Earth-Science Reviews*, v. 139, p. 123-144.
- Shackleton, J. R., M. L. Cooke, J. Vergés, and T. Simó, 2011, Temporal constraints on fracturing associated with fault-related folding at Sant Corneli anticline, Spanish Pyrenees: *Journal of Structural Geology*, v. 33, p. 5-19.
- Shaw, J. H., C. Connors, and J. Suppe, 2005, *Seismic Interpretation of Contractional Fault - related Folds: An AAPG Seismic Atlas*.
- Sibson, R., 1977, Fault rocks and fault mechanisms: *Journal of the Geological Society*, v. 133, p. 191-213.
- Smart, K. J., W. M. Dunne, and R. D. Krieg, 1997, Roof sequence response to emplacement of the Wills Mountain duplex: the roles of forethrusting and scales of deformation: *Journal of Structural Geology*, v. 19, p. 1443-1459.
- Smith, D., W. Harland, N. Hughes, and C. Pickton, 1976, The geology of Kong Karls Land, Svalbard: *Geological Magazine*, v. 113, p. 193-232.
- Stearns, D. W., 1968, Certain aspects of fracture in naturally deformed rocks: *Rock mechanics seminar*, p. 97-118.
- Stearns, D. W., and M. Friedman, 1972, Reservoirs in fractured rock, in *Stratigraphic oil and gas fields: Classification, exploration methods, and case histories: American Association of Petroleum Geologists*, v. 16, p. 82-106.
- Steel, R., A. Dalland, K. Kalgraff, and V. Larsen, 1981, The central Tertiary basin of Spitsbergen - sedimentary development of a sheared-margin basin. : In: J.

- Wm. Kerr and A.J. Fergusson (eds.), *Mem. Can. Soc. Petrol. Geol.*, v. 7, p. 647-664.
- Steel, R., J. Gjelberg, W. Helland-Hansen, K. Kleinspehn, A. Nøttvedt, and M. Rye-Larsen, 1985, The Tertiary strike-slip basins and orogenic belt of Spitsbergen: *The Society of Economic Palentologists and Mineralogists*, v. 37, p. 339-359.
- Steel, R. J., and D. Worsley, 1984, Svalbard's post-Caledonian strata—an atlas of sedimentational patterns and palaeogeographic evolution, *Petroleum geology of the North European margin*, Springer, p. 109-135.
- Suppe, J., 1983, Geometry and kinematics of fault-bend folding: *American Journal of science*, v. 283, p. 684-721.
- Suppe, J., and D. Medwedeff, 1984, Fault-propagation folding: *Geological Society of America Abstracts with Programs*, 16, p. 670.
- Suppe, J., and D. Medwedeff, 1990, Geometry and kinematics of fault-propagation folding: *Eclogae Geologicae Helvetiae*, v. 83, p. 409-454.
- Talwani, M., and O. Eldholm, 1977, Evolution of the Norwegian-Greenland sea: *Geological Society of America Bulletin*, v. 88, p. 969-999.
- Tarduno, J. A., 1998, The high Arctic large igneous province: Abstract, *Int. Conf. Arctic Margins (ICAM III)*, Celle, Germany, Fed. Inst. Geosci. Nat. Res.
- Tarduno, J. A., D. B. Brinkman, P. R. Renne, R. D. Cottrell, H. Scher, and P. Castillo, 1998, Late Cretaceous Arctic volcanism; tectonic and climatic connections: In *Am. Geophys. Union Spring Meeting Abstracts*. Washington, D. C., Am. Geophys. Union.
- Tavani, S., and F. Storti, 2006, Fault - bend folding as an end - member solution of (double - edge) fault - propagation folding: *Terra Nova*, v. 18, p. 270-275.
- Travé, A., P. Labaume, and J. Vergés, 2007, Fluid systems in foreland fold-and-thrust belts: an overview from the southern Pyrenees, *Thrust belts and foreland basins*, Springer, p. 93-115.
- Tsang, Y., 1984, The effect of tortuosity on fluid flow through a single fracture: *Water Resources Research*, v. 20, p. 1209-1215.
- Turner, F. J., and L. E. Weiss, 1963, *Structural analysis of metamorphic tectonites*, McGraw-Hill, New York.
- Underwood, C. A., M. L. Cooke, J. A. Simo, and M. A. Muldoon, 2003, Stratigraphic controls on vertical fracture patterns in Silurian dolomite, northeastern Wisconsin: *AAPG bulletin*, v. 87, p. 121-142.
- Van der Pluijm, B. A., and S. Marshak, 2004, *Earth structure: an introduction to structural geology and tectonics*. Chapter 6., WW Norton; 2nd ed., New York, p. 122.
- Wehr, A., and U. Lohr, 1999, Airborne laser scanning—an introduction and overview: *ISPRS Journal of Photogrammetry and Remote Sensing*, v. 54, p. 68-82.
- Wennberg, O., T. Svånå, M. Azizzadeh, A. Aqrabi, P. Brockbank, K. Lyslo, and S. Ogilvie, 2006, Fracture intensity vs. mechanical stratigraphy in platform top carbonates: the Aquitanian of the Asmari Formation, Khaviz Anticline, Zagros, SW Iran: *Petroleum Geoscience*, v. 12, p. 235-246.
- Wennberg, O. P., A. Andresen, S. Hansen, and S. G. Bergh, 1994, Structural evolution of a frontal ramp section of the West Spitsbergen, Tertiary fold

- and thrust belt, north of Isfjorden, Spitsbergen: *Geological Magazine*, v. 131, p. 67-80.
- Weyl, P. K., 1960, Porosity through dolomitization: conservation-of-mass requirements: *Journal of Sedimentary Research*, v. 30, p. 85-90.
- Wierzbicki, R., J. J. Dravis, I. Al-Aasm, and N. Harland, 2006, Burial dolomitization and dissolution of upper Jurassic Abenaki platform carbonates, Deep Panuke reservoir, Nova Scotia, Canada: *AAPG Bulletin*, v. 90, p. 1843-1861.
- Wilkerson, M., T. Apotria, and T. Farid, 2002, Interpreting the geologic map expression of contractional fault-related fold terminations: lateral/oblique ramps versus displacement gradients: *Journal of Structural Geology*, v. 24, p. 593-607.
- Wilkerson, M. S., and S. Marshak, 1997, Fold-thrust belts - an essay. In: van der Pluijm, B. A., Marshak, S. (Eds.). *Earth Structure*. WCB/McGraw-Hill: US Division, p. 366-387.
- Woodworth, J. B., 1896, On the fracture system of joints, with remarks on certain great fractures. : *Boston Soc. Host. Proc.*, v. 27, p. 63-183.
- Worsley, D., 1986, The geological history of Svalbard: evolution of an Arctic archipelago, *Den norske stats oljeselskap as*, Norway, p. 35-39.
- Worsley, D., 2008, The post - Caledonian development of Svalbard and the western Barents Sea: *Polar Research*, v. 27, p. 298-317.
- Wu, S., 1993, Fractal strain distribution and its implications for cross-section balancing: *Journal of Structural Geology*, v. 15, p. 1497-1507.

Appendix 1 - Unit description of Kapp Starostin Formation

Unit	Rock-description of Kapp Starostin Formation
0	<p>Grey limestone with patches of yellow weathering, and a sharp upper boundary. The unit is changing between mudstone and floatstone, containing brachiopods, brachiopod fragments, algae lamination, bioturbation, root traces and stylolites. The bed thickness varies between 15-70 cm, and has a total thickness of 7.25 m.</p> <p>Stratigraphically below the limestone is a 4 m thick package of white gypsum with weathering channels and alternating grey dolomite beds. The dolomite beds are 1-10 cm thick. The gypsum is weak, while the dolomites are more rigid. The beds are folded towards the top of the unit.</p>
1	<p>Medium grey color, with scattered yellow weathering. Going from a floatstone to rudstone, but mainly a rudstone, with a fine sand matrix. The unit is rich in brachiopods (macrofossils), and has large clasts towards the top. The beds vary between 15-90 cm in bed thickness. Stylolites have been observed, and some of the beds have an erosive contact. The unit does also have a sharp contact to the underlying Gipshuken Formation. The total unit has a thickness of ~2 m and are interpreted to be a brachiopod limestone of the Vøringen Member.</p>
2	<p>Grey spiculitic unit, with black pseudonodules. Thin mud-layers divide the beds. The lower boundary is where the brachiopod rich limestone goes into organic rich very dark shale, with sharp boundary. The shale bed thickens towards north. The bed thickness is between 15-65 cm, and is thickening upwards. This unit is interpreted to be the first unit that is part of the Svenskegga Member.</p>
3	<p>Alternating grey, highly silicified shale and black softer shale. Some burrows observed, mainly towards the top of the unit. Total thickness is 22 m, and highly fractured. The black softer shale is thinning upwards, going from beds with a thickness of 50 cm to a thickness of 1-5 cm. This bedded spiculite contains dark grey to black lenses that seem to be of secondary precipitation. These lenses make up a wavy internal structure.</p>
4	<p>Medium grey spiculitic shale that gets lighter grey towards the top of the unit. Fracturing causing a nodular wavy bedding. This type of structure is typical for Kapp Starostin Formation. The total thickness is ~2.30 m, with bed-thickness of 25-55 cm. The upper and lower boundaries are both sharp boundaries. Burrows are observed towards the top (lamellaeichnus), going both vertical and horizontal. High concentration of calcite veins.</p>
5	<p>Grey limestone with patches of yellow weathering. Wavy pattern with alternating darker and lighter grey to yellow limestone. The darker beds are clay-rich, while the lighter beds are more sandy, or rich in carbonate. Some layers are continuous while others are more undulating. Lots of burrows (lamellaeichnus) observed. The total thickness is ~4 m, with bed ranging from 10-75 cm in thickness. The lower boundary contains fault breccia. Classified as a mudstone.</p>
6	<p>Light grey, highly silicified unit with nodular bed boundaries. The total thickness is ~4 m and highly fractured. The beds vary from 20–90 cm in bed</p>

	thickness.
7	Medium grey highly silicified unit with a thin carbonate layer in the middle. The silicified shale is highly fractured, and the upper boundary is gradual with a 2 cm thick layer of shale. The thin carbonate layer is full of burrows. The total thickness is ~2 m, and the beds vary from 20-40 cm in thickness.
8	Light grey to bluish unit, going into a more yellowish to greyish color in the upper 3 meters. Angular eroded and rich in chert (chert nodules). This is a highly silicified unit, with a high content of dolomite and sulfide concretions (pyrite). The unit has a total thickness of ~9 m. The beds range in thickness from 15 cm to 95 cm. There are observed crinoids towards the base of the unit, and burrows in the upper 3 meters. The trace fossil zoophycos are also observed. The uppermost 20 cm of the unit is shale, rich in brachiopods and bioturbation.
9	Medium grey carbonate mudstone. Rich in brachiopods, sponges and unknown fossil fragments. The whole unit is shaly, but it is getting more shaly towards the top. The beds range in thickness from 15 cm to 1 m, and have a total thickness of ~3 m. A reverse fault is cutting through the unit. Fault breccia observed along the fault plane.
10	Yellowish crinoid limestone with lamina of shale between the beds. The unit has a high content of brachiopods, bryozoans, sponges and crinoids, and is all over a rudstone except the lowermost part that is more a floatstone. In the middle of the unit there is a shaly package of carbonate mudstone, with a high concentration of brachiopod fragments. The whole shaly package is 50 cm thick, where the brachiopod-rich bed has a thickness of 10 cm. At the very top of the unit there is characteristic burrows, both horizontal and vertical, filled with darker sediments from the overlying unit. The whole unit has a thickness of ~9 m.
11	Grey shaly carbonate mudstone. Brachiopod fragments observed. Total thickness of the unit is 1 m.
12	Grey highly silicified unit, containing brachiopods and shell imprints. The unit is shifting between light grey and grey color, indicating shift in grain-size. The beds are undulating to continuous and has a thickness between 5 cm and 60 cm.
13	Grey carbonate unit with patches of yellow weathering. Rich in brachiopods and bryozoans. Total thickness is 90 cm. "Brick-unit". Classified as a floatstone.
14	Alternating grey to dark grey limestone, with a high content of silica. The unit is shifting between mudstone and wackestone, which can be seen in intervals with more and less shale. Sponges, crinoids, bryozoans and brachiopods are abundant, and a plumose joint is observed close to the base of the unit. The total thickness is ~14 m, with bed thicknesses ranging from 5 cm to 75 cm.
15	Slope forming, soft weathered calcareous shale, having a greyish color with some patches of yellow weathering. The total thickness is 1.3 m, mainly of slope scree. No individual beds were possible to distinguish.
16	Bedded silicified mudstone with shaly intercalations. Some thin carbonate beds are also present (max. 8 cm thick). The unit have large oxidized patches on the surface, and a total thickness of ~3.5 m. The beds are highly bioturbated, and thinning towards the top of the unit.
17	Grey to dark grey silicified mudstone with shaly intercalations and patches of yellow weathering. Some thin carbonate beds present (5-15 cm thick). The unit

	contains brachiopods and burrows.
18	Silicified light grey to dark grey mudstone with intercalations of shale. Yellow weathered areas occur within the unit, often occurring along the beds. Brachiopods are present, but rarely observed. Towards the top of the unit is a 55 cm thick bed of siliceous shale. This is a highly fractured unit with a total thickness of ~18 m. Burrows are present.
19	Light grey limestone with patches of yellow weathering, and intercalating shale. Total thickness of 2.95 m.
20	Silicified light grey to dark grey mudstone with intercalations of shale. Internal wavy bedding and no fossils observed. The total thickness of the unit is ~6 m.
21	Medium grey limestone, packed with whole brachiopods and brachiopod fragments. This is a rudstone with a total thickness of ~2 m.
22	Characteristic light grey to white marker bed made up of mainly chert, with intercalations of shale (up to 5 cm thick). The middle part consists of thicker and more massive beds than the ones below and above. Abundant brachiopods throughout the whole unit. The total thickness is ~18 m.
23	Light grey silicified mudstone, rich in chert. The unit has abundant calcite veins (max. 7 cm in thickness), going in all directions. The uppermost bed has a highly oxidized surface and can be seen as a marker bed. The beds are thick, from 75 cm up to 1.60 m, and the total thickness is ~5 m.
24	Pyritic mudstone, highly silicified with a high content of chert. Intercalations of laminated mud are present. The unit is dark grey, but most of the surface has a yellowish weathering color. The unit include a 40 cm thick bed of shale, and are in total ~5 m.
25	Dark grey highly silicified shale, with intercalation of laminated mud. The beds are thickest at the top and base of the unit (~1 m), while the middle part has beds with thickness of ~30 cm. The bedding is wavy and there is abundance of burrows. Two reverse faults are also observed.
26	Slightly wavy black calcareous shale, with abundance of burrows. The total thickness is 1.2 m.

Appendix 2 – Lidarscan measurements

Measurements and calculations from lidarscan, measured in the software Lime.

Meso-scale Fold shortening (S_F)						
Box	Measured bed	L_{measured} (m)	Corrected L (m)	$L_{0\text{measured}}$ (m)	Corrected L_0 (m)	S_F (m)
1	MF1-aW1	100	-	110	-	10
	MF1-aW2	100	-	106	-	6
	MF1-bW	100	-	136	-	36
	MF1-cW	100	-	103	-	3
2	MF2-a1	100	87	105	91	4
	MF2-a2	100	87	105	91	4
	MF2-a3	100	87	104	90	3
	MF2-a4	100	87	102	88	1
	MF2-a5	100	87	104	90	3
	MF2-a6	100	87	103	89	2
	MF2-b1	100	87	103	89	2
	MF2-b2	100	87	108	94	7
	MF2-b3	100	87	108	94	7
	MF2-b4	100	87	103	89	2
	MF2-b5	100	87	104	90	3
	MF2-b6	100	87	128	111	24
	MF2-c1	100	87	110	95	8
	MF2-c2	100	87	121	105	18
	MF2-c3	100	87	117	101	14
	MF2-d1	100	87	111	96	9
	MF2-d2	100	87	103	89	2
	MF2-d3	100	87	104	90	3
	MF2-e	100	87	118	102	15
	MF2-f1	100	87	115	100	13
	MF2-f2	100	87	166	144	57
	MF2-g	100	87	189	164	77
	MF2N-a	100	-	102	-	2
	MF2N-b1	100	-	105	-	5
MF2N-b2	100	-	240	-	140	
MF2N-b3	100	-	122	-	22	

Meso-scale Thrust shortening (S_T)					
Box	Measured bed	T_1 (m)	T_2 (m)	S_T (measured) (m)	Corrected S_T (m)
2	MF2-c2	25	-	25	22
	MF2-e	12	0.5	12.5	10.9
	MF2-f1	10	-	10	9
	MF2-f2	41	-	41	36
	MF2N-a	0.9	0.8	1.7	1.5

Macro-scale Fold shortening (S_F)						
Box	Measured bed	L_{measured} (m)	Corrected L (m)	$L_{0\text{measured}}$ (m)	Corrected L_0 (m)	S_F (m)
1	MMF1-topW	397	-	542	-	145
	MMF1-baseW	397	-	592	-	195
	MMF1-topE	316	-	461	-	145
	MMF1-baseE	316	-	482	-	166
2	MMF2-W	1143	990	1198	1037	47
	MMF2-E	1018	-	1715	-	697

Macro-scale Fold shortening (S_F) for MMF2-E					
Measured bed	L_{measured} (m)	Corrected L (m)	$L_{0\text{measured}}$ (m)	Corrected L_0 (m)	S_F (m)
MMF2-E1	680	589	693	600	11
MMF2-E2	429	429	1115	1115	686
Total MMF2-E		1018		1715	697

Appendix 3 – Scanlines

All scanlines are collected during fieldwork of summer 2013 (sas X.13) and 2014 (sas X.14), were all scanlines of 2013 are strike parallel while scanlines of 2014 are either strike parallel or dip parallel. The scanlines include fracture frequency (fractures per meter), fracture orientations, bed thickness, lithological unit and additional fracture characteristics such as; is it through-going (TG) or bed-confined (BC), and does it have calcite precipitation (CP). Note that all scanlines are collected from the same ridge. This result in a similar UTM, and not all scanlines has a registered GPS coordinate (SAS 2.13 – SAS 11.13).

Locality: SAS 101.13
GPS Coordinates: N78 29,273 - E014 13,923
Scanline number: SAS 1.13 strike parallel
Lithological unit: 0
Bed thickness: 30 cm
Bed orientation: 356/?

Fractures:

Unit (m)	Distance (cm)	Fracture frequency	Strike	Dip	Type of fracture	Comments
0-1	1	5	257	89	BC	Low angular
	32		257	89	BC	
	42		232	34	TG	
	43		275	89	BC	
	90		275	89	BC	

1-2	4	4	264	88	BC	
	22		264	88	BC	
	34		197	44		Slickn line 190°, steps - reverse movement
2-3	68	3	264	88	BC	
	1		85	89	BC	CP
	40		85	89	BC	CP
3-4	79	3	85	89	BC	CP
	8		254	81	TG	
	58		254	81	BC	
4-5	73	5	254	81	BC	
	3		232	70	BC	
	32		82	80	BC	
	61		82	80	BC	
	81		82	80	BC	
5-6	96	4	82	80	BC	
	26		255	80	BC	CP
	65		255	80	BC	CP
	78		174	50	BC	CP, slick'n lines 193°, steps - reverse movement
6-7	97	2	255	80	BC	
	54		80	70	BC	
	76		80	70	BC	

Calcite veins:

Unit (m)	Distance (cm)	Fracture frequency	Strike	Dip	Type of fracture	Comments
0-1	4	10	253	79	BC	Less than 1mm thick. Representative through the whole bed
	8		253	79	BC	
	13		253	79	BC	
	20		253	79	BC	
	38		253	79	BC	
	41		253	79	BC	
	44		253	79	BC	
	48		253	79	BC	
	59		253	79	BC	
	62		253	79	BC	
1-2		0				No veins over 1 mm in thickness
2-3		0				No veins over 1 mm in thickness
3-4	55	1	356	?	BC	Layer parallell
4-5	50	1	174	52	BC	Low angular
5-6		0				No veins over 1 mm in thickness
6-7	30	1	172	40		Low angular

Locality: SAS 101.13
Scanline number: SAS 2.13 strike parallel
Lithological unit: 0
Bed thickness: 40 cm
Bed orientation: 356/?

Fractures:

Unit (m)	Distance (cm)	Fracture frequency	Strike	Dip	Type of fracture	Comments
0-1	1	3	256	75	BC	CP
	30		256	75	BC	CP
	80		256	75	BC	CP
1-2	22	3	256	88	BC	Calcite vein at 1.26 m. 3 mm thick, 256/89
	57		256	88	BC	
	90		256	88	BC	
2-3	36	2	76	86	BC	
	55		76	86	BC	
3-4	33	2	248	88	BC	
	69		248	88	BC	
4-5	15	1	284	68	TG	
5-6	15	3	58	86	TG	
	83		58	86	BC	
	93		58	86	BC	
6-7	33	2	96	82	BC	
	50		140	40	BC	
7-8	20	3	262	74	BC	
	54		262	74	BC	
	57		262	74	BC	

8-9	14	3	68	86	BC
	75		68	86	BC
	89		68	86	TG

Locality: SAS 101.13
Scanline number: SAS 3.13 strike parallel
Lithological unit: 0
Bed thickness: 45 cm
Bed orientation: 356/?

Fractures:

Unit (m)	Distance (cm)	Fracture frequency	Strike	Dip	Type of fracture	Comments
0-1	1	2	301	76	BC	CP
	99		301	76	BC	CP
1-2	50	1	265	84	TG	CP, 1.5 mm thick vertical vein (218/78)
2-3	5	2	10	48	TG	CP
	65		284	88	BC	
3-4	37	2	76	88	BC	Irregular shape on fracture
	93		76	88	BC	
4-5	50	2	278	62	BC	
	99		97	76	BC	

Locality: SAS 101.13
Scanline number: SAS 4.13 strike parallel
Lithological unit: 1
Bed thickness: 1.25 m
Bed orientation:

Fractures:

Unit (m)	Distance (cm)	Fracture frequency	Strike	Dip	Type of fracture	Comments
0-1		0				
1-2	20	2	168	50	BC	CP
	56		82	82	TG	
2-3	16	2	292	66	BC	
	80		300	70	TG	
3-4	70	1	244	72	TG	
4-5		0				
5-6	2	2	260	88	TG	
	72		260	88	TG	
6-7	7	3	88	80	BC	
	38		88	80	TG	
	75		280	80	BC	
7-8		0				
8-9	60	1	80	84	BC	8.79 m: calcite vein (090/86) BC
9-10	20	1	228	74	BC	
10-11	3	2	214	84	BC	
	50		250	74	BC	
11-12	25	1	276	66	BC	

12-13	41	1	326	52	BC	
13-14	23	1	118	52	TG	CP

Locality: SAS 101.13
Scanline number: SAS 4.13 strike parallel
Lithological unit: 1
Bed thickness: 1.25 m
Bed orientation:

Fractures:

Unit (m)	Distance (cm)	Fracture frequency	Strike	Dip	Type of fracture	Comments
0-1		0				
1-2	20	2	168	50	BC	CP
	56		82	82	TG	
2-3	16	2	292	66	BC	
	80		300	70	TG	
3-4	70	1	244	72	TG	
4-5		0				
5-6	2	2	260	88	TG	
	72		260	88	TG	
6-7	7	3	88	80	BC	
	38		88	80	TG	
	75		280	80	BC	
7-8		0				
8-9	60	1	80	84	BC	8.79 m: calcite vein (090/86) BC
9-10	20	1	228	74	BC	
10-11	3	2	214	84	BC	
	50		250	74	BC	
11-12	25	1	276	66	BC	

12-13	41	1	326	52	BC	
13-14	23	1	118	52	TG	CP

Locality: SAS 101.13
Scanline number: SAS 5.13 strike parallel
Lithological unit: 3
Bed thickness: 25 cm
Bed orientation:

Fractures:

Unit (m)	Distance (cm)	Fracture frequency	Strike	Dip	Type of fracture	Comments
0-1	4	3	322	80	BC	
	9		54	70	BC	
	25		54	70	TG	
1-2	21	2	65	76	TG	CP
	90		65	76	BC	CP
2-3	46	2	71	76	BC	
	59		71	76	BC	
3-4	18	1	122	48	TG	
4-5	1	2	78	72	TG	
	89		78	72	TG	
5-6	37	1	34	78	TG	
6-7	10	2	333	52	TG	Oxidation
	69		255	82	BC	
7-8	19	3	336	74	TG	
	47		336	74	TG	
	87		336	74	TG	
8-9	50	1	241	61	TG	
9-10		0				

10-11	35	1	248	80	TG	CP
-------	----	---	-----	----	----	----

Locality: SAS 101.13
Scanline number: SAS 6.13 strike parallel
Lithological unit: 5
Bed thickness: 75 cm
Bed orientation:

Fractures:

Unit (m)	Distance (cm)	Fracture frequency	Strike	Dip	Type of fracture	Comments
0-1	12	3	100	74	TG	CP
	45		100	74	TG	CP
	82		100	74	TG	CP
1-2	45	3	88	80	TG	CP
	67		88	80	TG	CP
	98		88	80	TG	CP
2-3	82	1	221	72	TG	
3-4	38	1	288	80	BC	CP, Irregular fracture
4-5		0				
5-6	43	1	321	56	TG	CP
6-7	34	1	348	50	TG	CP
7-8	98	1	288	84	TG	CP
8-9		0				
9-10	77	1	231	88	TG	CP
10-11		0				
11-12	94	1	235	78	TG	CP
12-13		0				
13-14	46	1	269	78	TG	

14-15	42	1	328	60	TG	CP
15-16	20	3	298	60	TG	CP
	46		298	60	TG	CP
	87		298	60	TG	CP
16-17	82	1	265	79	BC	
17-18	39	1	317	62	TG	CP
18-19		0				
19-20	98	1	291	70	BC	

Calcite veins

Unit (m)	Distance (cm)	Fracture frequency	Strike	Dip	Type	Comments
1-7		0				
7-8	22	2	321	54	TG	
	26		321	54	TG	
8-9		0				
9-10		0				
10-11		0				
11-12		0				
12-13	94	1	252	76	TG	
13-14	70	1	242	74	TG	5 m thick

Locality: SAS 101.13
Scanline number: SAS 7.13 strike parallel
Lithological unit: 6
Bed thickness: 50 cm
Bed orientation:

Fractures:

Unit (m)	Distance (cm)	Fracture frequency	Strike	Dip	Type of fracture	Comments
0-1		0				0.95: Calcite vein (252/74) TG
1-2		0				
2-3		0				
3-4	47	1	250	80	TG	CP
4-5	64	1	281	74	BC	
5-6	10	3	302	70	TG	CP
	57		302	70	TG	CP
	90		273	70	TG	CP
6-7		0				
7-8		0				
8-9	22	2	268	58	TG	CP
	70		268	58	TG	
9-10	40	1	68	80	TG	CP
10-11		0				
11-12	10	2	262	64	BC	
	65		262	64	BC	

Locality: SAS 101.13
Scanline number: SAS 8.13 strike parallel
Lithological unit: 6
Bed thickness: 50 cm
Bed orientation: 174/38

Fractures:

Unit (m)	Distance (cm)	Fracture frequency	Strike	Dip	Type of fracture	Comments
0-1	14	4	252	80	BC	
	32		252	80	BC	
	48		252	80	BC	
	82		252	80	BC	
1-2	13	2	254	75	BC	
	40		254	75	BC	
2-3	11	3	254	80	BC	
	70		174	38	TG	
	93		264	78	BC	
3-4	62	1	262	78	BC	
4-5	6	3	256	64	BC	
	70		256	64	TG	
	81		256	64	TG	
5-6	1	5	253	84	BC	CP
	13		253	84	BC	CP
	19		270	80	TG	CP
	26		72	70	TG	
	58		80	84	BC	CP
6-7	18	4	262	88	TG	CP

	30		262	88	BC	
	41		262	88	BC	
	95		262	88	TG	CP
7-8	38	3	256	80	TG	
	52		256	80	TG	
	88		256	80	BC	CP
8-9	69	2	68	82	TG	CP
	86		226	72	BC	
9-10	10	3	76	86	BC	
	25		76	86	BC	CP
	56		64	84	TG	CP
10-11	36	3	260	80	BC	
	66		260	80	BC	
	95		260	80	BC	CP
11-12	7	4	78	84	TG	CP
	25		78	84	BC	
	79		78	84	BC	
	92		78	84	TG	CP
12-13	21	3	268	88	BC	
	78		268	88	TG	CP
	97		268	88	TG	
13-14	17	3	68	86	BC	CP
	81		88	88	TG	
	99		88	88	TG	CP
14-15	66	1	268	82	TG	CP
15-16	22	2	76	84	BC	CP
	70		342	62	TG	

Locality: SAS 101.13
Scanline number: SAS 9.13 strike parallel
Lithological unit: 8
Bed thickness: 85 cm
Bed orientation: 160/38

Fractures:

Unit (m)	Distance (cm)	Fracture frequency	Strike	Dip	Type of fracture	Comments
0-1	20	5	88	84	BC	
	49		88	84	BC	
	60		88	84	BC	
	81		88	84	BC	
	90		88	84	BC	
1-2	12	6	82	84	TG	CP
	39		82	84	TG	
	48		82	84	BC	
	69		82	84	TG	
	79		82	84	BC	
2-3	26	4	256	70	TG	
	38		256	70	BC	
	55		256	70	TG	
	70		332	52	TG	
3-4	90	1	74	84	TG	CP
4-5	48	1	58	82	TG	
5-6	81	1	260	84	TG	

6-7	50	1	36	78	TG	CP
7-8	56	2	36	68	BC	
	70		262	70	BC	
8-9	3	1	260	70	TG	CP
9-10	50	3	264	64	TG	
	68		264	64	BC	
	86		264	64	TG	
10-11	3	9	256	62	BC	
	25		260	72	TG	
	40		260	72	TG	
	56		260	72	TG	
	65		260	72	TG	
	71		260	72	TG	
	73		260	72	TG	
	76		260	72	TG	
	80		260	72	TG	

Locality: SAS 101.13
Scanline number: SAS 10.13 strike parallel
Lithological unit: 10
Bed thickness: 45 cm
Bed orientation: 172/42

Fractures:

Unit (m)	Distance (cm)	Fracture frequency	Strike	Dip	Type of fracture	Comments
0-1	21	4	264	84	BC	
	62		264	84	BC	
	88		270	62	BC	
	97		270	62	BC	
1-2	21	2	310	54	TG	CP
	90		320	58	TG	CP
2-3	48	1	310	56	TG	CP
3-4	79	1	316	64	TG	
4-5	24	6	248	88	BC	CP, Calcite vein: 4.34 (248/88) BC
	41		248	88	BC	CP
	50		248	88	BC	CP
	67		248	88	BC	CP
	75		248	88	BC	CP
	90		248	88	BC	CP
	5-6		46	1	310	58
6-7	17	2	250	82	BC	
	66		250	82	BC	
7-8	3	4	326	64	TG	

	42		316	66	TG
	81		84	80	BC
	96		288	76	BC
8-9	5	3	304	68	TG
	38		288	70	TG
	62		324	68	TG
9-10	5	1	320	62	TG

Locality: SAS 101.13
Scanline number: SAS 11.13 strike parallel
Lithological unit: 10
Bed thickness: 45 cm
Bed orientation: 174/48

Fractures:

Unit (m)	Distance (cm)	Fracture frequency	Strike	Dip	Type of fracture	Comments
0-1	19	4	60	82	TG	
	47		60	82	TG	
	61		60	82	TG	
	75		60	82	BC	CP
1-2	9	2	58	86	BC	CP
	64		58	86	BC	
2-3	30	3	64	82	BC	
	43		64	82	BC	
	89		64	82	BC	
3-4	12	4	60	84	BC	
	46		60	84	BC	
	70		60	84	BC	
	98		60	84	BC	
4-5	76	2	282	62	BC	
	92		282	62	BC	
5-6	41	1	272	62	TG	
6-7	6	2	316	58	TG	
	37		316	58	TG	

Locality: SAS 101.13
GPS Coordinates: N78 29,245 E14 13,785
Scanline number: SAS 12.13 strike parallel
Lithological unit: 10
Bed thickness: 55 cm
Bed orientation: 164/40

Fractures:

Unit (m)	Distance (cm)	Fracture frequency	Strike	Dip	Type of fracture	Comments
0-1	1	5	54	84	BC	
	26		54	84	BC	
	38		54	84	BC	
	74		54	84	BC	
	93		54	84	TG	
1-2	42	3	248	84	BC	
	91		248	84	BC	
	50		192	40	BC	
2-3	27	3	252	88	BC	
	45		252	88	BC	
	78		286	64	BC	
3-4	7	3	310	80	BC	
	28		310	80	TG	
	49		284	62	BC	
4-5	10	5	68	82	BC	
	30		164	40	BC	
	44		288	60	TG	

	68		248	88	TG	
	92		248	88	TG	CP
5-6	15	4	80	86	TG	CP
	23		80	86	TG	CP
	28		80	86	TG	CP
	37		320	52	TG	
6-7	15	4	236	88	TG	CP
	21		76	88	TG	
	32		318	48	BC	
	86		76	84	TG	CP

Locality: SAS 101.13
GPS Coordinates: N78 29,245 E14 13,765
Scanline number: SAS 13.13 strike parallel
Lithological unit: 14
Bed thickness: 40 cm
Bed orientation: 164/44

Fractures:

Unit (m)	Distance (cm)	Fracture frequency	Strike	Dip	Type of fracture	Comments
0-1	32	2	76	76	TG	CP
	66		90	80	BC	
1-2	13	3	296	58	TG	CP
	40		94	82	BC	
	58		94	82	TG	
2-3	43	2	256	84	BC	
	47		316	58	TG	
3-4	30	4	278	78	BC	
	41		278	78	TG	
	56		278	78	TG	
	60		316	56	BC	
4-5	10	1	316	54	TG	
5-6	8	2	320	54	BC	
	40		320	54	BC	
6-7	8	2	314	52	BC	
	77		314	52	BC	
7-8	43	1	66	84	BC	

8-9	1	5	86	78	BC
	14		86	78	BC
	29		86	78	BC
	89		86	78	BC
	94		86	78	BC
9-10	8	4	80	68	BC
	20		80	68	BC
	36		80	68	BC
	78		80	68	BC
10-11	35	3	66	86	BC
	68		66	86	TG
	90		66	86	TG
11-12	19	4	62	82	TG
	46		62	82	TG
	68		312	56	BC
	83		312	56	BC
12-13	13	2	310	62	TG
	74		314	62	BC

Locality: SAS 101.13
GPS
Coordinates: N78 29,249 E014 13,727, 42 m.a.s.l
Scanline number: SAS 14.13 strike parallel
Lithological unit: 16
Bed thickness: 60 cm
Bed orientation: 169/44

Fractures:

Unit (m)	Distance (cm)	Fracture frequency	Strike	Dip	Type of fracture	Comments
0-1	1	2	60	89	BC	
	13		60	89	BC	
1-2	10	2	76	78	TG	CP
	30		76	78	TG	
2-3	8	2	84	80	TG	
	45		84	80	TG	
3-4		0				large blocks 2.70-4 m
4-5	4	3	80	78	BC	
5-6	55	4	80	78	BC	CP
	99		316	60	BC	
	27		79	89	BC	
	36		79	89	BC	
6-7	65		328	50	BC	CP
	92		226	70		
	30		84	76	TG	
7-8	27	3	229	64	BC	Curving against south

	44		70	82	TG	
	76		328	52		Calcite vein (7.79 m):2 mm, curved, BC, (260/68)
8-9	68	2	224	78	BC	
	85		224	78	BC	
9-10	6	3	235	62	BC	
	33		274	80	BC	
	56		274	80	BC	
10-11	55	2	84	80	TG	
	72		311	62	TG	
11-12	15	3	85	82	TG	
	39		85	82	TG	
	96		85	82	TG	
12-13	6	2	81	80	BC	
	96		79	80	BC	

Locality: SAS 101.13
GPS Coordinates: N78 29,249 E014 13,712
Scanline number: SAS 15.13 strike parallel
Lithological unit: 17 Slickn lines (212/42)
Bed thickness: 90 cm Slickn side (036/64)
Bed orientation: 138/52

Fractures:

Unit (m)	Distance (cm)	Fracture frequency	Strike	Dip	Type of fracture	Comments
0-1	20	4	270	74	BC	Irregular fracture
	44		328	48	BC	
	61		328	48	BC	
	86		328	48	BC	
1-2	20	2	320	46	TG	
	63		320	46	BC	
2-3	22	4	70	78	BC	
	45		70	78	TG	
	72		70	78	BC	
	84		51	72	TG	
3-4	20	2	236	74	TG	CP
	52		236	74	TG	CP
4-5	74	2	320	54	BC	Pyrite precipitation
	77		336	42	TG	
5-6	35	1	322	50	BC	
6-7		0				
7-8	10	3	329	48	BC	

	55		329	48	BC	
	79		329	48	BC	
8-9	73	1	318	58	BC	
9-10	1	3	51	71	TG	CP
	26		51	71	TG	CP
	88		333	56	BC	Crosses the other fractures on this meter
10-11	1	3	318	48	TG	
	34		318	48	TG	
	76		72	74	TG	
11-12	34	1	79	86	TG	

Locality: SAS 101.13
GPS Coordinates: N78 29,256 E014 13,688, 52 m.a.s.l.
Scanline number: SAS 16.13 strike parallel
Lithological unit: 18
Bed thickness: 85 cm
Bed orientation: 176/46

Fractures:

Unit (m)	Distance (cm)	Fracture frequency	Strike	Dip	Type of fracture	Comments
0-1		0				
1-2	44	2	313	44	BC	
	91		313	44	BC	
2-3	47	3	276	64	BC	
	69		276	64	BC	
	83		318	48	BC	
3-4	50	1	30	52	TG	CP, Slickn side(030/52) and slickn lines (52 -->200)
4-5		0				
5-6		0				
6-7		0				
7-8	94	1	325	46	BC	
8-9	98	1	318	54	TG	
9-10		0				
10-11		0				
11-12		0				
12-13		0				

13-14		0				
14-15	95	1	320	56	BC	
15-16	50	1	87	70	BC	
16-17	86	1	310	56	BC	
17-18		0				
18-19		0				
19-20	27	1	325	42	BC	
20-21		0				
21-22	82	1	322	54	BC	
22-23		0				
23-24		0				
24-25		0				
25-26	26	2	321	50	BC	
	70		321	50	BC	
26-27		0				
27-28		0				
28-29		0				
29-30	98	1	331	56	TG	CP, Slickn side(331/56) and slickn lines (12 -->157)

Locality: SAS 101.13
GPS Coordinates: N78 29,257 E014 13,617, 67 m.a.s.l.
Scanline number: SAS 17.13 strike parallel
Lithological unit: 22
Bed thickness: 120 cm
Bed orientation: 158/36

Fractures:

Unit (m)	Distance (cm)	Fracture frequency	Strike	Dip	Type of fracture	Comments
0-1	17	2	343	68	BC	Fault breccia
	87		343	68	BC	Fault breccia
1-2	2	4	62	82	BC	LBC
	19		62	82	BC	
	27		62	82	BC	
	83		252	68	BC	Irregular fracture
2-3	75	3	90	78	BC	CP
	81		90	78	BC	
	91		90	78	BC	
3-4		0				
4-5	51	6	154	72	LBC	
	72		154	72	TG	
	76		154	72	BC	
	81		154	72	LBC	
	93		154	72	LBC	
5-6	96	1	154	72	LBC	CP
	50		140	46	BC	

6-7	14	3	38	60	LBC	
	50		270	60	TG	
	79		270	60	TG	
7-8	50	2	150	24	BC	
	68		18	50	BC	
8-9		0				
9-10		0				Calcite vein (9.04 m): 2 mm, LBC, (070/74)
10-11		0				
11-12		0				
12-13		0				
13-14	18	5	33	66	BC	
	25		33	66	BC	
	41		169	54	BC	CP
	81		33	66	LBC	CP
	91		33	66	BC	CP
14-15	79	2	42	79	LBC	
	96		42	79	BC	
15-16	3	1	33	68	BC	
16-17		0				
17-18		0				
18-19	80	1	164	58	TG	CP
19-20	30	3	203	48	BC	
	33		332	50	LBC	
	82		19	59	BC	

Locality: SAS 101.13
GPS Coordinates: N78 29,304 E014 13,569, 90 m.a.s.l.
Scanline number: SAS 18.13 strike parallel
Lithological unit: 22
Bed thickness: 55 cm
Bed orientation: 160/58

Fractures:

Unit (m)	Distance (cm)	Fracture frequency	Strike	Dip	Type of fracture	Comments
0-1		0				
1-2		0				
2-3	66	1	17	60	BC	CP
3-4		0				
4-5	77	1	322	42	LBC	
5-6		0				
6-7	70	1	300	52	BC	
7-8	44	3	294	56	BC	
	63		294	56	BC	
	90		279	66	LBC	
8-9	8	3	279	66	BC	
	25		279	66	BC	
	54		279	66	BC	
9-10	14	1	58	58	TG	CP, Slickn side(058/58), slickn line (180/48)

Locality: SAS 101.13
GPS Coordinates: 33X 0482891 8713076 +- 3 m
Scanline number: SAS 1.14A strike parallel
Lithological unit: 10
Bed thickness: 62 cm, varying thickness. Thinner and less distinct beds towards the South
Bed orientation: 164/40

Fractures:

Unit (m)	Distance (cm)	Fracture frequency	Strike	Dip	Type of fracture	Comments
0-1		0				
1-2	54	2	72	87	TG	
	85		261	61	TG	
2-3		0				
3-4	34	1	114	88	TG	
4-5	35	3	314	62	BC	
	52		314	62	BC	
	77		314	62	BC	
5-6	12	3	316	64	BC	
	43		316	64	BC	
	79		316	64	BC	
6-7	28	2	316	64	BC	
	70		295	66	BC	
7-12		0				
12-13	77	1	296	68	BC	
13-14	24	2	296	68	BC	
	62		197	63	BC	
14-15		0				

15-16	1	1	304	66	BC
16-17		0			
17-18	33	2	294	60	TG
	95		294	60	TG
18-19	28	1	306	64	BC
19-20		0			
20-21	5	3	325	60	BC
	45		270	82	BC
	80		356	54	BC

Locality: SAS 101.13
GPS Coordinates: 33X 0482891 8713076 +- 3 m
Scanline number: SAS 1.14B - dip parallel (SP)
Lithological unit: 10
Bed thickness: 62 cm, varying thickness. Thinner and less distinct beds towards the South
Bed orientation: 173/40

Fractures:

Unit (m)	Distance (cm)	Fracture frequency	Strike	Dip	Type of fracture	Comments
0-1	1	5	340	42		
	29		340	42		
	70		348	56		
	80		348	56		
	84		40	78		
1-2	3	3	332	49		
	15		332	49		
	24		54	85		

Locality: SAS 101.13
GPS Coordinates: 33X 0482891 8713076 +- 3 m
Scanline number: SAS 2.14 - dip parallel
Lithological unit: 20
Bed thickness: 55 cm
Bed orientation:

Fractures:

Unit (m)	Distance (cm)	Fracture frequency	Strike	Dip	Type of fracture	Comments
0-1	55	1	346	30		
1-2	32	1	343	22		

Locality: SAS 101.13
GPS Coordinates: 33X 0482891 8713076 +- 3 m
Scanline number: SAS 3.14 - dip parallel
Lithological unit: 21
Bed thickness: 60 cm
Bed orientation:

Fractures:

Unit (m)	Distance (cm)	Fracture frequency	Strike	Dip	Type of fracture	Comments
0-1	16	3	19	58		Strike slip fault
	68		352	45		
	97		352	45		
1-2	39	1	357	48		

Locality:**GPS Coordinates:** 33X 0482891 8713076 +- 3 m**Scanline number:** SAS 4.14 - dip parallel**Lithological unit:** 20**Bed thickness:** 3 m**Bed orientation:****Fractures:**

Unit (m)	Distance (cm)	Fracture frequency	Strike	Dip	Type of fracture	Comments
0-1	10	2	350	44		
	18		350	44		
1-2	30	1	347	44		

Locality: SAS 101.13
GPS Coordinates: 33X 0482891 8713076 +- 3 m
Scanline number: SAS 5.14 - strike parallel
Lithological unit: 25
Bed thickness: 1 m
Bed orientation:

Fractures:

Unit (m)	Distance (cm)	Fracture frequency	Strike	Dip	Type of fracture	Comments
0-5		0				
5-6	1	2	23	42		
	45		270	68		
6-10		0				
10-11	1	2	270	80		
	2		34	54		
11-28		0				
28-29	1	2	255	68		
	13		292	77		
29-30		0				
30-31	2	1	142	64		CP
31-40		0				
40-41	5	1	140	60		slickn side
41-44		0				
44-45	55	1	19	30		
45-46	15	2	270	71		slickn side
	32		270	71		slickn side

Locality: SAS 101.13
GPS Coordinates: 33X 0482891 8713076 +- 3 m
Scanline number: SAS 6.14 - strike parallel
Lithological unit: 2
Bed thickness: 67 cm, massive towards South and more shaly towards North
Bed orientation: 156/38

Fractures:

Unit (m)	Distance (cm)	Fracture frequency	Strike	Dip	Type of fracture	Comments
0-1		0				
1-2	1	3	77	70	BC	
	2		255	80	BC	
	43		32	71	TG	
2-3	1	3	74	73	TG	
	48		54	80	TG	
	78		258	78	TG	
3-4	6	3	76	80	TG	
	49		77	80	BC	
	53		77	80	BC	
4-5	84	1	65	78	BC	
5-6	35	2	65	78	BC	
	79		59	77	BC	
6-7	8	2	59	77	BC	
	63		54	88	BC	CP
7-8	96	1	40	82	BC	
8-9		0				
9-10	6	3	68	84	BC	

	16		68	84	BC
	25		68	84	BC
10-11	79	1	254	82	BC

Locality: SAS 101.13
GPS Coordinates: 33X 0482891 8713076 +- 3 m
Scanline number: SAS 7.14 - strike parallel
Lithological unit: 3
Bed thickness: 72 cm
Bed orientation: 356/28

Fractures:

Unit (m)	Distance (cm)	Fracture frequency	Strike	Dip	Type of fracture	Comments
0-1	98	1	358	56	TG	
1-2	60	1	358	56	TG	
2-3		0				
3-4	15	1	296	70	TG	
4-5	96	1	59	77	BC	CP
5-10		0				
10-11	7	1	326	60	BC	
11-12	27	1	300	69	BC	CP
12-13		0				
13-14	70	1	298	66	BC	
14-15	24	1	298	66	BC	
15-16	10	1	282	72	BC	CP
16-19		0				
19-20	3	1	346	54	BC	
20-21	5	1	346	54	BC	
21-22	5	2	346	54	BC	
	83		88	85	BC	

22-23	24	1	88	85	BC	
23-24	46	1	261	78	TG	CP
24-25		0				
25-26		0				
26-27	20	2	270	74	BC	
	95		282	64	BC	
27-28	44	1	282	64	BC	
28-31		0				
31-32	48	1	358	74	BC	

Locality: SAS 101.13
GPS Coordinates: 33X 0482891 8713076 +- 3 m
Scanline number: SAS 8.14 - strike parallel
Lithological unit: 8
Bed thickness: 1 m
Bed orientation: 171/46

Fractures:

Unit (m)	Distance (cm)	Fracture frequency	Strike	Dip	Type of fracture	Comments
0-1	60	1	23	62	BC	
1-2	1	4	299	64	BC	
	45		18	53	BC	
	80		289	72	TG	
	93		289	72	TG	
2-3	80	1	270	67	BC	
3-4	50	4	281	66	TG	
	60		281	66	TG	
	83		281	66	TG	
	99		281	66	TG	
4-5		0				
5-6	1	1	141	44	BC	
6-10		0				
10-11	66	1	90	84	BC	
11-13		0				
13-14	5	2	292	76	BC	
	80		288	64	TG	

14-15

50

1

265

81

BC

Locality: SAS 101.13
GPS Coordinates: 33X 0482891 8713076 +- 3 m
Scanline number: SAS 9.14 - strike parallel
Lithological unit: 9
Bed thickness: 28 cm - thickest in the middle of the scanline
Bed orientation: 156/44

Fractures:

Unit (m)	Distance (cm)	Fracture frequency	Strike	Dip	Type of fracture	Comments
0-1	72	2	258	79	TG	
	96		258	79	TG	
1-2	18	2	258	79	TG	
	65		314	62	TG	
2-3	5	4	314	62	TG	
	26		258	74	BC	
	75		258	74	BC	
	87		258	74	BC	
3-4	25	1	68	84	TG	
4-5		0				
5-6	10	2	78	89	BC	
	60		255	78	BC	
6-7	26	3	83	88	BC	
	86		314	62	BC	
	97		314	62	BC	
7-8	17	2	314	62	BC	
	87		270	74	TG	

8-9	28	2	301	65	BC
	72		301	65	BC
9-10	43	1	309	56	TG
10-11	40	1	306	60	BC

Locality: SAS 101.13
GPS Coordinates: 33X 0482891 8713076 +- 3 m
Scanline number: SAS 10.14A - strike parallel
Lithological unit: 12
Bed thickness: 35 cm
Bed orientation: 170/42

Fractures:

Unit (m)	Distance (cm)	Fracture frequency	Strike	Dip	Type of fracture	Comments
0-1	1	1	35	60	BC	
1-2		0				
2-3	20	2	43	73	BC	
	70		255	74	BC	
3-4	1	2	68	86	BC	
	54		261	74	BC	
4-5	76	1	30	72	BC	
5-7		0				Covered 4.40 – 7 m
7-8	14	1	260	72	BC	
8-9	62	1	257	72	BC	
9-10		0				
10-11		0				
11-12	1	1	259	74	TG	
12-13		0				
13-14	1	1	182	74	TG	

Locality: SAS 101.13
GPS Coordinates: 33X 0482891 8713076 +- 3 m
Scanline number: SAS 10.14B - dip parallel
Lithological unit: 12
Bed thickness: 35 cm
Bed orientation: 170/42

Fractures:

Unit (m)	Distance (cm)	Fracture frequency	Strike	Dip	Type of fracture	Comments
0-1	2	3	269	74		
	44		2	49		
	76		351	50		
1-2	6	2	6	55		
	45		42	60		

Locality: SAS 101.13
GPS Coordinates: 33X 0482891 8713076 +- 3 m
Scanline number: SAS 11.14A - strike parallel
Lithological unit: 13
Bed thickness: 23 cm
Bed orientation: 162/44

Fractures:

Unit (m)	Distance (cm)	Fracture frequency	Strike	Dip	Type of fracture	Comments
0-1	17	1	266	72	BC	
1-2	29	4	300	64	BC	
	32		235	80	TG	
	60		279	66	BC	
	90		30	32	BC	
2-3	19	3	261	70	BC	
	46		265	82	BC	
	87		11	32	BC	
3-4	20	3	267	68	BC	
	37		11	32	BC	
	92		257	80	BC	
4-5	25	3	11	32	BC	
	44		257	80	BC	
	80		257	80	BC	
5-6	62	2	266	76	BC	
	66		266	76	BC	
6-7	73	1	76	86	BC	

7-8	1	2	359	30	BC
	72		81	87	BC
8-9	7	2	359	30	BC
	74		268	80	BC
9-10	10	4	355	24	BC
	50		355	24	BC
	60		64	86	BC
	75		64	86	BC

Locality: SAS 101.13
GPS Coordinates: 33X 0482891 8713076 +- 3 m
Scanline number: SAS 11.14B - dip parallel
Lithological unit: 13
Bed thickness: 23 cm
Bed orientation: 162/44

Fractures:

Unit (m)	Distance (cm)	Fracture frequency	Strike	Dip	Type of fracture	Comments
0-1	2	6	1	58		
	4		256	60		
	5		1	58		
	42		1	58		
	66		356	62		
	76		356	62		
1-2	60	4	356	30		
	82		277	76		
	83		356	30		
2-3	32	1	356	30		

Locality: SAS 101.13
GPS Coordinates: 33X 0482891 8713076 +- 3 m
Scanline number: SAS 12.14 - strike parallel
Lithological unit: 14
Bed thickness: 32 cm
Bed orientation: 161/36

Fractures:

Unit (m)	Distance (cm)	Fracture frequency	Strike	Dip	Type of fracture	Comments
0-1	36	1	258	73	BC	
1-2	1	3	269	62	BC	
	41		242	70	BC	
	77		248	78	BC	
2-3	34	4	194	72	TG	
	43		315	60	BC	
	54		315	60	BC	
	98		240	82	BC	
3-4	10	2	266	87	BC	
	65		296	70	BC	
4-5	64	1	52	84	TG	
5-6	18	2	60	82	BC	
	57		244	70	BC	
6-7	11	3	175	66	TG	
	20		320	56	BC	
	56		219	76	BC	
7-8	19	3	262	74	BC	

	31		262	74	BC	
	67		262	74	BC	
8-9	1	4	250	78	BC	
	21		250	78	BC	
	60		250	78	BC	
	90		250	78	BC	
9-10	52	1	278	80	BC	
10-11		0				
11-12	52	1	246	68	BC	
12-13	13	3	61	72	TG	
	52		256	74	BC	
	98		66	79	TG	
13-14		0				
14-15	22	1	56	79	TG	
15-16	87	1	318	63	BC	
16-17	9	2	318	63	BC	
	53		318	63	BC	
17-18	15	2	303	62	TG	
	70		316	62	BC	
18-19	44	2	232	72	BC	Listric shape
	63		318	56	TG	
19-20	30	2	318	60	BC	
	70		302	66	BC	

Locality: SAS 101.13
GPS Coordinates: 33X 0482891 8713076 +- 3 m
Scanline number: SAS 13.14A - strike parallel
Lithological unit: 16
Bed thickness: 43 cm
Bed orientation: 152/42

Fractures:

Unit (m)	Distance (cm)	Fracture frequency	Strike	Dip	Type of fracture	Comments
0-1	50	3	263	74	TG	
	61		260	72	BC	
	78		264	78	TG	
1-2	7	4	264	78	TG	
	17		264	78	TG	
	55		261	76	BC	
	87		7	74	TG	
2-3	7	4	7	74	TG	
	78		246	74	BC	
	83		246	74	BC	
	88		7	60	BC	
3-4	32	3	28	77	BC	
	42		261	74	TG	
	56		261	74	TG	CP
4-5	11	4	261	74	TG	
	46		257	73	TG	
	50		257	73	TG	

82

307 57

TG

Locality: SAS 101.13
GPS Coordinates: 33X 0482891 8713076 +- 3 m
Scanline number: SAS 13.14B - dip parallel
Lithological unit: 16
Bed thickness: 43 cm
Bed orientation: 152/42

Fractures:

Unit (m)	Distance (cm)	Fracture frequency	Strike	Dip	Type of fracture	Comments
0-1	32	2	358	54	TG	
	62		324	44	TG	
1-2	14	4	324	44	TG	
	53		325	54	BC	
	63		325	54	BC	
	80		325	54	BC	
2-3	10	1	312	50	TG	High uncertainty

Locality: SAS 101.13
GPS Coordinates: 33X 0482891 8713076 +- 3 m
Scanline number: SAS 14.14 - strike parallel
Lithological unit: 17
Bed thickness: 50 cm
Bed orientation: 158/46

Fractures:

Unit (m)	Distance (cm)	Fracture frequency	Strike	Dip	Type of fracture	Comments
0-1		0				
1-2	96	1	359	62	TG	
2-3	87	1	198	70	BC	
3-8		0				
8-9	66	1	19	64	TG	
9-12		0				
12-13	30	3	2	49	TG	
	60		2	49	TG	
	97		270	78	TG	
13-14	40	1	2	49	TG	
14-15	80	1	354	46	TG	
15-16		0				
16-17	34	2	254	78	BC	
	55		254	78	BC	
17-20		0				
20-21	37	1	8	56	BC	
21-22	67	2	287	56	TG	

	98		356	52	BC
22-23	23	1	287	56	TG
23-24	92	1	10	42	BC
24-25		0			
25-26	5	1	10	42	TG

Locality: SAS 101.13
GPS Coordinates: 33X 0482891 8713076 +- 3 m
Scanline number: SAS 15.14A - strike parallel
Lithological unit: 13
Bed thickness: 28 cm
Bed orientation: 169/38

Similar bed as SAS 11.14, but ca. 60 m further south

Fractures:

Unit (m)	Distance (cm)	Fracture frequency	Strike	Dip	Type of fracture	Comments
0-1	35	2	64	89	BC	CP
	83		64	89	BC	
1-2	14	5	261	82	BC	
	23		261	82	BC	
	26		334	54	BC	
	64		62	86	BC	
	71		334	54	BC	
2-3	22	1	282	60	BC	
3-4	36	4	334	60	BC	
	56		270	72	BC	
	74		334	60	BC	
	90		270	60	BC	
4-5	52	1	264	72	BC	
5-6	23	3	295	68	BC	
	58		265	47	BC	
	89		280	68	BC	
6-7	1	1	7	50	BC	

7-9		0					Covered: 6.30 – 9.10 m
9-10	32	3	267	70	BC		
	63		267	70	BC		
	95		72	81	BC		
10-11	6	4	10	50	BC		
	43		260	64	BC		
	54		26	36	BC		
	88		72	78	BC		
11-12	22	5	26	36	BC		
	25		321	60	BC		
	38		252	82	BC		
	52		69	86	BC		
	84		260	66	BC		
12-13	2	3	260	66	BC		
	30		49	84	BC		CP
	86		14	36	BC		
13-14	4	3	70	82	BC		
	33		265	36	BC		
	54		64	84	BC		
14-15	7	2	261	65	BC		
	43		85	82	BC		
15-16	20	4	20	46	BC		
	27		69	84	BC		
	37		264	80	BC		
	51		69	84	BC		
16-17	4	3	257	78	BC		
	25		257	78	BC		

36

9

39

BC

Locality: SAS 101.13
GPS Coordinates: 33X 0482891 8713076 +- 3 m
Scanline number: SAS 15.14B - dip parallel
Lithological unit: 13
Bed thickness: 28 cm
Bed orientation: 169/38

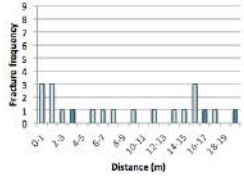
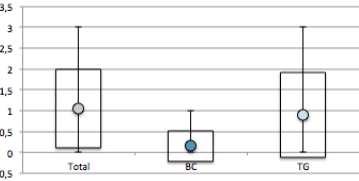
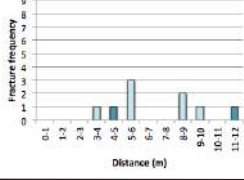
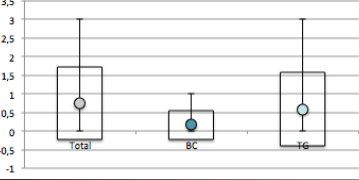
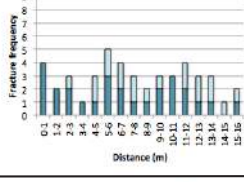
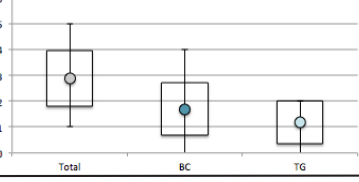
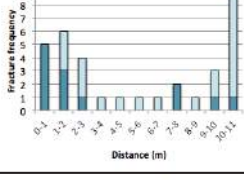
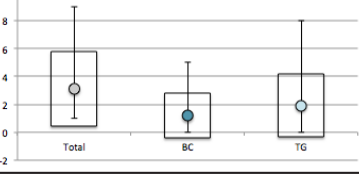
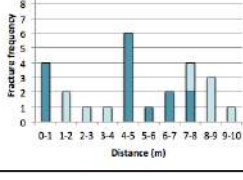
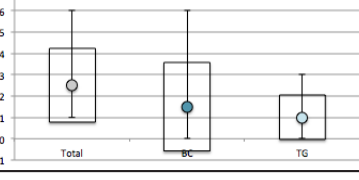
Fractures:

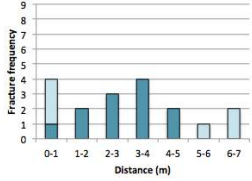
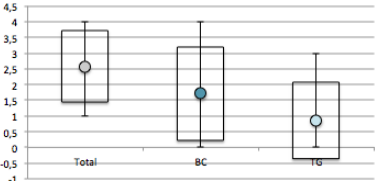
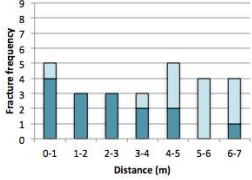
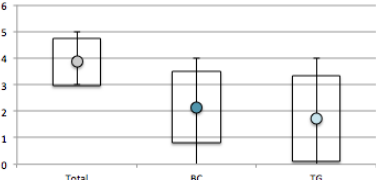
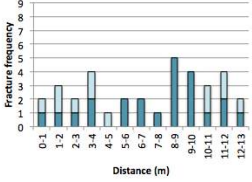
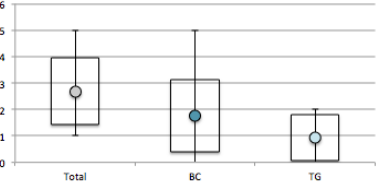
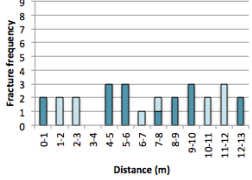
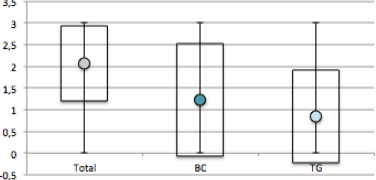
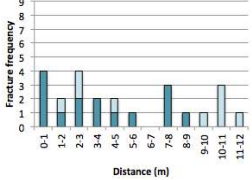
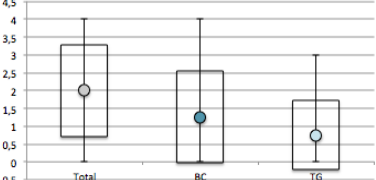
Unit (m)	Distance (cm)	Fracture frequency	Strike	Dip	Type of fracture	Comments
0-1	12	5	352	62		
	27		353	64		
	40		84	86		CP
	56		2	32		
	84		33	28		
1-2	2	6	324	62		
	12		6	34		
	40		84	86		CP
	54		6	34		
	69		349	29		
	75		344	65		

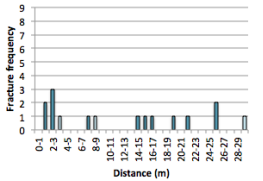
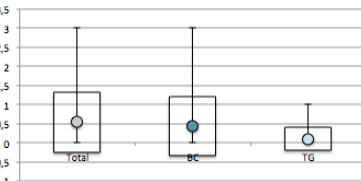
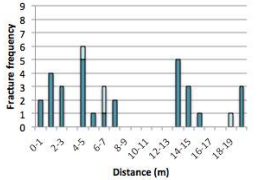
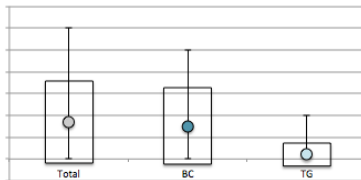
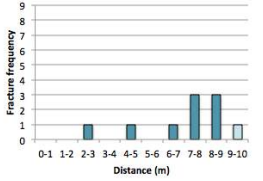
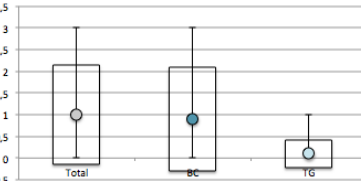
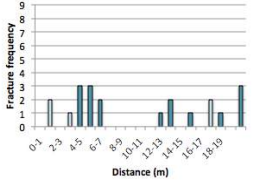
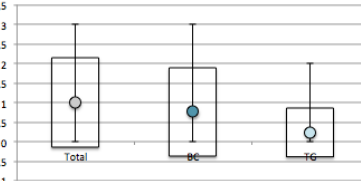
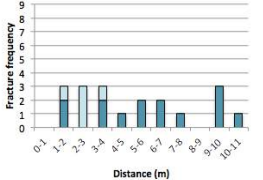
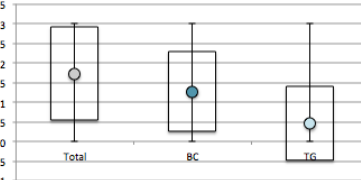
Appendix 4 – Fracture frequency for each scanline

Plots for each scanline displaying number of fractures for every meter in a stacked column plot (left) and error bar plot (right). Summary plots are displayed in Chapter 5.6.

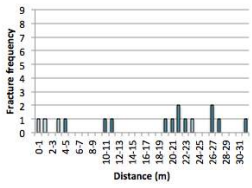
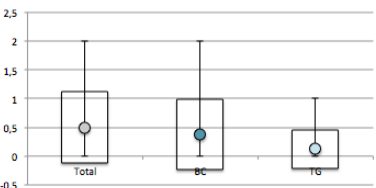
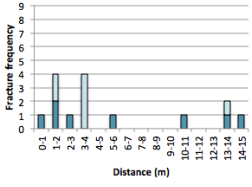
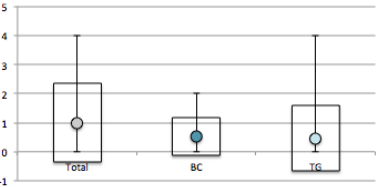
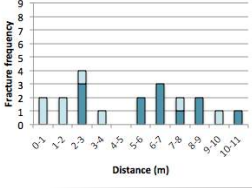
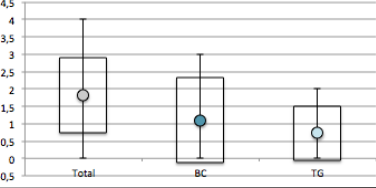
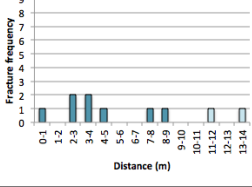
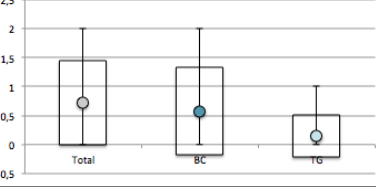
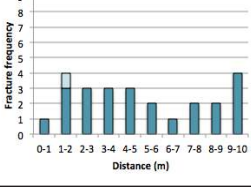
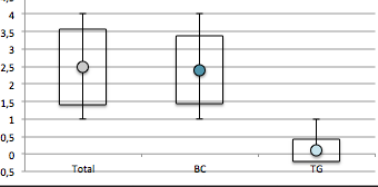
Scanline	Fracture frequency	
SAS 1.13	<p>SAS 1.13</p> <p>Fracture frequency</p> <p>Distance (m)</p> <p>Legend: TG (through going), BC (bed confined)</p>	<p>SAS 1.13</p> <p>Fracture frequency</p> <p>Total BC TG</p>
SAS 2.13	<p>SAS 2.13</p> <p>Fracture frequency</p> <p>Distance (m)</p> <p>Legend: TG (through going), BC (bed confined)</p>	<p>SAS 2.13</p> <p>Fracture frequency</p> <p>Total BC TG</p>
SAS 3.13	<p>SAS 3.13</p> <p>Fracture frequency</p> <p>Distance (m)</p> <p>Legend: TG (through going), BC (bed confined)</p>	<p>SAS 3.13</p> <p>Fracture frequency</p> <p>Total BC TG</p>
SAS 4.13	<p>SAS 4.13</p> <p>Fracture frequency</p> <p>Distance (m)</p> <p>Legend: TG (through going), BC (bed confined)</p>	<p>SAS 4.13</p> <p>Fracture frequency</p> <p>Total BC TG</p>
SAS 5.13	<p>SAS 5.13</p> <p>Fracture frequency</p> <p>Distance (m)</p> <p>Legend: TG (through going), BC (bed confined)</p>	<p>SAS 5.13</p> <p>Fracture frequency</p> <p>Total BC TG</p>

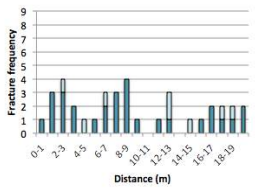
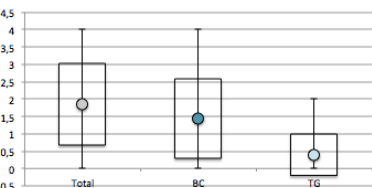
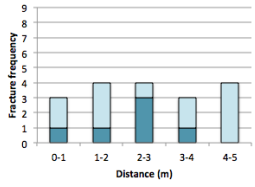
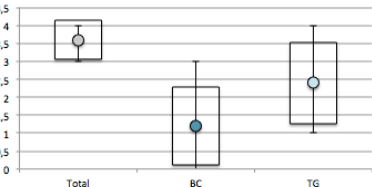
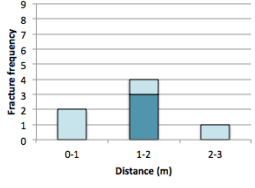
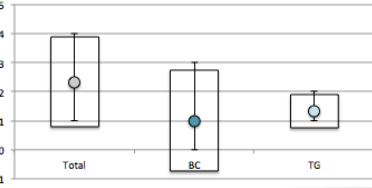
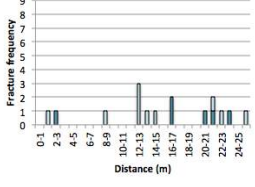
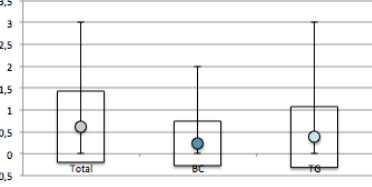
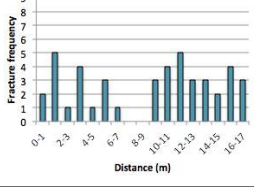
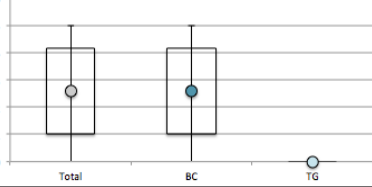
Scanline	Fracture frequency	
SAS 6.13	<p style="text-align: center;">SAS 6.13</p>  <p>Fracture frequency</p> <p>Distance (m)</p> <p>Legend: TG (through going), BC (bed confined)</p>	<p style="text-align: center;">SAS 6.13</p>  <p>Fracture frequency</p> <p>Total BC TG</p>
SAS 7.13	<p style="text-align: center;">SAS 7.13</p>  <p>Fracture frequency</p> <p>Distance (m)</p> <p>Legend: TG (through going), BC (bed confined)</p>	<p style="text-align: center;">SAS 7.13</p>  <p>Fracture frequency</p> <p>Total BC TG</p>
SAS 8.13	<p style="text-align: center;">SAS 8.13</p>  <p>Fracture frequency</p> <p>Distance (m)</p> <p>Legend: TG (through going), BC (bed confined)</p>	<p style="text-align: center;">SAS 8.13</p>  <p>Fracture frequency</p> <p>Total BC TG</p>
SAS 9.13	<p style="text-align: center;">SAS 9.13</p>  <p>Fracture frequency</p> <p>Distance (m)</p> <p>Legend: TG (through going), BC (bed confined)</p>	<p style="text-align: center;">SAS 9.13</p>  <p>Fracture frequency</p> <p>Total BC TG</p>
SAS 10.13	<p style="text-align: center;">SAS 10.13</p>  <p>Fracture frequency</p> <p>Distance (m)</p> <p>Legend: TG (through going), BC (bed confined)</p>	<p style="text-align: center;">SAS 10.13</p>  <p>Fracture frequency</p> <p>Total BC TG</p>

Scanline	Fracture frequency	
SAS 11.13	<p style="text-align: center;">SAS 11.13</p>  <p style="text-align: right;"> □ TG (through going) ■ BC (bed confined) </p>	<p style="text-align: center;">SAS 11.13</p> 
SAS 12.13	<p style="text-align: center;">SAS 12.13</p>  <p style="text-align: right;"> □ TG (through going) ■ BC (bed confined) </p>	<p style="text-align: center;">SAS 12.13</p> 
SAS 13.13	<p style="text-align: center;">SAS 13.13</p>  <p style="text-align: right;"> □ TG (through going) ■ BC (bed confined) </p>	<p style="text-align: center;">SAS 13.13</p> 
SAS 14.13	<p style="text-align: center;">SAS 14.13</p>  <p style="text-align: right;"> □ TG (through going) ■ BC (bed confined) </p>	<p style="text-align: center;">SAS 14.13</p> 
SAS 15.13	<p style="text-align: center;">SAS 15.13</p>  <p style="text-align: right;"> □ TG (through going) ■ BC (bed confined) </p>	<p style="text-align: center;">SAS 15.13</p> 

Scanline	Fracture frequency	
SAS 16.13	<p style="text-align: center;">SAS 16.13</p>  <p>Fracture frequency</p> <p>Distance (m)</p> <p>Legend: □ TG (through going), ■ BC (bed confined)</p>	<p style="text-align: center;">SAS 16.13</p>  <p>Fracture frequency</p> <p>Legend: □ Total, ■ BC, □ TG</p>
SAS 17.13	<p style="text-align: center;">SAS 17.13</p>  <p>Fracture frequency</p> <p>Distance (m)</p> <p>Legend: □ TG (through going), ■ BC (bed confined)</p>	<p style="text-align: center;">SAS 17.13</p>  <p>Fracture frequency</p> <p>Legend: □ Total, ■ BC, □ TG</p>
SAS 18.13	<p style="text-align: center;">SAS 18.13</p>  <p>Fracture frequency</p> <p>Distance (m)</p> <p>Legend: □ TG (through going), ■ BC (bed confined)</p>	<p style="text-align: center;">SAS 18.13</p>  <p>Fracture frequency</p> <p>Legend: □ Total, ■ BC, □ TG</p>
SAS 1.14A	<p style="text-align: center;">SAS 1.14A</p>  <p>Fracture frequency</p> <p>Distance (m)</p> <p>Legend: □ TG (through going), ■ BC (bed confined)</p>	<p style="text-align: center;">SAS 1.14A</p>  <p>Fracture frequency</p> <p>Legend: □ Total, ■ BC, □ TG</p>
SAS 6.14	<p style="text-align: center;">SAS 6.14</p>  <p>Fracture frequency</p> <p>Distance (m)</p> <p>Legend: □ TG (through going), ■ BC (bed confined)</p>	<p style="text-align: center;">SAS 6.14</p>  <p>Fracture frequency</p> <p>Legend: □ Total, ■ BC, □ TG</p>

Appendix 4 – Fracture frequency for each scanline

Scanline	Fracture frequency	
SAS 7.14	<p style="text-align: center;">SAS 7.14</p>  <p style="text-align: center;">Distance (m)</p>	<p style="text-align: center;">SAS 7.14</p> 
SAS 8.14	<p style="text-align: center;">SAS 8.14</p>  <p style="text-align: center;">Distance (m)</p>	<p style="text-align: center;">SAS 8.14</p> 
SAS 9.14	<p style="text-align: center;">SAS 9.14</p>  <p style="text-align: center;">Distance (m)</p>	<p style="text-align: center;">SAS 9.14</p> 
SAS 10.14A	<p style="text-align: center;">SAS 10.14A</p>  <p style="text-align: center;">Distance (m)</p>	<p style="text-align: center;">SAS 10.14</p> 
SAS 11.14	<p style="text-align: center;">SAS 11.14</p>  <p style="text-align: center;">Distance (m)</p>	<p style="text-align: center;">SAS 11.14</p> 

Scanline	Fracture frequency	
SAS 12.14	<p style="text-align: center;">SAS 12.14</p>  <p style="text-align: right;"> TG (through going) BC (bed confined) </p>	<p style="text-align: center;">SAS 12.14</p> 
SAS 13.14A	<p style="text-align: center;">SAS 13.14A</p>  <p style="text-align: right;"> TG (through going) BC (bed confined) </p>	<p style="text-align: center;">SAS 13.14A</p> 
SAS 13.14A	<p style="text-align: center;">SAS 13.14B</p>  <p style="text-align: right;"> TG (through going) BC (bed confined) </p>	<p style="text-align: center;">SAS 13.14B</p> 
SAS 14.14	<p style="text-align: center;">SAS 14.14</p>  <p style="text-align: right;"> TG (through going) BC (bed confined) </p>	<p style="text-align: center;">SAS 14.14</p> 
SAS 15.14A	<p style="text-align: center;">SAS 15.14A</p>  <p style="text-align: right;"> TG (through going) BC (bed confined) </p>	<p style="text-align: center;">SAS 15.14A</p> 

Appendix 5 – SEM Results

Results from element tests done in SEM (scanning electron microscope) of selected thin sections.

